CITY UNIVERSITY OF HONG KONG
香港城市大學

Patch Clamp Technique with Integration of Automatic Cell Identification for Ion Channel Activities Recording and Cell Microinjection

膜片鉗技術結合自動細胞識別功能技術以用於進行離子通道訊息採集和細胞微注射

Submitted to

Department of Biomedical Engineering

生物醫學工程學系

in Partial Fulfillment of the Requirements

for the Degree of Doctor of Philosophy

哲學博士學位

by

Chan Hiu Ling

陳曉玲

April 2022

二零二二年四月

Abstract

Ion channels are specialised proteins in the plasma membrane that provides a passageway for charged ions, including sodium ($Na^{+)}$, potassium (K^+), chloride (Cl^-), and calcium (Ca^+) ions; and ion channel activities are crucial related to the physiology of living creatures. Abnormal ion channel activities can lead to neurodegenerative diseases such as Amyotrophic lateral sclerosis (ALS) and Alzheimer's disease (AD). Thus, recording of the ion channels' activities from time to time is regarded as valuable data for tracing how such conditions were developed, and hence it may be possible to assist the diagnosis of patients. The patch clamp technique is considered a gold method to record the ion channels activities. This technique can measure the ultra-low current going down to pico ampere across the cell membrane.

In this thesis, the patch clamp technique is used to develop cytoplasmic microinjection with current feedback for small and non-spherical cells. Cell microinjection is commonly used for intracellular delivery of various substances into cells using micropipettes. It plays a crucial role in drug deliveries, cell transfection, and gene therapy using human cells. However, cell microinjection always requires a skilled operator to manipulate a micropipette carefully, so it is inefficient to carry out the cell microinjection, especially for cells that are small in micron scale. It is quite challenging to observe and determine whether the target materials are injected into the cell spontaneously with the naked eye of humans. To reduce the operational failure due to human errors, other research groups have introduced different feedback approaches such as visual and voltage feedback. Using the features of high current sensitivity of the patch clamp technique, we have introduced the patch clamp technique to monitor the microinjection by observing the electrical current passing through the living cell. The electrical current response not only can indicate the materials injected into the cell during the microinjection but also can verify the cell viability after the microinjection. In our studies, an electrical equivalent model for cytoplasmic microinjection has been developed and cell viability verification with SH-SY5Y (human-derived neuroblastoma cell) and HEK-293 (human embryonic kidney cell) have been performed after the microinjection.

After building the electrical equivalent model, we have converted the model into the equivalent electric circuit to calculate the current response with four different injection volumes during the microinjection. During the experiment, a linear relationship is found between the injection volumes and the drop of the current signals. In the equivalent electric circuit, I_{Seal} (current passing the sealing resistance) and I_{Access} (current passing the access resistance) have been calculated and we have found that I_{Seal} is the significant factor of I_m (cell membrane current) for monitoring the injection volume.

Nevertheless, the patch clamp technique has a low throughput due to operational challenges. Traditional operations are complex and labour-intensive, especially the first step to identify suitable cells which can be poked with a glass micropipette without destroying the cell membrane based on microscopic images. The subtle morphological differences between suitable and unsuitable cells are difficult to detect by inexperienced operators or using traditional machine learning approaches. It is desirable to develop an automatic and accurate detection method to select suitable cells for every operation. Hence, a novel signalling model called CELL-YOLO has been developed to detect suitable cells for electrophysiological recording based on the YOLO (You only look once) model [23]. To verify its effectiveness, HEK-293 cells have been chosen as target cells in this study. CELL-YOLO has been trained with three different data sizes of HEK-293 cell images in our self-built datasets and three resulting models named CELL-YOLO^{104}, CELL-YOLO^{306} and CELL-YOLO^{612} have been generated. The learning ability of CELL-YOLO has been verified by comparison among these three trained models. To assess CELL-YOLO's performance, the newly developed YOLO models that are YOLOV3 and YOLOV4 have also been trained with the largest dataset for comparison. To quantify the performance, the accuracy can be measured using mAP_{50} (mean average precision when intersection over union (IoU)=50), and mAP_{75} (mean average precision when IoU=75), whilst the processing speed can be measured using FPS (frames per second).

We have found that the mAP_{50}, mAP_{75}, and FPS of CELL-YOLO^{612} are 35.65, 21.26, and 30, respectively, which are higher than those parameters of YOLOV3 and YOLOV4. The mAP and FPS results indicate the superiority of our proposed model in this specific application in terms of accuracy and processing speed.

Since the patch clamp technique can measure the ultra-low current that goes down to pico ampere, it is a reliable electrophysiological technique to reveal and quantify neuronal activities. The developed method has been applied to electrophysiological signals in both voltage and current clamp to verify if the induced pluripotent stem (iPS) cells can be differentiated into neuronal stem cells (NSCs) on different biocompatible extracellular matrices (ECMs). After plating the stem cells on the glass slip as a control and two different ECMs that are L-NHs (Left-handed nano-helices subtract) and NZs (Nano-zigzags subtract), the whole-cell voltage-clamp has been used to monitor the total current flow across the entire membrane of the stem cell due to the total ion channel activity in response to voltage stimuli. The activities of the Na^+ and K^+ ion channels of the stem cells have been recorded and those ion channel activities can be ascribed to neuronal signalling. Using the current clamp, the NSCs can exhibit spontaneous firing with current stimuli, and that signal firing is one of the typical neuronal signalling activities. Thus, the experimental result can prove that iPSC can be differentiated into NSC successfully.

CITY UNIVERSITY OF HONG KONG

Qualifying Panel and Examination Panel

Surname: Chan

First Name: Hiu Ling

Degree: PhD

College/Department: Department of Biomedical Engineering

The Qualifying Panel of the above student is composed of:

Supervisor(s)

Prof. LAI Wai Chiu King	Department of Biomedical Engineering City University of Hong Kong

Qualifying Panel Member(s)

Prof. Tin Chung	Department of Biomedical Engineering City University of Hong Kong
Prof. Li You Fu	Department of Mechanical Engineering City University of Hong Kong

Qualifying Panel Member(s)

Prof. LAI Wai Chiu King	Department of Biomedical Engineering City University of Hong Kong
Prof. TIN Chung	Department of Biomedical Engineering City University of Hong Kong
Prof. LI Wen Jung	Department of Mechanical Engineering City University of Hong Kong
Prof. ZHANG Li	Department of Mechanical and Automation Engineering The Chinese University of Hong Kong

CITY UNIVERSITY OF HONG KONG

Department of Biomedical Engineering

Statement on the Extent of Research Collaboration

If any part of your research has been carried out in collaboration with other parties, please indicate the extent of collaboration, and to identify any parts of the dissertation thesis which are not the result of your own work.

☐ No.

☑ Yes. If yes, please specify.

(1) Cell-YOLO modelling design (partially works of chapter 5), is provided by Mr Zhe Liu at Nano/Bio Robotic Laboratory (NRL), City University of Hong Kong.

(2) Cell data collection (partially works of chapter 5), is prepared by Miss Yee Ching Wong and Miss Karey Yee Lam Liu at Nano/Bio Robotic Laboratory (NRL), City University of Hong Kong.

(3) The biocompatible extracellular matrices (ECMs) and the neuronal stem cells (NSCs) (partially works of chapter 6) are prepared by the research group led by Dr Zhifeng Huang and Dr Ken Kin Lam Yung at Hong Kong Baptist University.

(4) The rest of the works are all designed and operated by myself under the supervision of Prof. LAI Wai Chiu King at Nano/Bio Robotic Laboratory (NRL), City University of Hong Kong.

Signed by

Chan Hiu Ling

Date: 31.3.2022

Acknowledgement

First, I would like to give my greatest thanks to my supervisor, Prof. Lai Wai Chiu King, for his guidance, patience, and advice over the past years, which paved the way for this dissertation. I was inspired by many new approaches to state-of-the-art biomedical techniques and deep learning. Besides, I would like to thank my qualifying panel members, Prof. LI You Fu and Dr TIN Chung, for their insights and comments.

I would like to express my thanks to all members of Nano/Bio Robotics Laboratory. They are Dr KOH Keng Huat, Dr WU Guangfu, Dr LIN Zihong, Dr FANG Yuqiang, Dr YANG Runhuai, Dr TANG Xin, Mr FARHAN Musthafa, Miss LIU Yanfei, Dr GAO Qi, Miss ZHAO Ling, Dr LI Xiaoting Megan, Mr YANG Sheng Jie, Miss LIU Yanchen, Mr CHAN Pak Yu Colin, Mr SO Chun Ho Lucius, and Mr SHIU Kin Hei Ringo. I am grateful for your kind help when we were in the lab. I would like to thank the technicians, Mr LEE W.K., Mr CHENG S. W., Mr AU S. Y., and Mr KIAN K. C., for their kind assistance during the past years. I would like to thank Dr WONG Pat Lam Patrick of the Department of Mechanical Engineering and Dr CHOW Yuk Tak of the Department of Electronic Engineering to support my PhD application and my career. I am grateful to Prof. YUNG Kin Lam Ken of the Department of Biology, for providing a chance as a collaboration party to research the differentiation of neural stem cells. My grateful thank also goes to Mr LIU Zhe, Ms WONG Yee Ching, and Ms LIU Yee Lam for their help in the project of deep learning application on biological cell detection for patch clamp recording. In addition, I would like to thank Prof LI Wen Jung, for his kind help and advice. I would like to thank my friends in Prof. Li's research group, including Dr Ka Wai KONG, Mr Junhui LAW, and Dr JIA Boliang James.

Finally, I would like to dedicate this thesis to my family for their love, patience, understanding, and support. My dad and mum always give me the freedom to choose my life. My sister, Jackie, brother, Ryan, and sister-in-law, Tracy, always support and help me with all my needs. My heartfelt gratitude goes to my beloved husband, Simon, who always gives me support and love; my beloved daughter, Eira, who was inside my tummy when I was doing experiments and was my reason to chase and accomplish my dream.

Table of contents

Table of Figures

List of Tables

Chapter 1 Introduction

1.1. Background of ion channel activities

Ion channels are an essential part of living cells related to the physiological function of nearly all living organisms. The ion channel plays a fundamental role in cell signalling [1][2]. Ion channels are distinct protein structures that span the lipid bilayer of the cell membrane allow particular ions to pass from one side of the membrane to the other [3].

Various ion channels can be classified as either passive or active ion channels. Passive channels are always open, i.e. ions diffuse from areas of high concentration to areas of low concentration [4]. In the resting state of most cells, the extracellular sodium ion concentration is much higher than the intracellular solution, while the reverse is true for potassium ions. The ion flux through these passive channels contributes significantly to the resting potential [5].On the other hand, active ion channels lead to the firing of input energy called action potential (AP) to transport ions against the concentration gradients in responses to different physical stimuli, that is divided ion channels into three main categories which are voltage-gated, ligand-gated and mechano-gated, in responses to different physical stimulus. Those ion channel activities are illustrated in Figure 1.

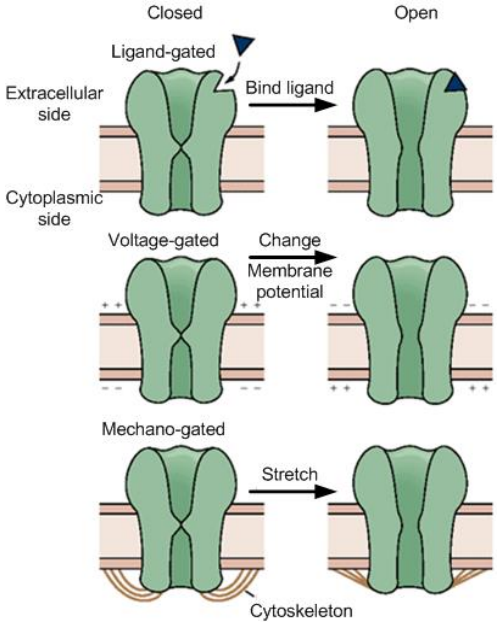

Figure 1. Three Types of Ion Channels [6].

In different parts of the nervous system, different types of channels carry out specific signalling tasks. Due to the key roles in electrical signalling, the malfunction or dysfunction of ion channels can cause various neurological diseases. Moreover, ion channels are often the site of the action of drugs, poisons, or toxins. Thus, the ion channels have crucial roles in both electrophysiology and pathophysiology [6][7]. Currently, there are approximately 400 kinds of ion channels are present in the human genome, and many of these ion channels have been implicated in many diseases; only approximately 50 channel pathways in humans are known and around 30% of those 50 channels are targeted by the drugs on the market [8].

To investigate the ion channels, the Patch clamp technique is a unique method for real-time measurements of ion channels functions at the single-molecule level and ion transporter functions at the level of a cluster of molecules [9]. The technique is now widely used in the field of ion channel research for many purposes, such as to monitor changes in the total membrane current, intracellular voltage or cell membrane capacitance etc. in a living cell at high time resolution [9]. To monitor the current change of the entire cell under the voltage stimulus, the whole-cell patch mode has been used for recording the membrane current from a cell under the voltage clamp. It is believed that the current recording from the cell can facilitate the understanding of cell signalling and hence can further apply to drug screening or diseases diagnosis.

1.2. The Patch clamp electrophysiology

Patch clamp electrophysiology is a technique of choice for the biophysical analysis of the function of nerve, muscle and synapse in Caenorhabditis Elegans nematodes[10]. Patch clamp is considered the “gold standard” for ion channel screening due to its unrivalled signal-to-noise ratio and temporal resolution [11]. The principle of the Patch clamp technique is to isolate a patch of membrane electrically from the external solution and to record the current flowing into the patch. In each recording, a fire-polished glass pipette filling with a suitable electrolyte solution is pressed again the surface of a cell with applying light suction to create a seal whose electrical resistance is more than 1 GΩ, called the gigaseal formation [12] [13], shown in Figure 2.

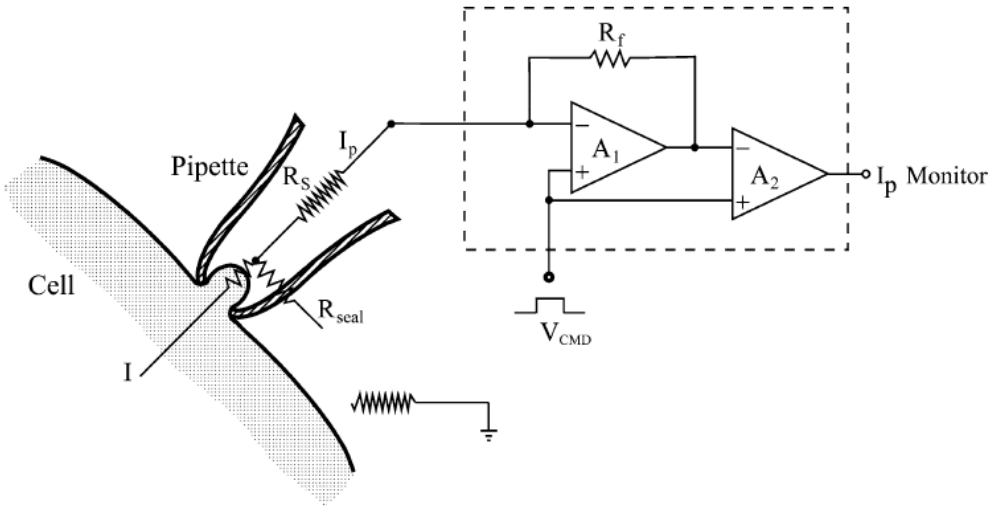

Figure 2. Principle of Patch clamp Technique [9].

R_S represents the series resistance (or access resistance) linked serially to the patch membrane resistance. R_{seal} means seal resistance. Usually, R_S is 1–5 MΩ [9]. When R_{seal} is more than 10 GΩ, $I_p/I = R_{seal}/(R_S + R_{seal}) \sim 1$ [9]. This I_p is detected as a voltage drop across the high-resistance feedback resistor (R_f) in the I –V converter circuitry (surrounded by *dotted lines*) [9]. Since the output of the operational amplifier (A_1) contains the command voltage (V_{CMD}), this is to be subtracted through the next operational amplifier (A_2) [9].

Figure 3 indicates several configuration/modes on the Patch clamp technique. The cell-attached mode is designed first to record single-channel currents [14]; the inside-out mode and outside-out mode are then developed for realizing the control of intracellular and extracellular environment during single-channel recording [15]. Subsequently, the open cell-attached inside-out mode [16] and the perforated vesicle outside-out mode [17] are invented. The conventional whole-cell mode [15] and the perforated patch mode [18] are designed for recording the total current across the whole membrane of a single cell.

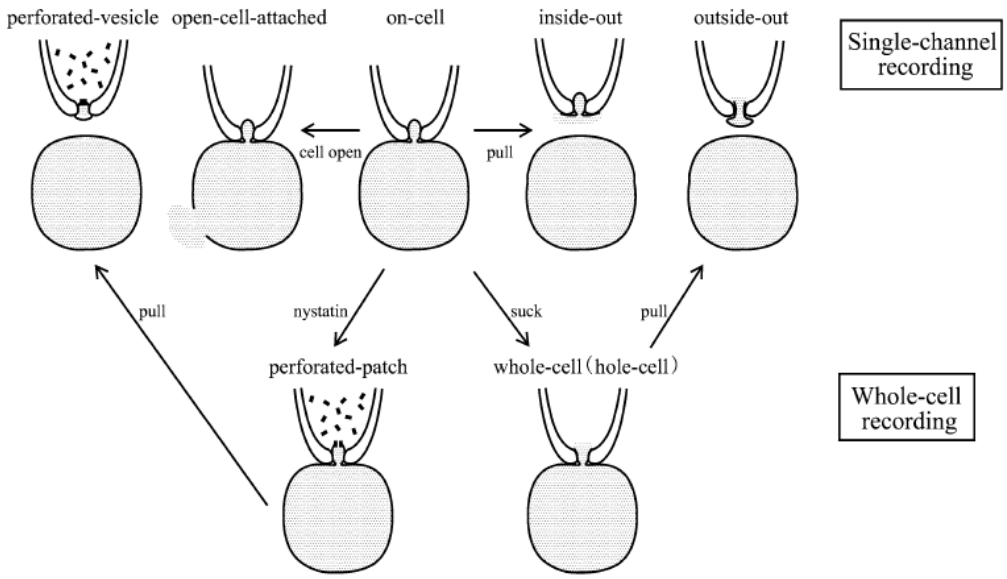

Figure 3. Different Kinds of Patch Configuration [13][19].

The Patch clamp allows investigation of the change of the state of neurons from resting potential to action potential and the functional properties of ion channels. It includes current clamp and voltage clamp and several configurations, including whole-cell recording and single-channel recording. The cell-attached mode records single-channel currents under gigaseal conditions. In this mode, channel activity is observed with minimum disturbance to the intracellular environment. However, intracellular conditions cannot be controlled directly, and the actual transmembrane voltage remains unknown because there is no information on the intracellular membrane potential [20][21].

When the patch membrane is ruptured after making the cell-attached configuration, the total current across the whole membrane of the cell can be recorded. This is called the “whole-cell” mode. In this mode, the intracellular milieu is dialyzed with the pipette solution, so both extracellular and intracellular conditions can be controlled. Furthermore, the intracellular membrane potential can be controlled or monitored reliably by voltage clamp or current clamp, respectively. Conventional Patch clamp is a very information-rich technique, but it requires skilled personnel to perform experiments, and typically, only one experiment can be performed at a time [22] due to the complicated operation and the specific skills are required. An example of a procedure for whole-cell recording is shown in Figure 4 [23].

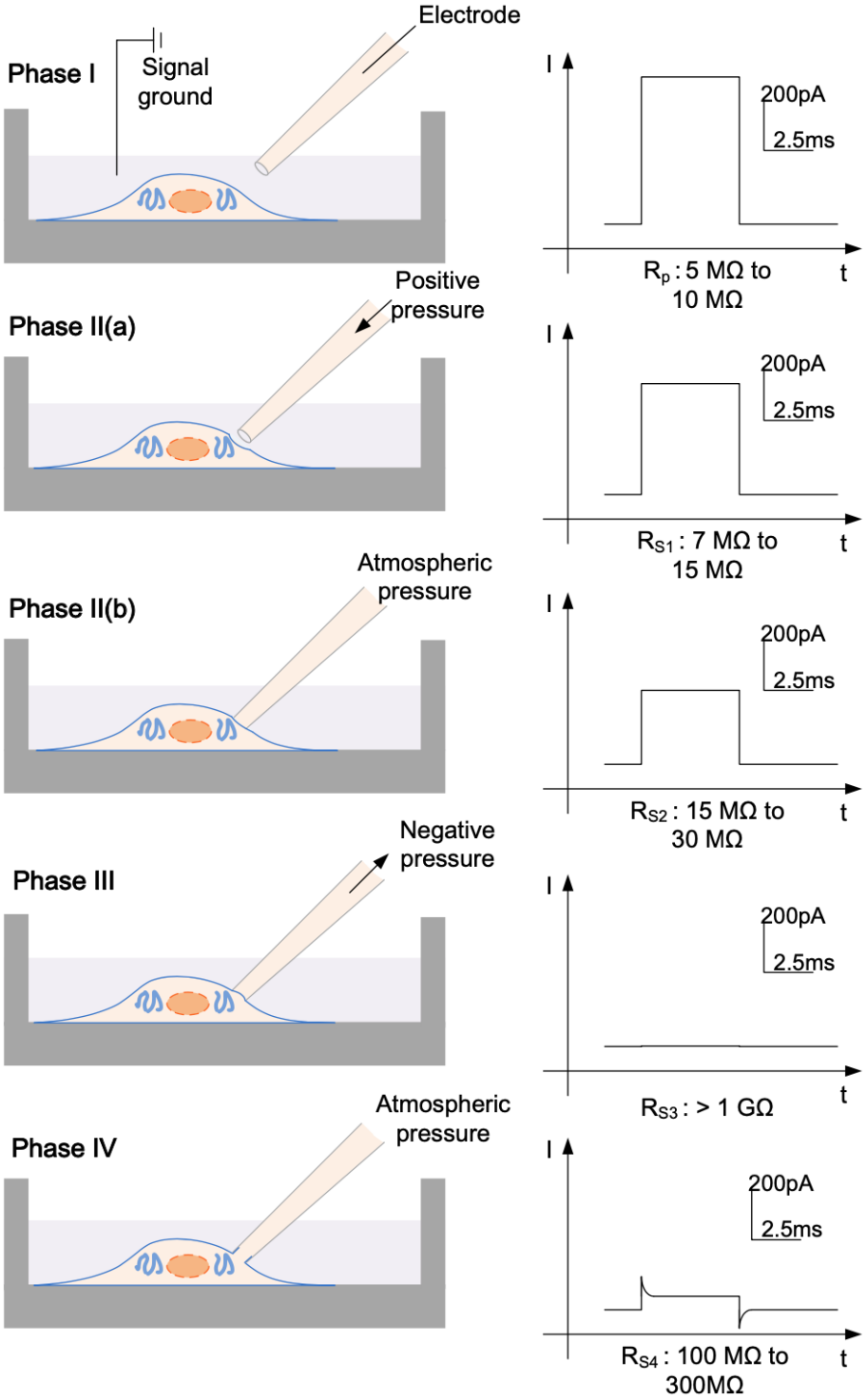

Figure 4. The five phases of the Patch clamp recording [23]

The five phases of the whole-cell recording involve locating a cell in good condition, manipulating a single micro-pipette filled with intracellular solution to approach the cell bathed in extracellular solution, controlling pressure applied on the cell membrane through the pipette to create the gigaseal configuration and then break-in the cell membrane in the tactic cells or tissues [24]. Despite the challenges of Patch clamp

recording, the ability to record ion channels activities led to the diverse development of automated Patch clamp (APC) systems [25]. To overcome the difficulties of the conventional Patch clamp systems, different APC systems have been proposed [26].

1.3. Microinjection of biological cells

Besides the patch clamp recording, cell microinjection is a another promising micromanipulation method in the study of biological fields [1]. Efficient tools to precisely inject drugs into cells are of significant value to the development of novel therapeutics [28]. It is also important for the study of cellular activity in biological fields [29]. Research activities in biological engineering such as drug screening and transfection require the precise manipulation of single biological cells [30]. Several methods, including drug delivery by either nano-vehicles or nanoparticles, may be used to penetrate the cell membrane and perform intracellular delivery [31][32]. In addition, viral vector-based methods are very effective to inject the target nuclide acid into various kinds of cells ranging from ex vivo transduction of hematopoietic cells to in vivo transgene expression through the optimization of tissue-specific. However, safety remains a great concern for gene therapies using the viral vector [33]. Besides, nano-needle is very efficient for delivering different molecules and materials including antibodies, quantum dots and nanoparticles to primary hippocampus neuron cells and NIH3T3 fibroblast cells which both of their sizes are around 100 μm in diameter [34]. Unfortunately, the injection performance on small adherent cells using the nano-needles is unknown at present.

To monitor the microinjection process, we are going to develop a current feedback approach for cell microinjection using the patch clamp technique. Further details will be discussed in Chapter 3 and Chapter 4, respectively.

1.4. Research motivation and objectives

Cell microinjection is one of the most common methods for intracellular delivery of various substances into cells, to apply in the field of drug deliveries and cell

transfection and gene therapy using human cells. Nevertheless, cell microinjection using a pipette always require a skilled operator to manipulate the pipette carefully and hence the efficiency of cell injection is low. In addition, it is quite challenging to determine whether the target material is injected into the cell spontaneously by observation, especially for cells that are small in the micron scale. Consequently, the applied force on the fragile cell membrane may be larger than necessary during the cell microinjection, which may lead to cell death. Cell viability is believed to be another important issue with great concern after the microinjection. Cell viability is commonly verified by using the vital stain. Observing the cell division using the fluorescent stain on the target cell was also reported to verify the cell viability. However, both methods cannot give the verification spontaneously.

The patch clamp recording is a powerful tool for the study of ion channel activities, but conventional Patch clamp is far too laborious. Automated patch clamp technologies have been steadily advancing over the past 15 years with a planar substrate, but the success rate of obtaining a current measurement is still not reliable for small and irregular cells, compared with the conventional Patch clamp with a pipette.

The research objectives are described as below:

1. To develop a current feedback approach for a cell cytoplasmic microinjection process with the patch clamp technique for small and non-spherical living cells
2. To develop an equivalent electrical model for monitoring the real-time current response during the microinjection and verifying the cell viability with the ion channel activities after the microinjection
3. To develop a deep learning approach for automatic detection of a suitable biological cell for the patch clamp operation to enhance the success rate of signal recording
4. To apply both voltage clamp recording and current clamp recording of patch clamp techniques to record the electrophysiological behaviours of induced pluripotent stem cell (iPSC) grown on biocompatible extracellular matrices (ECM) and hence verify if the neuronal stem cells (NSC) can be developed

1.5. Chapter summary

This chapter discusses the research background, motivation, and objectives. The scope of this dissertation covers the development of cytoplasmic microinjection with current feedback using the patch clamp technique, development of an electric model for monitoring cytoplasmic microinjection and cell viability verification of small and non-spherical living cells, development of an equivalent electric circuit for monitoring the consistent current response drop against different injection volume, development of a deep learning approach for cell detection and screening in patch clamp electrophysiology and application of the developed patch clam technique for electrophysiological study of neural stem cells (NSC) differentiation. The overall layout of the dissertation is illustrated in Figure 5.

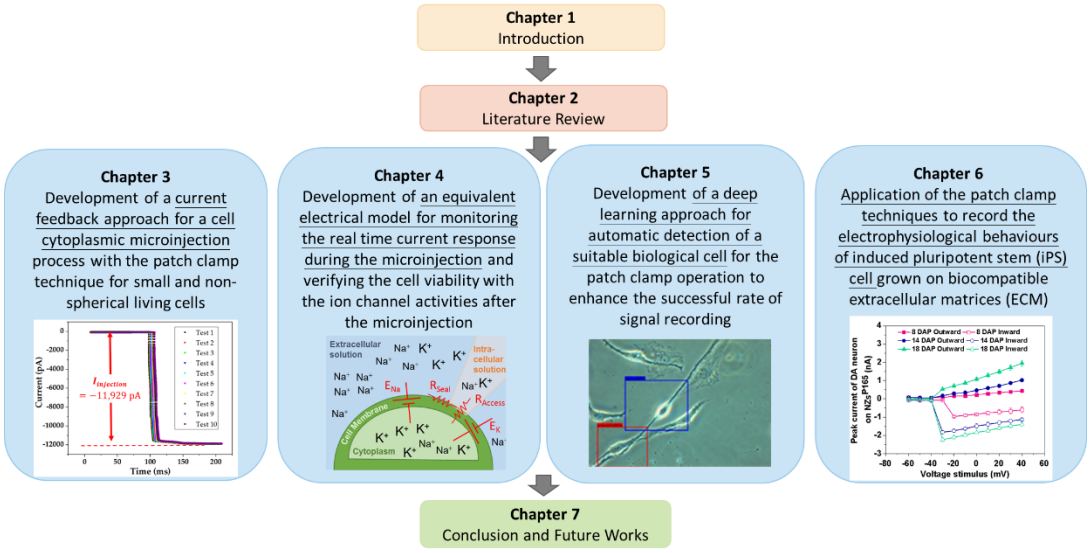

Figure 5. The overall layout of the dissertation

After the introduction, chapter 2 presents a literature review of cell microinjection with different feedbacks, automated patch clamp (APC) techniques and deep learning and convolution neural networks.

Chapter 3 presents the development of cytoplasmic microinjection with current feedback using the patch clamp technique and an electrical equivalent model for cell cytoplasmic microinjection and cell viability. The equivalent model for monitoring cell

cytoplasmic microinjection has been developed with the patch clamp technique to monitor the electrical signal of biological cells during microinjection. The electrical model for cell viability verification has been developed to explain the consistent current drop during microinjection. Besides, the electrophysiological recording was performed before and after the cell cytoplasmic microinjection to verify the cell viability.

Chapter 4 further investigates the electrical behaviour of cell microinjection for small and non-spherical living cells. The experimental results show a linear relationship between the current response of cell microinjection and different injection volumes. The results have been verified with the calculation of the involved current in the equivalent electric circuit converted by the electric model.

Chapter 5 introduces the deep learning approach for cell detection and screening in patch clamp for electrophysiology. A model of CELL-YOLO for biological cell detection has been developed. Data collection and labelling for the training dataset has been explained. Data augmentation of biological microscopic images has been discussed to enhance the data size for training. The loss curves of CELL-YOLO have been plotted to examine the training performance. The detection results and mAP of CELL-YOLO have been collected to verify detection accuracy and measure detection time. The testing results have been compared with YOLOV3 and YOLOV4

Chapter 6 reveals the application of the developed patch clamp technique for the electrophysiological study of neurological behaviour of neural stem cells (NSC) after differentiation. The current response detection of differentiated NSC was recorded using a voltage clamp, and the membrane potential change was monitored using the current clamp. The peak current density tracking against voltage stimulus of NSC was studied in a differentiation cycle.

Finally, the conclusions and future works are provided in Chapter 7.

Chapter 2 Literature review

2.1. Micropipette-based microinjection

Micropipette-based microinjection is a process for the delivery of foreign materials by penetrating living cells using a micropipette. The foreign materials are various, ranging from RNA, DNA, protein, sperm, toxins and drug, which are broadly used in cell transfection, drug screening and other biomedical applications [35][36][37]. Molecule screening at a single cell level is crucial in drug discovery so that the cellular function of the target molecules inside the cell can be controlled [38]. At present, conventional microinjection is still operated manually under a microscope with a fine glass micropipette [39][40].

It was proven to work effectively and has the advantages of precise control of delivery dosage and high transduction efficiency [41]. However, the drawbacks of pipette-based methods are time-consuming and require a well-trained operator, resulting in costing a lot of time and money [42]. During the cell microinjection, the micropipette is manipulated to approach a single living cell and then penetrate the cell membrane with a micromanipulator [42]. Then, a micro-injector is used to inject the foreign materials into the cell. The entire process is mainly controlled by operators with direct or indirect observation under a microscope. Therefore, a skilful operator plays a key role in the success of cell microinjection. The abovementioned concerns have led to the demand for automatic pipette-based cell microinjection to increase the success rate and reduce human errors [43]. Several automated cell injection approaches with different kinds of feedback have been reported, including force feedback, impedance feedback and visual feedback.

2.1.1. Microinjection with force feedback

The microNewton force feedback approach has been reported to largely improve the work efficiency and success rate of microRNA and DNA injections to suspended mouse embryos (around 100 μm in diameter) and zebrafish cells (1.3 mm in diameter) [44]. Polyvinvylidenedback (PVDF) film as a piezoresistive force sensor is used for

force feedback to monitor the injection process when injecting zebrafish embryos [45]. For smaller cells, the penetration force analysis of several cell lines, L929, HeLa, 4T1, and TA3-HA-II cells, is demonstrated using atomic force microscopy (AFM) [28], which helps the researcher to understand the cell mechanics.

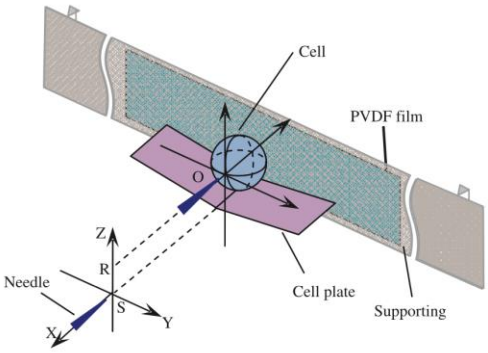

Figure 6. The force-based cell injection and sensing scheme [45].

Cell type	Range of penetration force	Percentage of penetration
L929	3-6 nN, 18-22 nN	19.6 % (9/46), 21.4 % (6/28)
HeLa	2-13 nN	41.7 % (15/36)
4T1	2-17 nN	5.8 % (4/ 69)
TA3 HA II	3-9 nN	12.8 % (6/47)

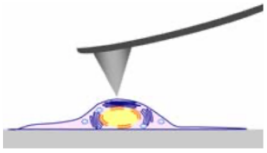

Figure 7. Penetration force analysis for cell injection using AFM with Si tip [28].

2.1.2. Micro-injection with voltage and impedance feedback

Impedance feedback for a robot-assisted cell microinjection system performed on zebrafish fish embryos is introduced to enhance the accuracy of the system feedback [28][46]. Utilizing the voltage feedback of the piezo-actuator, a design of the piezo-driven cell injector is introduced in cell injection of zebrafish embryos at the suspended state with a comparably high survival rate of over 80% [47].

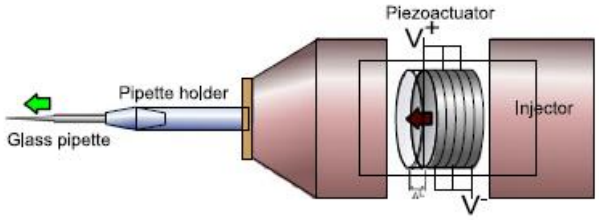

Figure 8. Design of the piezo-driven cell injector [47].

2.1.3. Micro-injection with visual feedback

A vision-based force measurement for cell microinjection is performed on mouse oocytes (around 100 μm in diameter) and drosophila embryos (around 500 μm in diameter) [48]. The relationship between the dimple angle and the injection force is found to be polynomial, as shown in Figure 9.

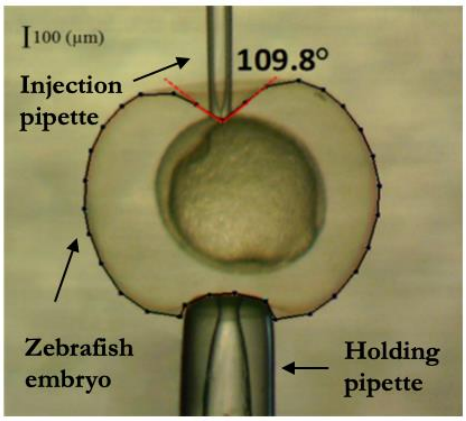

Figure 9. The dimple angle formed in the cell deformation during the micro-injection of a cell [48]

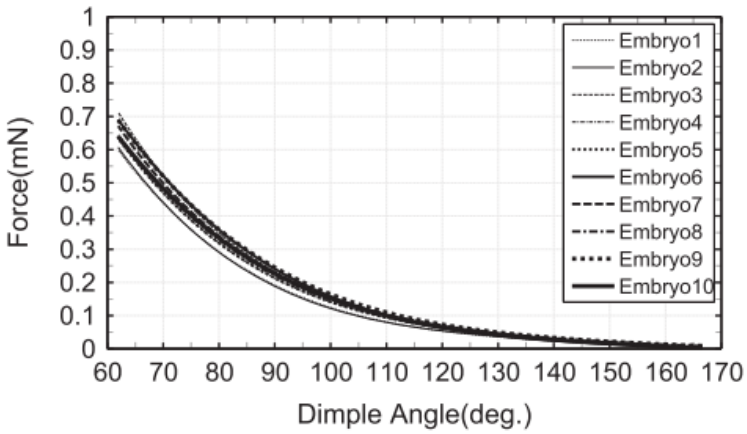

Figure 10. The fitted curves of the data sample between the dimple angle and the injection force [48]

While a visual-based system with impedance control for cell injection has been reported to perform on Zebrafish embryos [49], some researchers suggest that visual feedback may be a possible solution for the micro-injection of small cells with a

diameter of less than 100 μm [50]. However, another challenge that arose from visual feedback is the difficulty in observing the contact between the tip and the cell to determine the penetration status. In recent years, more genetic research has driven the demand for automated cell microinjection systems, and some in vitro cell microinjection systems have been reported in a review[51]. All of the microinjection systems mentioned are for suspending cells in an oval shape. Nevertheless, some typical human cells are adherent and small such as neuroblastoma cells and human epithelial cells. Recently, an automated injection system for suspending small cells (diameter < 30 μm) has been reported, which is operated with a microfluidic cell holder chip [43][52]. Small adherent cells are of importance in cell biology because the size of human cells, which is usually ranging from 7 μm to 25 μm, and also cell transfection using human cells with precise delivery of target materials is challenging to operate, but have a great demand to be automated [43]. In the past, other research groups focused on the automated injection of large and round cells such as zebrafish embryos [30][41][53][54][55][56]. In contrast, there are relatively few numbers of researches about the automated injection of small adherent cells [56]. For instance, SHSY-5Y cells (human neuroblastoma cells) are used frequently for studying Alzheimer's disease. HEK-293 cells (human embryonic kidney cells) are used frequently for studying gene therapy. However, it is more difficult to implement either manual or automated injection on the human cells due to their small size.

To overcome the challenges, a current feedback approach is proposed to work for automating the micro-injection of neuronal cell line (<30 μm). In this study, an equivalent electrical model has been established to monitor two situations. The real-time current response during the microinjection was studied for the effectiveness of the injection. In addition, the current trace under voltage stimulus was recorded to verify the viability of the cells after microinjection.

2.1.4. Micro-injection for small adherent cells

In recent years, several small adherent cells with a diameter of < 30 μm) are considered as typical models in pathological studies, such as HEK293 [57], N2A [58] and SHSY5Y [59] even though they are difficult to manipulate due to its fragile feature

and irregular form. Therefore, cell microinjections on small adherent cells are of great importance in various biomedical studies. Nevertheless, it is more challenging to perform microinjection to small adherent cells because their size is nearly 5 to 10 times smaller than that of oocytes and hence more accurate control in terms of positioning and injection accuracy of micropipette is demanded [40]. In other previous studies, visual-based controls [60] or force-based controls [39] have been proposed to enhance injection accuracy and the ease of operation, and a fully automated microinjection system has been thus developed for zebrafish cells [61]. The visual control approach involves auto-focusing, identification and position control of cells and injection pipette [62]; the force sensor is used to detect the contact between the target cell and the pipette [63]. Despite the claimed advantages, the abovementioned approaches have been limited to the application of the microinjection process for large and spherical cells such as zygotes, oocytes and zebrafish cells. The visual feedback mechanism is difficult for small and irregular shape cells due to the complicated algorithm to cope with small and irregular shape features. Force feedback may be another method to enhance the automation level, but it cannot provide adequate sensitivity to detect a force change during cell microinjection of small adherent cells. Therefore, we propose a new monitoring approach to validate the cell microinjection quantitatively via observing the change of electrical signal across the cell membrane in real-time. In our previous study, an electrical model is established to explain the relationship between electrical signal change across cell membrane and the cell microinjection process [64].

2.2. Automated Patch clamp technique

The patch clamp technique is widely used in electrophysiological studies and provide direct quantified data of ion channel activities in real-time at high fidelity in the scale of pico-ampere. This technique can monitor the interaction between a drug and a specific ion channel and hence understand the biophysical mechanisms of pathology and biological computation [26]. The patch clamp technique is regarded as a gold standard for ion channel research, inevitably with the drawbacks of low throughput and high personnel costs. In the last decade, the development of several automated patch clamp (APC) systems has greatly increased the throughput of whole-cell

electrophysiological recordings [26]. The current APC systems are divided into three main categories: (1) the glass pipette-based APC system; (2) the micro-fabricated planar electrode-based APC system; and (3) the automated two-electrodes voltage clamp (TEVC) on Xenopus oocytes [65].

2.2.1. The glass pipette-based APC

Glass pipette-based APC systems are proposed in different approaches. The first approach is to move a pipette to contact the surface of a randomly chosen cell suspended in one or more cell layers in a density-gradient solution or a random cell of brain tissue [1]. In the second approach, a tiny pipette is vertically positioned upwards while the suspended cells are attached to the opening of the pipette tip randomly. In the third approach, suspended cells flow through a glass pipette to the inside of the pipette's tip [67]. Those approaches have the same drawbacks that limit the choices of cell types to the suspended cells. Moreover, the cell is selected blindly, so it is quite challenging to patch a target cell.

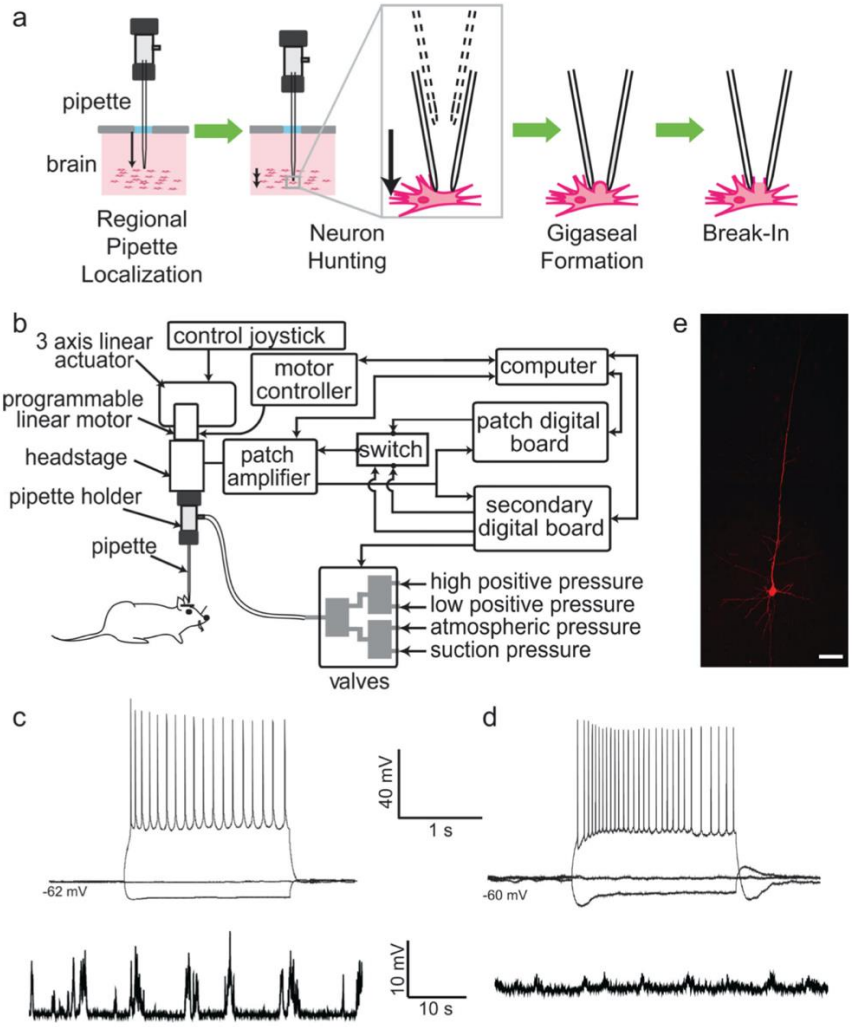

Figure 11. APC using micro-pipette performing the whole-cell recording a neuronal tissue of a mouse in vivo. (a) the operation sequence of a micro-pipette electrode-based patch clamp. b) Schematics of the APC with the key components. (c) the voltage firing under the applied current from -60 pA to + 80pA. (d) the voltage firing under the applied current from -60 pA to +40 pA. (e) a cortical neuron as a target cell.

2.2.2. The micro-fabricated planar electrode-based APC system

Another type of APC system is based on a micro-fabricated planar electrode, which utilizes microfabrication of silicon or plastic-based planar arrays with micron-size holes that allow loose or tight seal formations [68]. Although the planar APC system can significantly increase throughput and several commercial APC systems are employing this technique, it also has a limited choice of cell types. Those planar type APC systems are designed to use stable cell lines that express a single ion channel type in large quantities, whilst the primary cells, differentiated cells derived from induced pluripotent stem cells (iPSCs), embryonic stem cells (ESCs) or transiently transfected

cells with low expression levels of ion channels are difficult to be used using this technique [26][69]. The schematics of a planar electrode-based patch clamp is shown in Figure 12 [70]. During the operation, the cell hunting is performed by suction and then a cell-attached configuration.

Furthermore, the TEVC is designed for studying ion channels expressed in Xenopus oocytes only, which are not widely used for drug discovery [71]. Due to the various limitations of different APC systems, the current APC cannot entirely replace the manual patch clamp, especially for the study in a wide range of cell types, which are not suspended, or the cell is with irregular and unique cell morphological features.

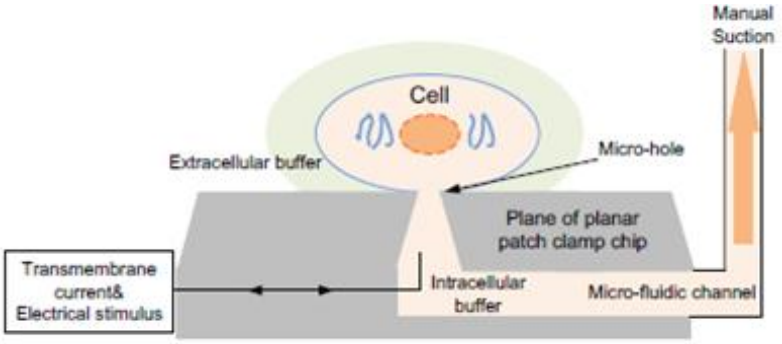

Figure 12. The illustration of a planar electrode-based patch clamp [70].

Another challenge of both the manual patch clamp technique and APC system is to control the cell condition of a single cell to be patched because the cell condition is one of the main keys to the success of the patch clamp operation. In most APC systems, a target cell is randomly selected, so the cell condition cannot be guaranteed since the cell condition can be varied in the same batch of the cell culture [26]. In contrast, the target cell of the manual patch clamp under the microscope can be selected by the operator, but the success rate of selecting a suitable cell for the patch clamp operation is highly dependent on the skills of the operator, and a skilled operator is expensive and required years of experience. To enhance the success rate and the efficiency of the patch clamp technique, APC with object detection of a unique and specific biological cell is highly desired with high accuracy and high throughput.

2.3. Deep learning-based object detection

Object detection is one of the key areas in the fields of computer vision and deep learning. The two main tasks of object detection are object localization to determine the location of an object target within an image and object classification to recognize the categories of the target object [72]. Traditionally, object detection is divided into three steps: (i) proposal generation to search the region that may contain the object in an image with sliding windows; (ii) feature vector extraction to capture discriminative semantic information of the covered region; and (iii) region classification to assign categorical labels to the covered regions [73]. Inevitably, this working mechanism has led to various drawbacks. Redundant proposals are generated, and hence a significant number of false positives are produced. Since the feature descriptors are designed manually with low-level visual cues, it is difficult to locate the representative features information in complicated images [74] [75][76]. A globally optimal solution for an entire system cannot be acquired because every step of the detection pipeline is designed and optimized individually[73]. In contrast, the performance of object detection is significantly improved after employing the convolutional neural network of deep learning techniques[77].

Deep learning is a computational model composed of multilayers neural networks and backpropagation to learn representations of data with multiple levels of abstraction. The working principle of deep learning is to learn to map a fixed-size input to a fixed-size output through forward-propagation of a neural network from the input layer to the output layer through the hidden layers. During the feedforward process, a set of units compute a weighted sum of their inputs from the previous layer and pass the results to the next layer through a non-linear activation function [78]. Typically, the rectifier linear (ReLU) function is the most commonly used since the learning process of a ReLU function is much faster in a very deep neural network when compared with other non-linear functions such as tanh(z) and 1/(1+exp(-z))[79]. In backward propagation of a neural network, an objective function is used to measure the error between the output scores and the desired pattern of scores through a procedure is called stochastic gradient descent (SGD), as shown in Figure 13 [78].

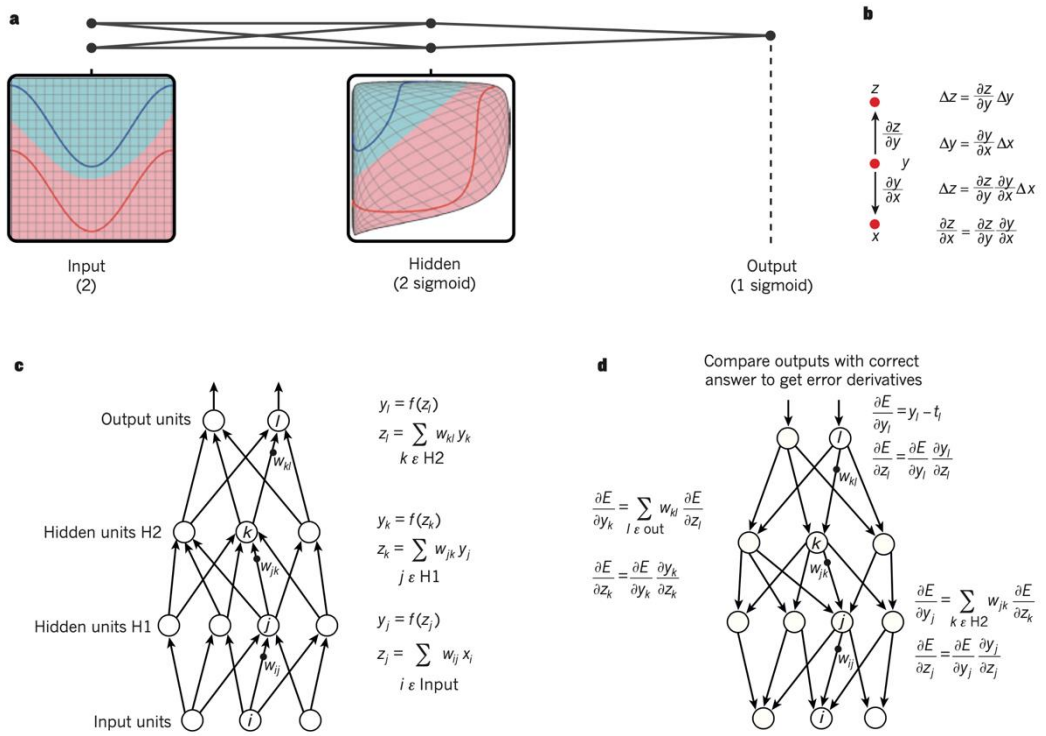

Figure 13. Deep learning model with multilayer neural networks and backpropagation. (a) Multilayer neural networks with two input units at one input layer, two hidden units at one hidden layer and one output unit at one output layer. (b) The chain rule of derivatives as a basic unit functioning at the forward propagation and backward propagation. (c) The objective functions are used for computing the forward propagation of a neu with two hidden layers. (d) The gradient descent function for computing the backward propagation to find out the error derivatives with respect toral network the output of each unit in the neural network [78].

Constructing with more hidden units and hidden layers, the neural network becomes deeper in the structure, and hence it is called deep learning or deep neural networks. Different deep neural networks are constructed for various applications, as shown in Figure 14 [78]. Particularly, a kind of neural network framework called convolutional neural network (CNN) is used for computer vision applications, including image classification and object detection.

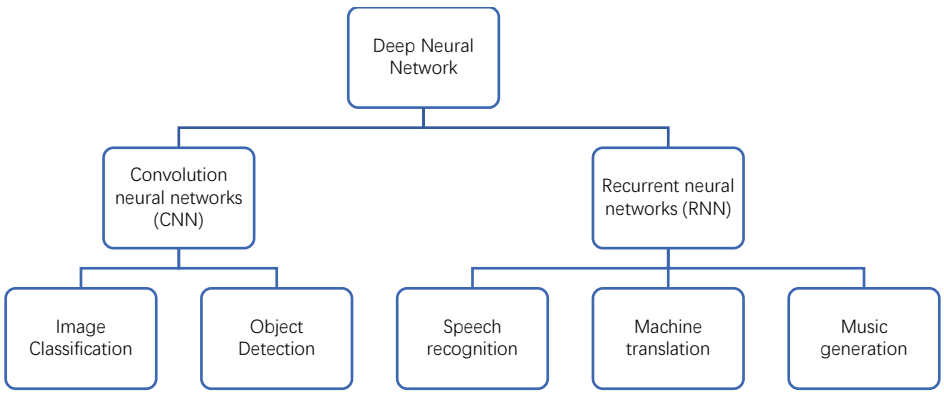

Figure 14. Classification of deep neural networks and their application.

2.3.1. CNN for image classification

CNN has been developed for processing data in the form of multiple arrays. For image processing, the input data of an image is three 2D arrays with pixel intensities in three RGB colour channels: red, green, and blue. The basic structure of a CNN is composed of convolution layers, pooling layers and fully connected layers, as shown in Figure 15 [78][73] to conduct different data transformations. In Figure 15, the image processing is being computed from the bottom upwards. Units in convolution layers are designed as feature maps or filters to compute the data from the previous layer [72]. The convolution or filtering operation is used to convolute the values of the receptive units with the learned weight and take a ReLU function to obtain the output [72]. Pooling operation such as average pooling and max pooling is used to summarize the response of the receptive units into one value to produce a more robust feature description [72]. In recent years, different network structures have been developed, and their image classification performances have been well-proven in the largest scale image classification contest called ImageNet Large Scale Visual Recognition Challenges (ILSVRC) to classify over 1.2 million images from the largest image database called ImageNet [73], [77], [78] as shown in Figure 16.

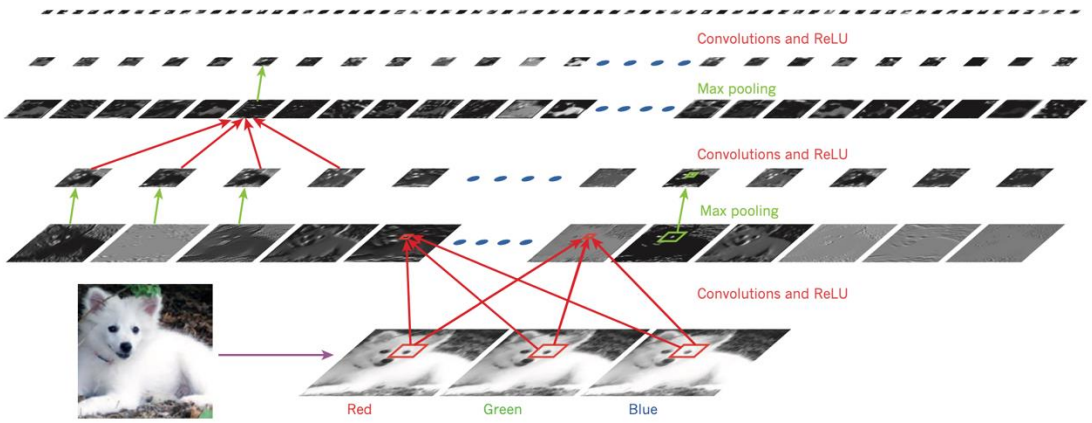

Figure 15. The structure of a convolution neural network

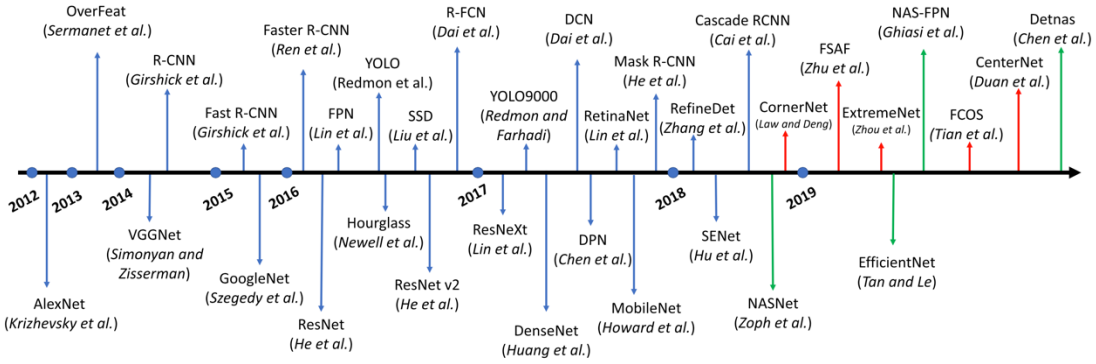

Figure 16. The development of classic convolution neural networks for image classification (at the bottom) and object detection (at the top) starting from 2012 [73]

Some of the classific CNNs for image classification became the standard modules of deep learning application due to their specific contribution to a significant improvement of image classification in terms of speed and accuracy.

The breakthrough of AlexNet is to introduce non-saturating neurons for faster training and dropout regularization to reduce overfitting in the fully connected layers [77]. Afterwards, VGG is developed by the Visual Geometry Group of Oxford University, has proved the advantages of using a smaller filter that is a 3 × 3 convolution filter with a stride of 1 over AlexNet using an 11 × 11 convolution filter with a stride of 4. Using a 3 × 3 convolution filter can make the decision function more non-linear and the data extraction operation more systematic [80]. VGG-16 and VGG-19 are typical VGG networks using 16 and 19 weight layers, respectively. VGG-16 and VGG-19 have 13 and 16 convolutional layers, respectively, and they both have 3 fully connected layers and 3 max-pooling layers. After VGG-Net, two classic building blocks of CNN are developed: residual network (ResNet) from Microsoft and the inception module of GoogLeNet from Google. In a residual learning model, a plain network inspired by VGG-19 is constructed and a shortcut connection is proposed to reduce optimization difficulties, as shown in Figure 17[80]. As a ResNet, a layer could skip the nonlinear transformation and directly pass the input from the previous layer to the next layer. Compared with VGG-19 (19.6 billion), ResNet can successfully reduce the top-1 error with significantly less floating-point operation per second (FLOP) in the entire structure[80]. Shortcut connection creates a highway to directly pass the gradients from deep layers to shallow units, reducing training difficulty significantly. Using residual blocks, the model depth of a training network could be increased

tremendously (e.g. from 16 to 152), allowing us to train very high capacity models [73]. Another 22 layers deep network called GoogLeNet, developed by Google, became the next champion of ILSVRC in 2014. In GoogLeNet, an important module called inception is introduced with embedded different scale convolution kernels (1×1, 3×3, and 5×5) on the same feature map in a given layer as shown in Figure 18. Compared with VGGNet, the computational cost of the Inception structure is much lower; the inception captures multi-scale features and summarizes these features together as an output feature map. The development of the inception module from Inception v2, Inception v3 [81], Inception v4 to Inception-ResNet [82] is continued by adding the batch normalization operation, rearranging the different sizes of convolution kernels and integration with residual blocks. The introduction of residual connections leads to dramatically improved training speed for the Inception architecture[82].

The abovementioned network structures are all initially designed and trained for image classification using the ImageNetg database. For initialization of the model used for object detection, those CNNs have been introduced as backbone networks for different detection paradigms. Directly applying the trained model for classification on object detection tasks can lead to poor detection problems due to the conflicts arising from the features discrimination between the classification and detection.

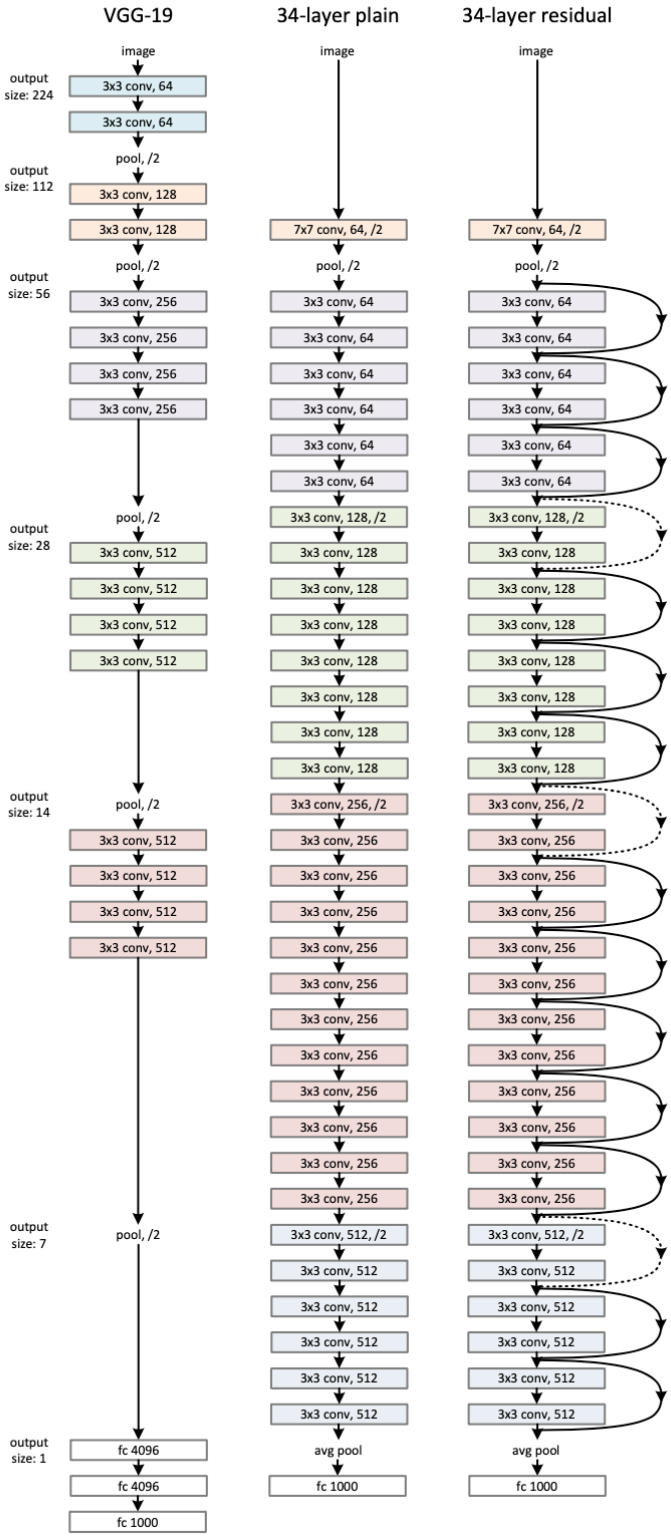

Figure 17. Left: the VGG-19 model [80] as a baseline. Middle: a plain network with 34 parameter layers. Right: a residual network with 34 parameter layers.

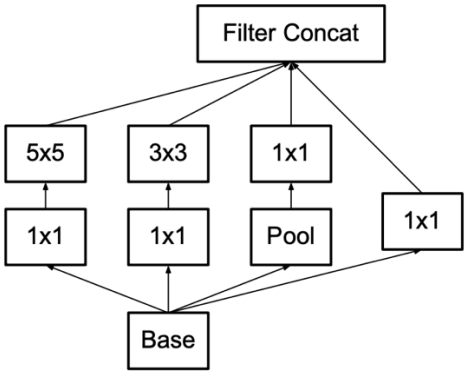

Figure 18. The original inception module

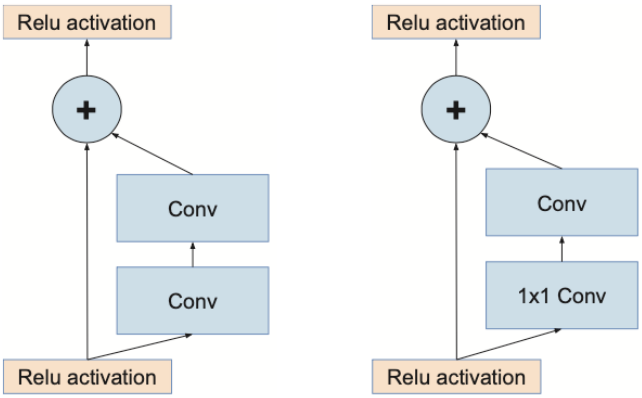

Figure 19. Residual connection (left: typical residual connection[83], right: optimized residual connection using 1x1 convolution block[82])

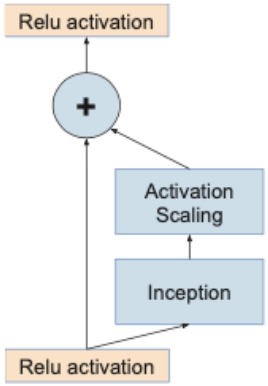

Figure 20. The unit block of the Inception-Resnet Model[82]

2.3.2. CNN framework for object detection with deep learning

Recent CNN based object detectors can be mainly divided into two main categories: two-stage detectors such as RCNN [84], spatial pyramid pooling network (SPP-net), Fast RCNN [85], Faster RCNN [86] and R-FCN [87], as shown in Figure 21 and one-stage detectors such as you only look once (YOLO) [88] [89] [90][91], single-shot multibox detector (SSD) [92], RetinaNet [93] and CornerNet [94] as shown in Figure 22.

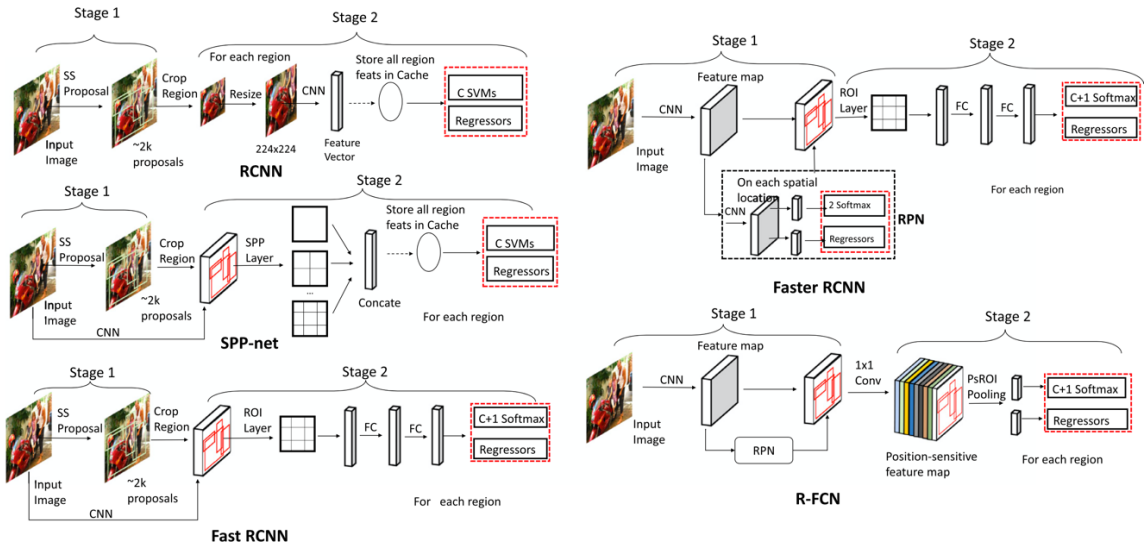

Figure 21. The framework structure of two-stage detectors[73]

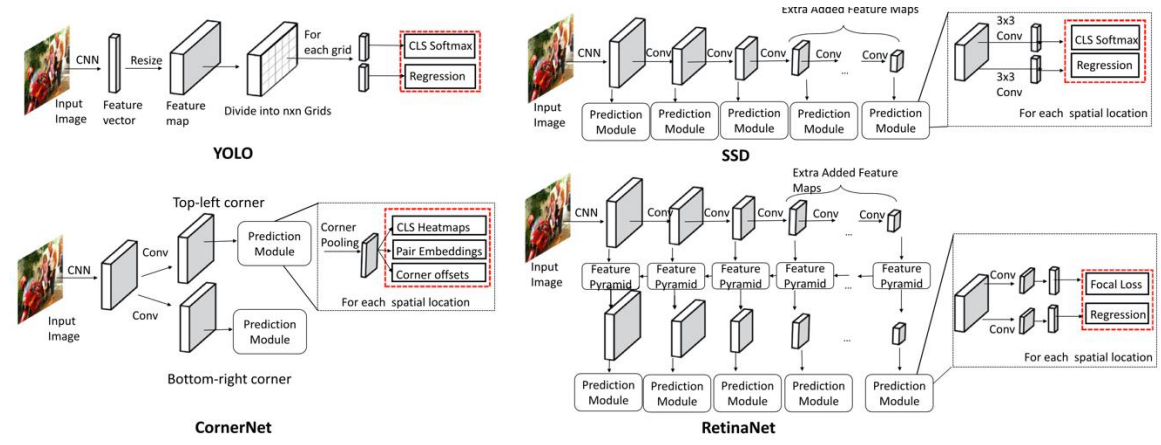

Figure 22. The framework structure of one-stage detectors[73]

A two-stage object detector, or called region-proposed-based detector, uses the framework with a two-stage process [73] [38]. The first stage is region proposal generation to propose regions in the image with a high recall, and hence all objects in the image belong to at least one of these proposed regions. The second stage is to

classify these proposals with the right categorical class labels using CNN for image classification. In contrast, a one-stage object detector, called a global-classification-based detector, does not have a separate stage for proposal generation; they generally consider all positions in the image as potential objects and classify each region of interest as either background or a target object[73] [38]. In general, the detection precision of a two-stage detector is higher than a one-stage detector, while the processing time of a one-stage detector is much faster and applicable to real-time object detection because it eliminates proposal generation and subsequent pixel or feature resampling stages and encapsulates all computation in a single network[92].

2.4. Chapter summary

This chapter has shown the recent development in three main sections: cell microinjection with different feedback, automated patch clamp techniques, and deep learning techniques for object detection. After reviewing the literature, cytoplasmic microinjection with current feedback using the patch clamp technique for small and non-spherical cells, an equivalent electrical model for monitoring the real-time current response during the microinjection and verifying the cell viability with the ion channel activities after the injection, and a specific deep learning-based algorithm for automatic detection of a suitable and healthy cell for reducing the operational challenges of the patch clamp technique has been developed. After that, the developed patch clamp technique has applied to record the electrophysiological behaviours of induced pluripotent stem (iPS) cells grown on biocompatible extracellular matrices (ECM) and hence verify if the neuronal stem cells (NSC) can be developed on ECM.

Chapter 3 Current-feedback approach for a cell cytoplasmic microinjection process with the patch clamp technique for small and non-spherical living cells

To monitor the electrical signal of biological cells for microinjection, an electric equivalent model of a cell cytoplasmic microinjection with a micro-pipette has been proposed, as illustrated in Figure 23. The electric model was developed to find out the significant factor of current that can align with the experimental results. This chapter describes the electric model and the key parameters and shows the experimental results of the current responses during the microinjection. We found that the current responses were related to the key parameters of the electric model. More calculations will be provided in the next chapter.

In Figure 23, a cell interacting with a micro-pipette can be regarded as an electrical circuit containing several electrical components. E_{na}, E_K, and $E_{other\ ions}$ are the equilibrium (Nernst) potentials of Na^+, K^+, and other ions between the cell membrane. In normal conditions, E_K and E_{Na} are about −90 mV and +60 mV [95] due to the concentration difference between the outer and inner fluid of living cells. Naturally, the external fluid usually contains 0.44 M of Na^+, and the internal fluid, which is the cytoplasm, usually contains 0.5 M of K^+ and some unspecific anions such as phosphates, amino acids, and negatively charged proteins [96]. In this study, cells are bathed in the buffer solution as the outer fluid of living cells, called the extracellular solution. Meanwhile, another solution is prepared as the fluid being injected into the inner fluid of living cells, called an intracellular solution.

The capacitance (C_M) of the cell membrane exists due to the different concentrations of total ions between the outer and inner fluid. The glass layer structure of the pipette acts as a capacitor, $C_{Pipette}$, which gives the capacitance transient curve when the micropipette is immersed in the extracellular solution. The capacitance transient curve can be neutralized by injecting the opposite capacitance current via adjustment with the observation of the electrical signal. R_{na}, R_K, and $R_{Other\ ions}$ are the variable resistances of the ionic currents contributed by Na^+, K^+, and other ions,

respectively. Their resistances vary because the various ions (Na^+, K^+, and other ions) pass through the cell members when the corresponding ion channels are activated under a different stimulus [95]. R_{Seal} is the resistance due to the formation of a tight and strong seal between the cell surface and the pipette before the microinjection. Access resistance (R_{access}) results from the geometry of the pipette and any obstruction at the tip by the adherent membrane [97].

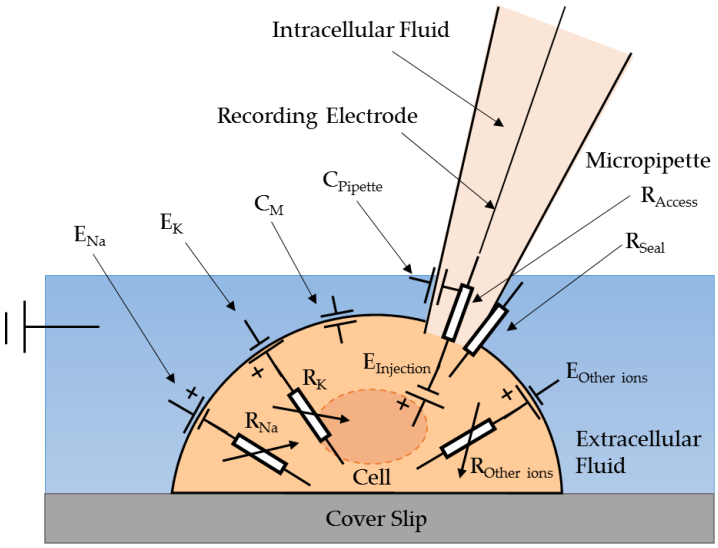

Figure 23. The electric equivalent model of the cell cytoplasmic injection.

3.1. The equivalent model for the cell cytoplasmic microinjection

In the model, $E_{Injection}$ is hypothesized to exist when the intracellular solution is injected into a cell using a micropipette. It is believed that the injection will cause a significant change in the membrane potential because of the change of ion concentrations across the membrane. During the injection, the injected intracellular solution immediately mixes with the cytoplasm of the cell leading to a change of ion concentration in the cytoplasm, while the concentration of the extracellular solution remains unchanged. $E_{Injection}$ can be expressed as shown in Equation (3.1). $E_{Cell\ Membrane}$ can be calculated by the Nernst Equation, as shown in Equation (3.2):

$$\boldsymbol{E_{Injection} = New\ E_{Cell\ Membrane} - Old\ E_{Cell\ Membrane}} \qquad (3.1)$$

where *New* $E_{Cell\ Membrane}$ is the membrane potential after the injection, and Old $E_{Cell\ Membrance}$ is the membrane potential before the injection:

$$\boldsymbol{E_{Cell\ Membrane} = \sum_{j=0}^{n} \frac{RT}{ZF} ln \frac{[ion_j]_o}{[ion_j]_i}} \tag{3.2}$$

where R is the ideal gas constant, R = 8.314472 J K^{-1}·mol^{-1}, T is the temperature in kelvins, F is Faraday's constant (coulombs per mole), F = 9.648533 × 10^4 C·mol^{-1}, $[ion]_o$ is the extracellular concentration of that particular ion (in moles per cubic meter), $[ion]_I$ is the intracellular concentration of that particular ion (in moles per cubic meter), and Z is the number of moles of electrons transferred in the cell reaction or half-reaction. By taking into consideration all the ions of the intracellular solution, $E_{Cell\ Membrane}$ can be expressed as shown in Equation (3.3).

$$\begin{aligned} \boldsymbol{E_{cell\ membrane}} &= \boldsymbol{\frac{RT}{(+1)F} ln \frac{[Na^+]_o}{[Na^+]_i} + \frac{RT}{(+1)F} ln \frac{[K^+]_o}{[K^+]_i}} \\ &+ \boldsymbol{\frac{RT}{(+2)F} ln \frac{[Mg^{2+}]_o}{[Mg^{2+}]_i} + \frac{RT}{(-2)F} ln \frac{[Cl^{2-}]_o}{[Cl^{2-}]_i}} \\ &+ \boldsymbol{\frac{RT}{(Z)F} ln \frac{[Other\ ions]_o}{[Other\ ions]_i}} \end{aligned} \tag{3.3}$$

where $\boldsymbol{\frac{RT}{(Z)F} ln \frac{[Other\ ions]_o}{[Other\ ions]_i} \cong 0}$, since the concentration of ion is very small.

Since the major injected ions are K^+ and Na^+, the equation of cell membrane potential can be simplified in Equation (3.4).

$$\boldsymbol{E_{cell\ membrane} = \frac{RT}{(+1)F} ln \frac{[Na^+]_o}{[Na^+]_i} + \frac{RT}{(+1)F} ln \frac{[K^+]_o}{[K^+]_i}} \tag{3.4}$$

To study and verify this electrical model, the patch clamp technique was used with a low noise operational amplifier that can apply voltage stimulus for controlling the voltage potential of the cell membrane, called the membrane potential (V_m). It can also acquire the total current response of the cell membrane, called the membrane current (I_m).

When a cell is connected to the operational amplifier, the electric equivalent circuit of the cell cytoplasmic microinjection is constructed, as shown in Figure 24. The operational amplifier acts as a voltage source (E_{OpAmp}) in series with a resistor (R_{OpAmp}) to apply the voltage stimulus, which can evolve the ion flow along the ion channels. There are five switches in the circuit, including the switch (S_{seal}) for the sealing resistance and the switch ($S_{Injection}$) for the microinjection of the cell. In this circuit, S_{seal} is always open as R_{Seal} is extremely large compared with other resistances, and hence the connection to R_{Seal} will act as an open circuit. The function of the switch ($S_{Injection}$) for the microinjection of the cell is to connect the $E_{Injection}$ when the intracellular solution is injected into the cell. S_K, S_{Na}, and $S_{Other\ ions}$ act like the switches to connect R_{Na}, R_K, and $R_{Other\ ions}$, which will be the maximum when there is the least ion channel activity, and vice versa.

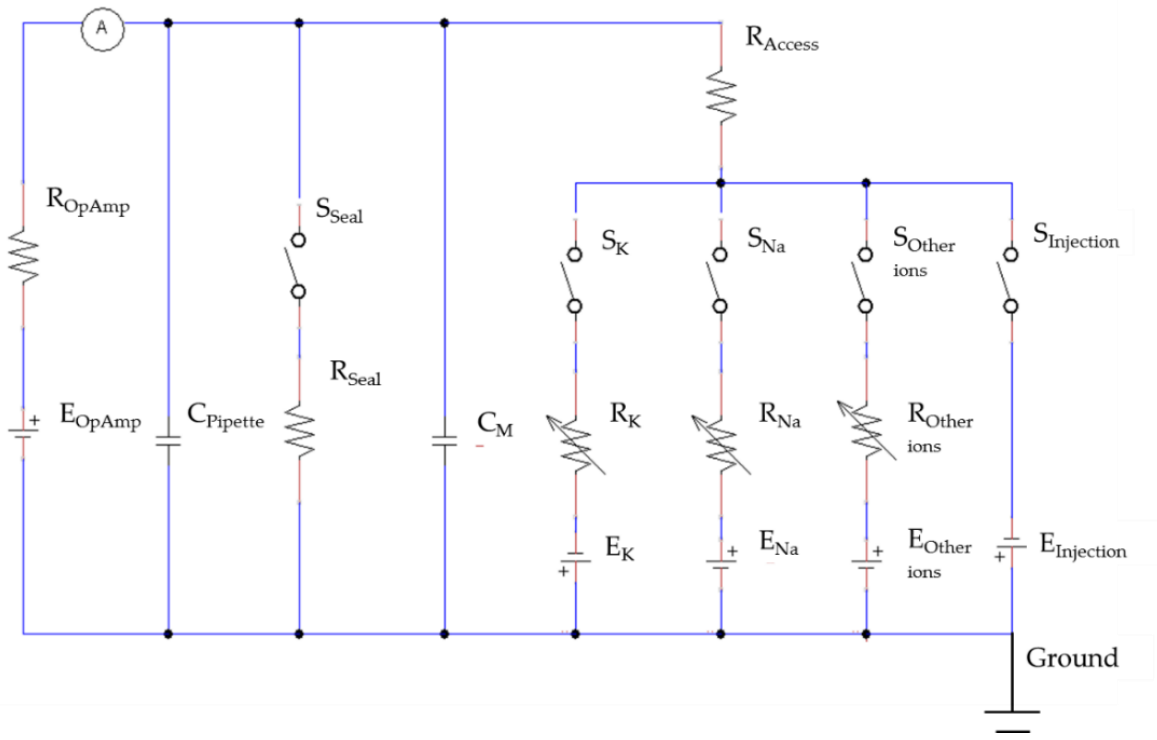

Figure 24. The equivalent circuit of the current feedback model for the cell cytoplasmic microinjection and cell viability verification.

In the measurement, the membrane current (I_M) can be recorded. According to the circuit model, I_M is composed of several components, as shown in Equation (3.5), including the current caused by the pipette capacitance ($I_{Pipette}$), the current passing through the sealing resistance (I_{Seal}), the current passing through the access resistor

(I_{Access}), and the current caused by the membrane capacitance (I_c). I_c is produced by the charge accumulation at the outer and inner membrane surface when V_m changes.

$$\boldsymbol{I_m = I_{pipette} + I_{Seal} + I_C + I_{Access}} \quad (3.5)$$

To simplify Equation (5), $I_{Pipette}$ can be cancelled out by adjusting the current signals with the function of leak subtraction in the operational amplifier of the patch clamp. In addition, I_{Seal} is usually small enough to be neglected when R_{Seal} is very large. I_C is nonzero only when V_m is changing [95]. Throughout the microinjection, V_m is controlled at a constant level. When studying the ion channel activities, the stimulus of a square voltage pulse is applied to the cell. Hence, I_C will be nearly zero because V_m is always constant, and V_m only changes at the brief instants when the voltage is stepped to a new value. In other words, $\boldsymbol{I_C = C_m \frac{dV}{dt} \cong 0}$ under the stimulus of a square voltage pulse. I_{Access} is composed of the current passing through the sodium, potassium, and other ion channels (I_{Na}, I_K and $I_{Other\ ions}$) [97], as well as the current drop due to the injection ($I_{Injection}$) in Equation (3.6).

$$\boldsymbol{I_{Access} = I_{Na} + I_K + I_{Other\ ions} + I_{Injection}} \quad (3.6)$$

By combining Equations (3.5) and (3.6), the membrane current (I_M) will be directly equal to I_{Access}, as shown in Equation (3.7).

$$\boldsymbol{I_m = I_{Access} = I_{Na} + I_K + I_{Other\ ions} + I_{Injection}} \quad (3.7)$$

Therefore, the electric equivalent circuit of the cell cytoplasmic microinjection can be simplified, as shown in Figure 25.

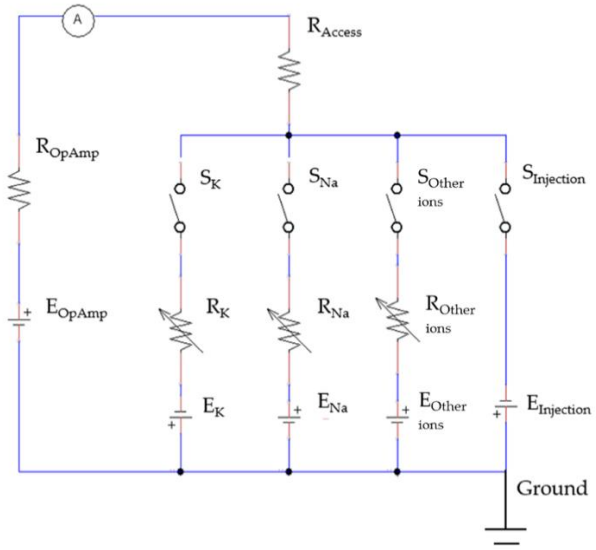

Figure 25. The simplified circuit of the current feedback model for the cell cytoplasmic microinjection and cell viability verification.

The microinjection was performed on a single living cell at the resting state. S_K, S_{Na}, and $S_{Other\ ions}$ are anticipated to be open because R_{Na}, R_K, and $R_{Other\ ions}$ are expected to be very large since nearly none of the ion channels will be activated without the voltage stimulus. Hence, I_{Na}, I_K, and $I_{Other\ ions}$ will become zero. Subsequently, I_M will only be equal to the current drop, as R_{Access} is connected to $E_{Injection}$, induced by the concentration difference of the ions in the cytoplasm of the living cell due to the microinjection of the intracellular solution, as shown in Equation (3.8).

$$\boldsymbol{I_m = I_{Injection} = \frac{E_{Injection}}{R_{Access}}} \tag{3.8}$$

3.2. The electric model for cell viability

After the injection to a living cell, its viability is of great concern and can be verified by studying ion channel activities. When the cells are alive after the microinjection, the activities of the ion channels can be activated by applying the voltage stimulus. Under the voltage stimulus, the cell membrane current I_M of the normal cell can be calculated by Equation (3.9). In this situation, R_K, R_{Na}, and $R_{Other\ ions}$ are very low, so those ions can easily pass through the cell membrane when the Na^+,

K^+, and other ion channels are activated. Moreover, $I_{Other\ ions}$ can be neglected when compared with I_{Na} and I_K because the activities of the Na^+ and K^+ ion channels are dominant. Therefore, the I_M of a normal cell is equal to the sum of I_{Na} and I_K, as shown in Equation (3.10).

$$\boldsymbol{I_m = I_{Na} + I_K + I_{Other\ ions}} \tag{3.9}$$

where $\boldsymbol{I_{Other\ ions} \cong 0}$

$$\boldsymbol{I_m = I_{Na} + I_K} \tag{3.10}$$

where the current response of I_K and I_{Na} depends on R_K and R_{Na}, respectively, as shown in Equations (3.11) and (3.12).

$$\boldsymbol{I_K = \frac{V_m - E_K}{R_K}} \tag{3.11}$$

$$\boldsymbol{I_{Na} = \frac{V_m - E_{Na}}{R_{Na}}} \tag{3.12}$$

where R_K and R_{Na} are variables based on the number of activated ion channels for passing Na^+ and K^+ ions across the membrane.

3.3. The cell cytoplasmic microinjection with the patch clamp technique

The experimental setup consists of several units (as shown in Figure 26), which are an extracellular solution to bathe the cells for providing them with an in vitro environment like in vivo, an intracellular solution to act as an electrolyte connected to a low-noise amplifier and to be injected inside the cell during the microinjection process, a low-noise amplifier (Model: Axopatch 200B from Molecular Device, Sunnyvale, CA, USA) to amplify the recording current signal from the cell, a data digitizer (Digidata 1440A from Molecular Devices) and computer for generating the voltage stimulus waveform and data acquisition of the current signal from the cell membrane, and the inverted microscope (Model: Eclipse Ti from Nikon, Tokyo, Japan) to monitor the cell cytoplasmic microinjection. The adherent cells grown on coverslips

were prepared. In each experiment, the coverslip with adherent cells was placed inside a petri dish, filled with extracellular solution. When implementing the microinjection, the force applied on the cell via the micropipette was vertical, which would not lead to the sliding of the coverslip and movement of the cell. In addition, a Faraday cage is used to reduce the background signal in the surrounding area since the patch clamp recording is very sensitive to background noise.

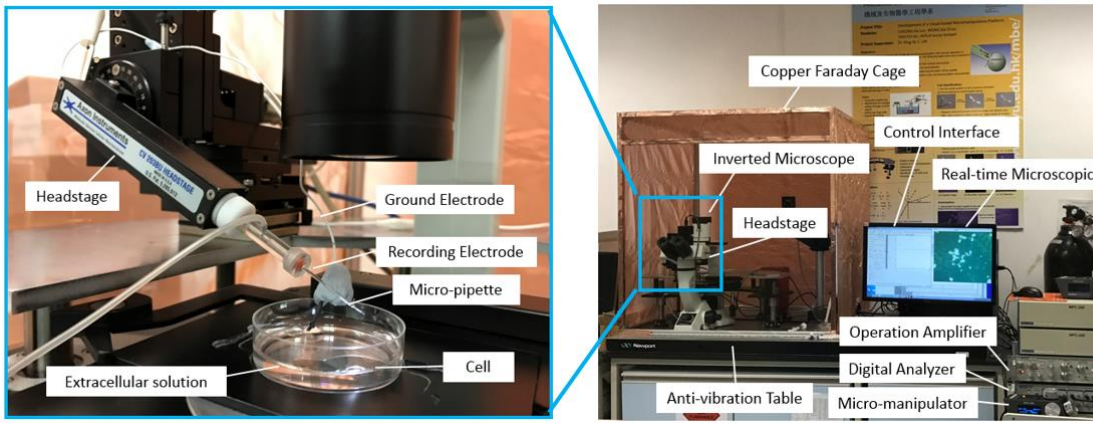

(**a**) (**b**)

*Figure 26. The experimental setup of the current feedback injection: (**a**) the close-up view; (**b**) the overall view.*

3.3.1 The patch clamp technique

The principle of the patch clamp technique is to isolate a patch of membrane electrically from the external solution and to record the current flowing into the patch. During each recording, a fire-polished glass pipette filled with a suitable electrolyte solution was pressed against the surface of a cell whilst applying light suction to create a seal whose electrical resistance is more than 1 GΩ, called the gigaseal formation [98]. The patch clamp technique can be carried out under different kinds of configurations, which can record the total current of ion channels on the cell membrane of the intact cell at the whole-cell mode [99]. The patch clamp allows an investigation of the change of the cell state from resting potential to action potential and the functional properties of ion channels. The action potential is a transient, regenerative electrical impulse in which the membrane potential (V_m) rapidly rises to a positive voltage value from a negative voltage value, namely the resting potential where the cell is at its resting state

[100]. Under a voltage stimulus, the ion channels of the living cell normally respond to generate an electric impulse. The method is believed to be a more precise and accurate way to determine the cell condition.

3.3.2 The cell cytoplasmic microinjection process

In this process, the cell cytoplasmic microinjection process is divided into five main steps. Firstly, a micropipette is made from borosilicate glass capillaries (BF120-69-7.5 from Sutter Instrument, Novato, CA, USA). Each glass capillary was pulled by a CO_2 laser-based micro-pipette puller (Model: P-2000 from Sutter Instrument). As a result, the glass capillaries are divided into two halves, which were the micropipettes with the tip size of 1 µm. From the literature, the common tip size ranges from 0.05 µm to 1 µm [43][51][53][96]. Secondly, SHSY-5Y cells are weekly prepared by cell passage and cell culture. Thirdly, the extracellular and intracellular solutions are prepared with various ions. The details of the cell culture and the solution preparation will be shown in the coming sections. Fourthly, the injection process is initiated by positioning the micro-pipette filled with intracellular solution to approach the cell surface using the micro-manipulator. The electrode placed inside the micropipette is connected to the headstage and hence to the operational amplifier. A test square voltage pulse of 20 mV for 10 ms is applied to the cell from the operational amplifier.

When the pipette is immersed into the solution, a typical positive pressure is applied using a 10 mL syringe. A displacing plunger of about 1 mL is used to remove any contaminations at the tip. The resistance value is around 4–8 MΩ at the bath position. Afterwards, the pipette tip slowly approached the cell surface until there was an obvious increase of 3 to 5 MΩ in the total resistance and a significant decrease in the test pulse amplitude. When the current signal became steady, the positive pressure could be released rapidly. By applying suction through retracting air using a 5 mL syringe, the plunger is retracted at 0.1 mL/s for a second. Consequently, a very tight seal between the pipette and cell surface can be created with a GΩ formation where the total resistance of the electrical model will be around 1 GΩ. Afterwards, the voltage potential of the cell membrane is controlled at −70 mV, and a stronger pressure was applied to the micropipette through retracting air using a 5 mL syringe. The plunger

was retracted at 1 mL/s until a significant change of the current response was observed with the existence of capacitive current trace from the cell membrane. In the circuit, the membrane current is measured spontaneously and continuously while the voltage potential is kept at −70 mV throughout the microinjection process. Before starting the microinjection experiment, the baseline of the electric current response is always adjusted to zero. Consequently, the current due to the microinjection can be acquired without distortion from the original ion activities.

During the microinjection, the current signal of the cell membrane is monitored. The permanent drop of the current level is consistently observed right after each injection. In each injection, the injection volume was estimated to be 19 pL. The estimation is based on recording the volume of the cell cytoplasm before and after the injection using optical images. In another study, the injection volume for cells (25 μm) is measured in the range of 2 to 22 pL [43]. Moreover, the patch clamp technique is used to compare the cell condition before and after the injection, and it can be done by applying a series of voltage square pulses from the operational amplifier.

3.3.3 SHSY-5Y cells and HEK-293 cells

In this study, a SHSY-5Y cell, which is the human-derived neuroblastoma cell, and a HEK-293 cell, a human embryonic kidney cell, are used to study the performance of the microinjection. The SHSY-5Y cell is often used as in vitro model to study Parkinson's disease through studying the ion channel activities. The HEK-293 cell is widely used in cell biology, including in the study of gene therapy, and is also used as one mammalian expression system in the study of voltage-gated K^+ channels [101][102]. The cells are cultured in standard conditions (Dulbecco's Modified Eagle's Medium supplemented with 10% fetal bovine serum and 1% penicillin-streptomycin). The cells are weekly passaged via detachment with trypsin-EDTA, 5-min centrifugation at 1900 rpm, resuspension of the pellet in a 25 mL flask filled with 3 mL of medium and seeding of a new flask with 100–200 μL of suspension.

3.3.4 Intracellular and extracellular solution

During the micro-injection, the cell lines cultured on a coverslip are bathed in an extracellular solution containing 160 mM NaCl, 4.5 mM KCl, 1 mM MgCl2, 2 mM CaCl2, 5 mM glucose, and 10 mM of HEPES with pH adjustment to pH 7.4 using NaOH. The intracellular solution is prepared using 75 mM KCl, 10 mM NaCl, 70 mM KF, 2 mM $MgCl_2$, 10 mM HEPES, and 10 mM EGTA with pH adjustment to pH 7.2–7.4 using KOH.

3.4. Current drop of the cell cytoplasmic microinjection

In the experiment, both SHSY-5Y and HEK-293 cells were used for the microinjection. The cells were placed at the stage of the inverted microscope, and optical images were obtained during the injection process, as shown in Figure 27. In each injection, a single cell was selected, and a tight seal was formed between the micropipette and the cell surface. After that, the current response of the cell was recorded and re-adjusted the initial current to be zero. During the microinjection, the cell is injected with around 19 pL intracellular solution, and the current responses have been recorded for the microinjection of both SHSY-5Y cells and HEK-293 cells, as shown in Figure 28. Since the estimated injected volume is 19 µL, the new concentration of $[K^+]$ and $[Na^+]$ are calculated to 150.5 µM and 15.1 µM, respectively, and the $E_{injection}$ is estimated at −0.3 mV, which is not sufficient to activate the ion pumps (<10 mV) after the injection. As a result, $E_{Injection}$ would contribute a current drop during the injection. In one test, we found that the current drops are −11.9 nA and −11.7 nA for the SHSY-5Y cells and HEK-293 cells, respectively.

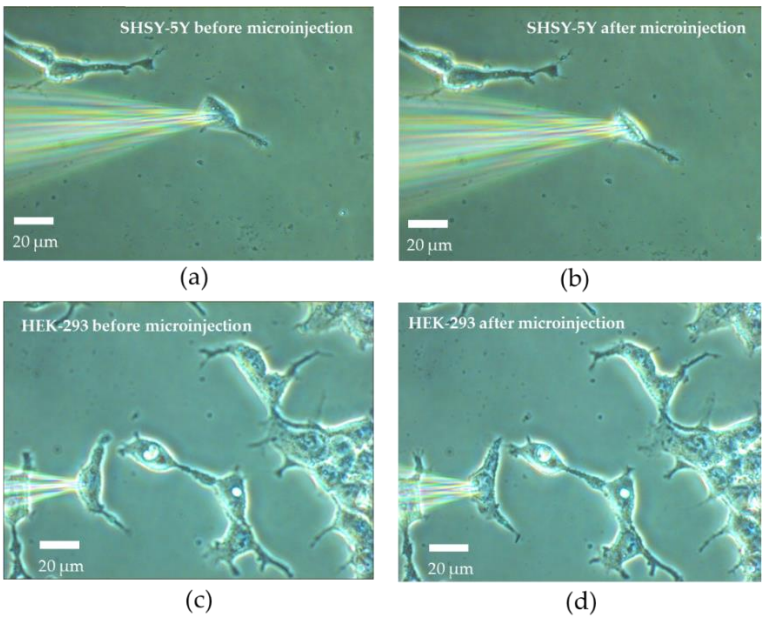

*Figure 27. Photos of the micropipette and the cells (**a**) SHSY-5Y cells before the microinjection; (**b**) SHSY-5Y cells after the microinjection; (**c**) HEK-293 cells before the microinjection; (**d**) HEK-293 cells after the microinjection.*

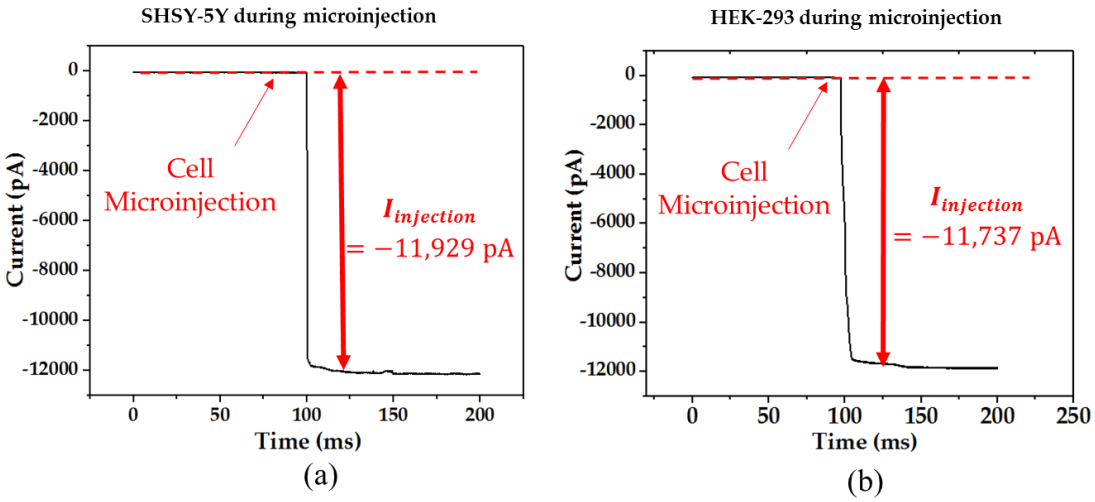

*Figure 28. The current response during the cell cytoplasmic microinjection of (**a**) a SHSY-5Y cell and (**b**) a HEK-293 cell.*

3.5. The current response of ion channel activities

Before and after the microinjection, electrical responses of SHSY-5Y cells and HEK-293 cells are recorded, as shown in Figure 29. The responses of both cells are observed under the voltage stimulus of a square pulse from −80 mV to 100 mV with

the epoch of 60 ms. The current responses can be studied through the direction and the amplitude of the current trace.

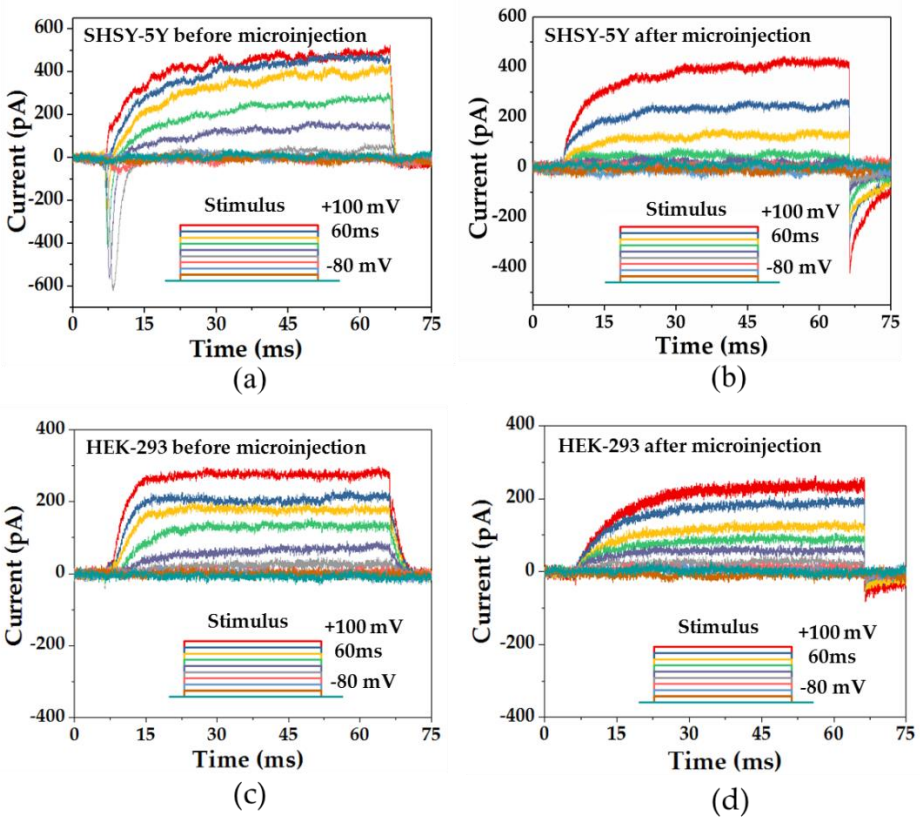

*Figure 29. The current traces of ion channels and the voltage stimulus of a SHSY-5Y cell: (**a**) before the microinjection and (**b**) after the microinjection. The current traces of ion channels and the voltage stimulus of a HEK-293 cell: (**c**) before the microinjection and (**d**) after the microinjection.*

Before the microinjection, the observation of the normal ion channel activities of both Na^+ and K^+ ion channels in SHSY-5Y cells were known with the inward current due to the hyperpolarization of Na^+ ion channels and the outward current due to the depolarization of K^+ channels that occurred at the same time, which was also reported by another research group [100]. Meanwhile, the normal ion channel activities of K^+ ion channels were recorded in HEK-293 before the microinjection.

After the microinjection, the viability can be verified by the current response due to the ion channel activities evolved by the voltage stimulus of a square pulse from −80 mV to 100 mV with the epoch of 60 ms, applied from the low noise amplifier. The ion channel activities of the K^+ ion channel were found to be normal with the outward current due to the depolarization of K^+ channels [100]. The current responses were compared before and after the microinjection of SHSY-5Y cells and HEK-293 cells. In

SHSY-5Y cells, K^+ ion channels can be activated in both circumstances, while Na^+ ion channels can only be activated before the microinjection. Due to the microinjection, Na^+ ions were redistributed across the cell membrane, while Na^+ ions inside the cell membrane were consumed, and hence Na^+ ion channels could not be activated after the microinjection. However, the disappearance of Na^+ ions did not lead to the death of the cell, which can be proven by the sustainable activities of the K^+ ion channels. It is believed that we can re-activate the Na^+ ion channels if we inject more Na^+ into the cell. In HEK-293 cells, K^+ ion channels can be activated in both circumstances.

3.6. Reliability and repeatability of the current responses during the cytoplasmic microinjection

In the experiment, reliability and repeatability are two important indicators of monitoring the current responses during the cytoplasmic microinjection. The reliability can be found by the consistency of the total current drop after the injection among 10 tests for both SHSY-5Y cells and HEK-293 cells, whilst the repeatability can be demonstrated by the similar results of two different cells, as shown in Figure 30. From 10 tests, we found that the current response of SHSY-5Y cells and HEK-293 cells are (-11.9 ± 0.2) nA and (-11.7 ± 0.4) nA, respectively.

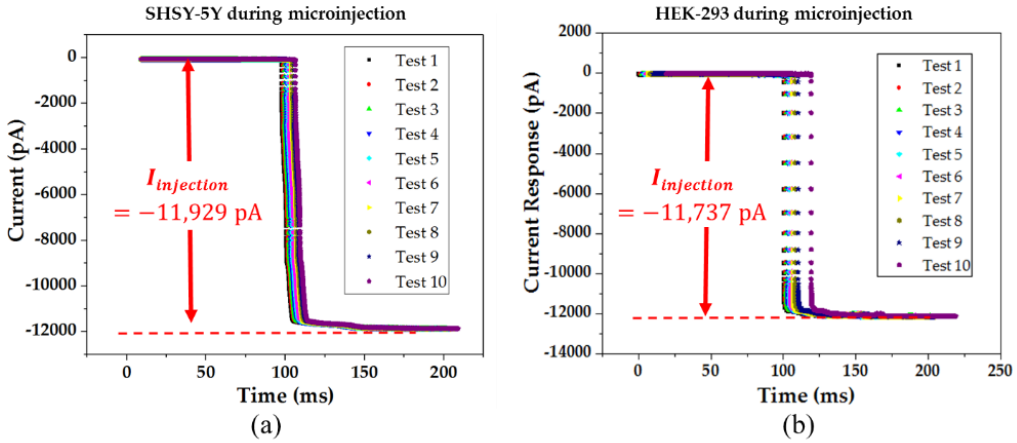

Figure 30. The current response of the cell during the cell cytoplasmic microinjection: (a) the microinjection process of the SHSY-5Y cell with 10 results; (b) the microinjection process of the HEK-293 cell with 10 results.

3.7. Chapter summary

An electric model for cytoplasmic microinjection with current feedback was designed especially for small adherent cells. To elucidate the model for realising the current feedback, the cytoplasmic microinjection was performed on the SHSY-5Y and HEK-293 cells. During the microinjection, the consistent current drop (~12 nA) was found on both cells across the cell membrane with a prompt response within several milliseconds for the SHSY-5Y cell and the HEK-293 cell, while the voltage potential of the cell membrane was maintained at −70 mV. We found that the derived equation from the developed electric model can calculated the value of induced current, that matches with the experimental result of the consistent current drop of around 12nA when the injection volume is fixed at 12pL. The calculation method will be further discussed in next chapter.

The viability of cells after the cytoplasmic microinjection can be well proven by the sustainable activities of K^+ ion channels. In the future, the intracellular solution could act as a transporter of various drugs or other target materials for the micro-injection of small adherent cells using this technique.

Chapter 4 Equivalent electric circuit for monitoring the real-time response against the injection volume for cell cytoplasmic microinjection

4.1. Cell microinjection for small and non-spherical living cells

In the experiment, living adherent cells grown on the coverslip s bathed with the extracellular solution inside a petri dish, as shown in Figure 32. Each borosilicate glass capillary (BF120-69-7.5 from Sutter Instrument) is pulled by a CO_2 laser-based micropipette puller (Model: P-2000 from Sutter Instrument) to make a micropipette. A glass micropipette with a very fine tip (tip size is 1 μm) filled with an intracellular solution is inserted into the cell. During cell microinjection, the solution is injected through the micropipette with a recoding electrode inside it. Meanwhile, another electrode, namely the reference/ground electrode, is immersed inside the intracellular solution to measure the electrical current passing across the cell membranes of a single cell. The recording electrode was connected to a low noise amplifier (Model: Axopatch 200B from Molecular Device, Sunnyvale, CA, USA) and a digitizer (Model: Digidata 1440A from Molecular Devices), thereby acquiring the electrical current signal at nano-ampere scale rapidly. The movement of the micropipette was controlled by a micro-manipulator (Model: MPC-200 from Sutter Instrument Company) in three directions at the micrometre scale. A typical observation of a cell and a micropipette is shown in Figure 31. The injection is implemented with a syringe while the injection volume is controlled by a syringe pump (Model: NE 1000 from Pump Systems Inc.). A syringe is used to give the pressure to push the fluid from the micropipette into the cell. In each injection, the injection volume was estimated to be 4 pL, 8 pL, 12 pL and 15 pL, respectively. The estimation is based on finding the volume of the cell cytoplasm before

and after the injection using microscopic images. Furthermore, a Faraday cage was installed whereby the background signal in the surrounding can be filtered.

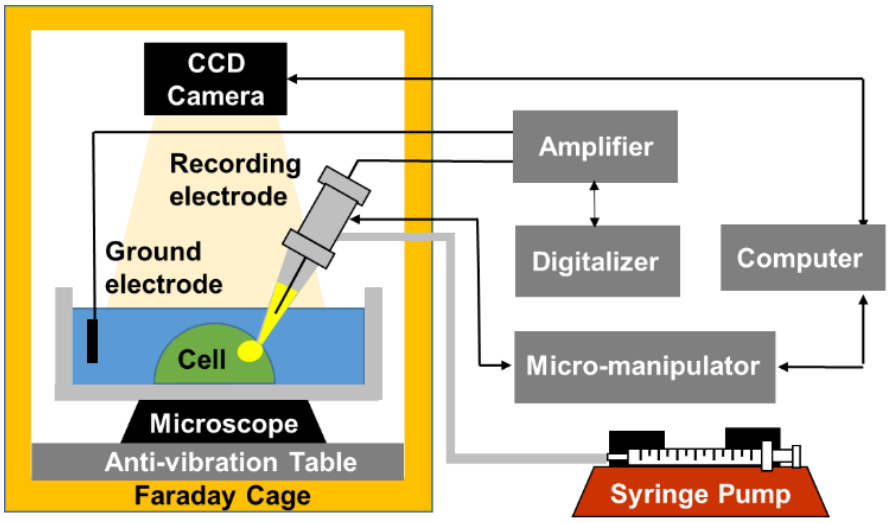

Figure 31. Schematics of cell microinjection at nano-ampere scale.

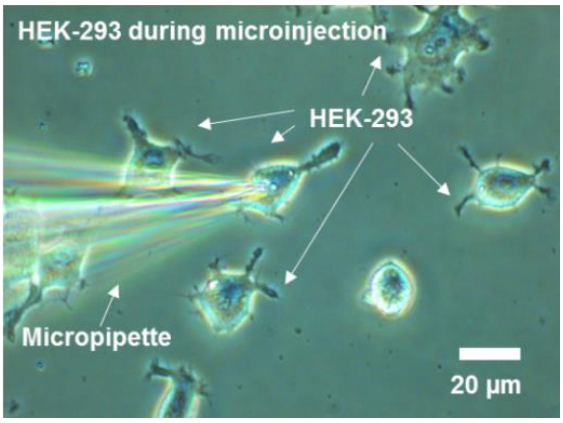

Figure 32. The microscopic image of a cell and a micropipette during cell microinjection.

4.2. Current drops of cell microinjection with different injection volumes

In this experiment, the cell microinjection has been implemented on HEK-293 cells with different injection volumes in the range of 4 pL to 15 pL. When the solution was injected into the cell with different volumes, the electrical current response was detected within the period of several milliseconds, as shown in Figure 33. Before each

microinjection, the baseline of electric current response was always adjusted to zero. Therefore, the current due to microinjection can be recorded without distortion from the original ion activities. Since the detected signal is very small at nano-ampere, it is very easy to be distorted by the surrounding noise, especially when the injection volume is getting smaller down to be 8 pL or below. Thus, we can observe some small spikes in these cases. The current responses with different injection volumes were plotted in Figure *34*, with 24 tests in total. Each point in Figure *34* respresents one test. We found that the electrical signal is directly proportional to the injection volumes.

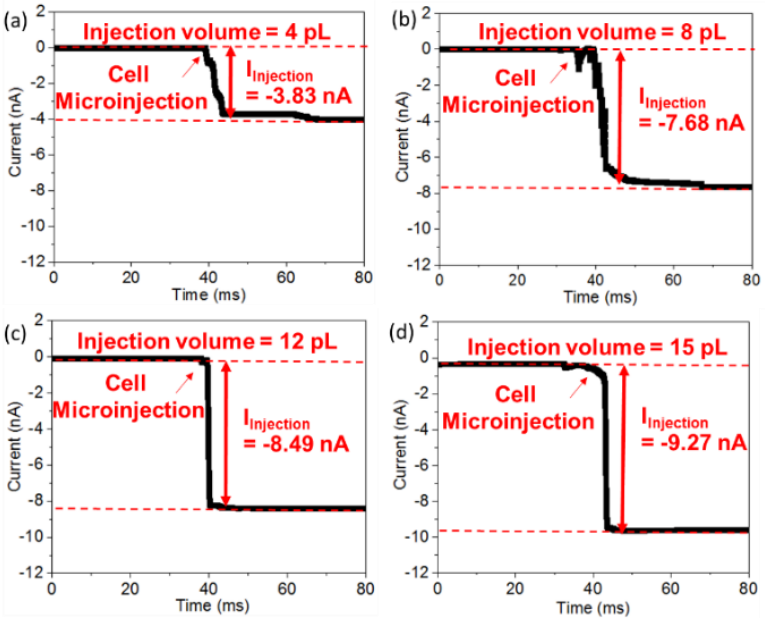

Figure 33. The current responses during the cell microinjection when the injection volumes are (a) 4 pL, (b) 8 pL, (c) 12 pL and (d) 15 pL, respectively

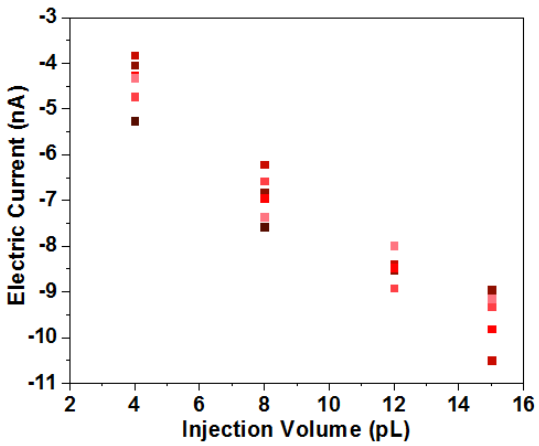

Figure 34. The current responses against the injection volumes during the cell microinjection.

4.3. Verification of the current drops using the equivalent electric model

To verify the observation with our hypothesis, we designed an equivalent electric model to explain why the electric response can be measured during the microinjection. In Figure 35, the equivalent electrical model consists of an operational amplifier that acts as a voltage source, $\boldsymbol{E_{OpAmp}}$, in series with a resistor $\boldsymbol{R_{OpAmp}}$. In the meantime, there are four switches in the circuit, including the switch ($\boldsymbol{S_{seal}}$) for the sealing resistance, the switches ($\boldsymbol{S_K}$) and ($\boldsymbol{S_{Na}}$) for activation of K^+ ion channels and Na^+ ion channels, respectively as well as the switch ($\boldsymbol{S_{injection}}$) for the microinjection of the cell.

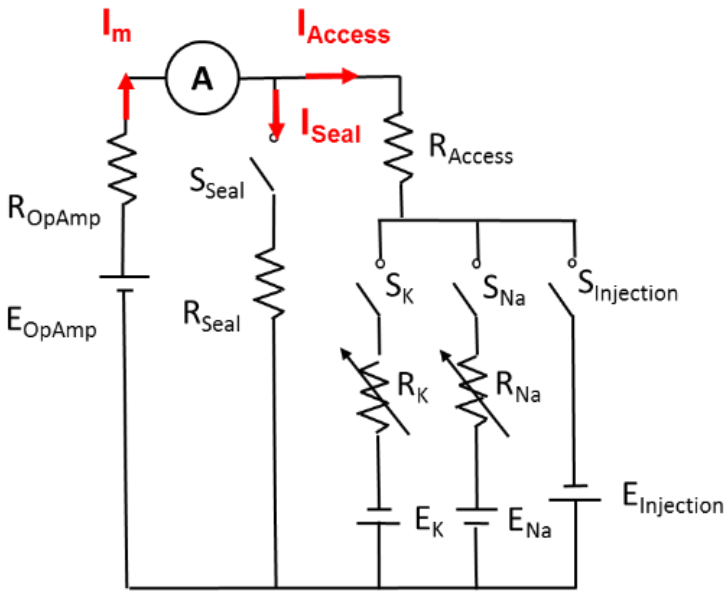

Figure 35. The equivalent circuit of the cell microinjection

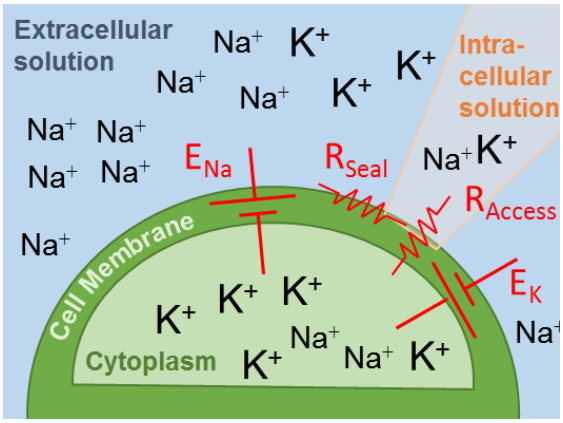

Figure 36. The illustration of E_K, E_{Na}, R_{Seal} and R_{Access} on the cell membrane.

During the microinjection, the recording electrode bathed inside the glass micropipette can form a sealing with the cell membrane and hence measure the total current flow across the cell membrane ($\boldsymbol{I_m}$).

$$\boldsymbol{I_m = I_{Seal} + I_{Access}} \quad (4.1)$$

where I_m is the total current flow across the cell membrane, I_{Seal} is the current flow depending on the sealing condition between the cell membrane and the glass micropipette. In the model, I_{Seal} is smaller when R_{seal} is large since a secure suction between the glass micropipette and the cell membrane is formed. In addition, I_{Access} is the current change due to ion concentration change during microinjection ($\boldsymbol{I_{Access} = E_{Injection}/R_{Access}}$). When the intracellular solution is injected into the cytoplasm, the cytoplasmic concentration of K^+ ion and Na^+ ion will change and hence induce $E_{Injection}$.

During the microinjection, $\boldsymbol{R_{seal}}$ will decrease due to the change of contact condition between the cell membrane and the glass micropipette. The cell membrane will expand, and hence $\boldsymbol{I_{Seal}}$ will increase. To estimate $\boldsymbol{I_{Seal}}$, the command voltage from an amplifier ($\boldsymbol{E_{OpAmp}}$) was set as -10 mV throughout the process. During the microinjection, we recorded $\boldsymbol{R_{seal}}$. Consequently, the calculated values of $\boldsymbol{I_{Seal}}$ with different injection volumes were calculated and summarized in Table 1 using Equation (4.2).

$$\boldsymbol{I_{Seal} = \frac{E_{OpAmp}}{R_{Seal}}} \quad (4.2)$$

Table 1. The recorded R_{Seal} and the calculated I_{Seal} of different injection volume

Injection Volume (pL)	**4**	**8**	**12**	**15**
$\boldsymbol{R_{Seal}}$ (MΩ)	1.2	1.4	1.6	1.8
$\boldsymbol{I_{Seal}}$ (nA)	- 5.55	-6.25	-7.14	-8.33

4.4. Potential Change of Potassium Ion and Sodium Ion after the Cell Microinjection

On the other hand, the cell membrane has the electric potential due to the difference of ion concentration across the cell membrane, as illustrated in Figure 36. Living biological cells are constructed with cytoplasm and bathed in extracellular fluid, which ion concentration in both cytoplasm and extracellular solution for different cells varies in different locations due to their unique functions. The electric potential (can be calculated based on Nernst Equation [64]. Since the ion concentration of potassium ion and sodium ion are significantly larger than other ions, therefore, we will consider potassium ion and sodium ion only in our calculation in Equation (4.3). Hence, the cell membrane potential ($\boldsymbol{E_{cell\ memb}}$) is the sum of all electric potentials induced by the ions.

$$\boldsymbol{E_{cell\ memb}} = \frac{\boldsymbol{RT}}{(\mathrm{Z})\boldsymbol{F}} \boldsymbol{ln} \frac{[\boldsymbol{Na^+}]_o}{[\boldsymbol{Na^+}]_i} + \frac{\boldsymbol{RT}}{(\mathrm{Z})\boldsymbol{F}} \boldsymbol{ln} \frac{[\boldsymbol{K^+}]_o}{[\boldsymbol{K^+}]_i} \tag{4.3}$$

where $\boldsymbol{R}$ is the ideal gas constant ($\boldsymbol{R}$ = 8.314472 J K^{-1}·mol^{-1}); $\boldsymbol{T}$ is the temperature in kelvins ($\boldsymbol{T}$ =299 K in our condition); $\boldsymbol{F}$ is Faraday's constant in coulombs per mole (F = 9.648533 × 10^4 C·$mol^{-1)}$; $\boldsymbol{[ion]_o}$ is the extracellular concentration of that ion (in moles per cubic meter); $\boldsymbol{[ion]_i}$ is the intracellular concentration of that ion (in moles per cubic meter); and $\boldsymbol{Z}$ is the number of moles of electrons transferred in the cell reaction or half-reaction ($\boldsymbol{Z}$ = +1 for both sodium and potassium ions). Equation (3) can be expressed as Equation (4) as follows,

$$\boldsymbol{E_{cell\ memb}} = \boldsymbol{E_{Na}} + \boldsymbol{E_K} \tag{4}$$

where $\boldsymbol{E_{Na}}$ is the potential difference induced by the concentration difference of sodium ion between the cytoplasm and extracellular fluid, and similarly, $\boldsymbol{E_k}$ is the potential difference induced by the concentration difference of potassium ion.

Based on Equation (4.3), the membrane potential before the injection ($\boldsymbol{Old\ E_{Cell\ Memb}}$) is estimated as -85.69 mV because the concentrations of potassium ion and sodium ion are 400 mM and 50 mM in the cytoplasm, and 4.5 mM and 160 mM in extracellular

fluid in nature. Similarly, the membrane potential after the injection (***New*** $E_{Cell\ Memb}$) can be calculated according to the new concentration of potassium ion and sodium ion inside the cytoplasm of cells after the microinjection, as shown in Table 2. As a result, the change in the membrane potential due to the injection ($E_{injection}$) can be found by Equation (4.5), where ***Old*** $E_{Cell\ Memb}$ is nearly the same in four conditions because the same type of cell with a similar volume of around 141 pL was tested even the injection volume is different.

$$E_{Injection} = New\ E_{cell\ memb} - Old\ E_{cell\ memb} \tag{4.5}$$

$$I_{Access} = \frac{E_{Injection}}{R_{Access}} \tag{4.6}$$

Table 2. The potential change of potassium ion and sodium ion after the cell microinjection

Injection Volume (pL)	**4**	**8**	**12**	**15**
New $[Na^+]_i$ (mM)	48.97	47.99	47.07	46.18
New $[K^+]_i$ (mM)	391.90	384.21	376.90	369.93
New E_{Na} (mV)	-115.15	-114.64	-114.14	-113.66
New E_k (mV)	30.52	31.04	31.54	32.03
New $E_{Cell\ Memb}$ (mV)	-84.63	-83.60	-82.60	-81.63
$E_{Injection}$ (mV)	1.06	2.10	3.09	4.06
R_{Access} (MΩ)	6.6	6.9	7.1	7.4
I_{Access} (nA)	0.14	0.30	0.45	0.62

Comparing the estimated current due to injected ions and the estimated current due to the change of the contact condition with the measured current potential, we can obtain the graph as shown in Figure 37.

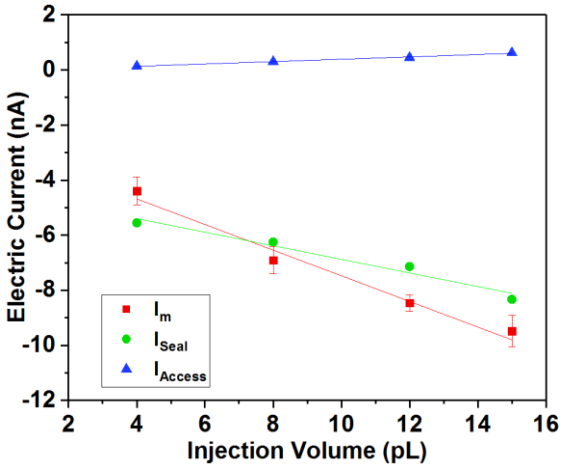

Figure 37. The linear fit of the measured current and estimated current against the injection volume.

From the calculation, the change of the current drop due to the ion concentration change across the cell membrane during the injection (I_{Access}) is very small. Whilst the estimated current (I_{Seal}) due to expansion of cell membrane increase significantly.

We observe that the estimation of I_{Seal} is closer to the experimental results of the total membrane current (I_m), which is consistently proportional to the injection volume.

4.5. Chapter Summary

In the experiment, the amount of electrical current responses can be detected within several milliseconds per injection, and it was found to be a directly proportional relationship with the injected volumes of the solution into the cell at a pico-litre scale. The current drops are 4.40 ± 0.51 nA, 6.91 ± 0.50 nA, 8.46 ± 0.30 nA and 9.49 ± 0.57 nA when the injection volumes are 4 pL, 8 pL, 12 pL and 15 pL, respectively. A linear relationship between the current due to expansion of cell membrane during microinjection has been found. We can conclude that the current change can be a reliable and fast response for monitoring the process of microinjection.

Chapter 5 Deep learning approach for cell detection and screening in patch clamp for electrophysiology

To enhance the success rate and the efficiency of the patch clamp technique, APC with object detection of a unique and specific biological cell is highly desired with high accuracy and high throughput. However, the complexity and diversity in microscopic image data pose challenges for developing the intelligence image analysis and hence the high-throughput cell screening method [103][104]. Even though the computer vision analysis for bioimages can be the solution in the past for various applications, such as object detection, motion analysis or measurement of morphometric features [105][106][107], those software are not easy to reprogram, and the parameter tuning for specific biological assays is required. Consequently, manual software adaptions would be one of the major obstacles for most cell biological laboratories due to the limited knowledge about the mathematics behind the image analysis algorithms and a lack of expertise in software engineering [103]. Thus, machine learning superior to conventional computer vision methods can come to solve the complex dimensional data analysis tasks, because machine learning aims to provide a simple solution with learning processing rules from the own data rather than relying on manual adjustment of parameters or pre-defined processing steps [104][108].

In the past, building a pattern-recognition or machine-learning system often required considerable domain expertise to design a feature extractor that can transform the raw data into a suitable internal representation or feature vector from which the recognition subsystem, often a classifier, could detect or classify patterns in the input; meanwhile, representation learning is a set of methods that allow a machine to be fed with raw data and to automatically discover the representations needed for detection or classification [78].

Deep-learning methods are representation-learning methods with multiple levels of representation, obtained by composing simple but non-linear modules, each of which transforms the representation at one level starting with the raw input into a representation at a higher, slightly more abstract level [78]. In recent years, several deep

neural networks have been developed for object detection. A deep CNN is typically composed of several layers of convolution neural networks for feature extraction in order to identify the object piece-by-piece and pooling layers for downsizing input data to reduce memory usage, as shown in Figure 38 [109][110].

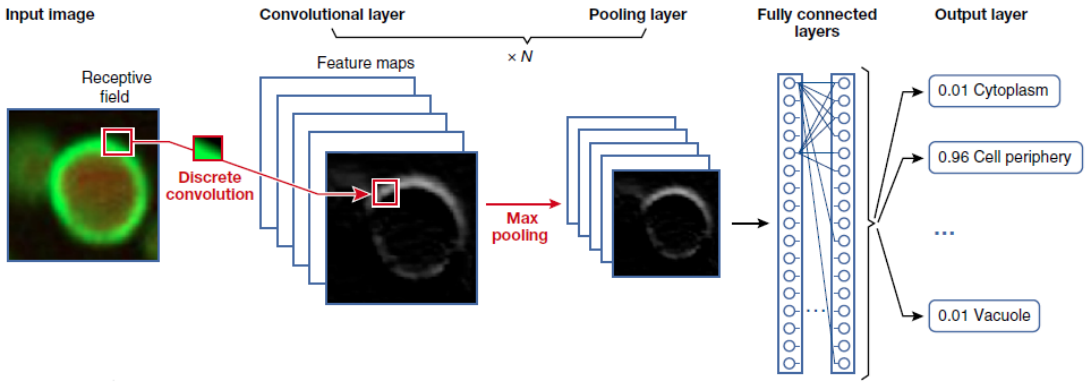

Figure 38. Convolution neural networks (CNN) for cell detection [115].

Recent advances in this field are driven by the success of region proposal methods and region-based convolutional neural networks (e.g. R-CNNs) [111][112]. You only look once (YOLO) serial networks are typical models of the one-stage detection pipeline with the ability of precise object detection in real-time, and they are widely applied on natural scene detection, face detection and so forth [88]. Compared with two-stage networks, like Faster R-CNN, YOLO possesses the advantage of faster detection speed which benefits from no demand on building an additional network to generate proposal regions [86]. With the evolution of YOLO serials, the detection performance of the newest version is always better than that of the previous two versions [89]. Though YOLOV4 is the latest YOLO serial model and outperforms the three previous versions in precision, its complexity is the highest among the four models [91]. Therefore, considering the balance between model complexity and model performance, we have developed a modified model named CELL-YOLO on the basis of YOLOV3 for the detection of the unique biological cell in good condition at the current patch clamping setup in this study. In order to improve the ability of feature extraction of the object-detection-oriented backbone, dilated bottlenecks used in DetNet [113] are integrated into the backbone of CELL-YOLO. The effectiveness of our proposed model is thoroughly validated by experiments, and the performance is compared with that of YOLOV3 and YOLOV4.

This research project is internal collaborative research. The CELL-YOLO model was designed and built by Mr Zhe Liu under the supervision of Prof. King Lai. The images were collected and labelled by Miss Yee Ching Wong and Miss Yee Lam Liu. Prof. King Lai suggested classifying the cell in three conditions and I have designed the criteria of three cell conditions. In this research, I have verified the model and re-constructed the database of the biological cells; I have trained the developed model of CELL-YOLO, YOLOV3 and YOLOV4 using the same set of databases for comparison and have measured the performance of the trained model in terms of mAP (mean average precision) and FPS (frames per second) for measuring the accuracy and the processing speed.

5.1 CELL-YOLO for biological cell detection

In this work, a modified model called CELL-YOLO is developed using YOLOV3 as a baseline for a specific task of selecting a suitable cell in good condition automatically for patch clamp and hence increasing the success rate and efficiency of this operation. CELL-YOLO detection pipeline includes data collection, model training and model testing, as shown in Figure 39.

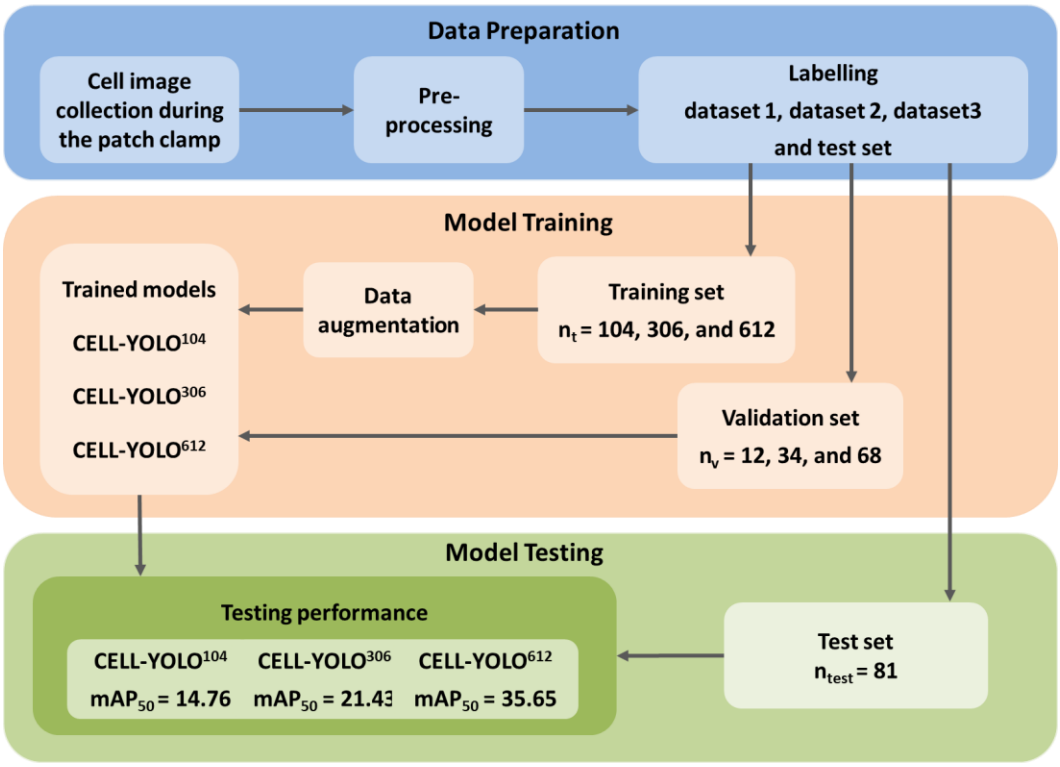

Figure 39. Flow diagram of the development of CELL-YOLO of biological cell detection for automated patch clamp where n_t, n_v and ntest mean the number of images for training, validation, and testing, respectively.

In this study, the biological cells are cultured with Dulbecco's Modified Eagle Medium (DMEM), 9% fetal bovine serum (FBS), and 1% Penicillin-Streptomycin-Neomycin (PSN). Cell images and electrophysiology are conducted and collected by a traditional patch clamp system. In preprocessing, all images are cropped to the dimension of 416 × 416 × 3 for labelling processes and ground truth labels are produced by experts for model training and testing. Eventually, three datasets are built with dataset 1, dataset 2 and dataset 3, respectively. In these datasets, 90% of images are contributed to the training set, whereas 10% of the images in the dataset are contributed to the validation set. Dataset 1, 2 and 3 consists of 104, 306 and 612 images in the training set; and 12, 34 and 68 in the validation set, respectively. During model training, image augmentation is applied on each image randomly in every batch of the training set at each epoch to enrich the dataset for training. A separate set of cell images with 81 images that is independent of Dataset 1, 2 and 3 has been allocated to the testing set for model testing. Each model was tested with the same testing set to compare the performance of trained models reasonably afterwards.

The architecture and the building blocks of the CELL-YOLO network are shown in Figure 40 and Figure 41. The input of the model is an RGB image with the dimension of 416 × 416 × 3, and the outputs of the model are set with the specific dimension based on the size of the biological cell acquired during the patch clamp experiment under a microscope in this study. The dimensions of the two output layers are 13 × 13 × (5 + the number of cell classes) and 26 × 26 × (5 + the number of cell classes), respectively, in which smaller feature maps are responsible for detecting larger cells and vice versa. The meaning of each element in the output layer is the same.

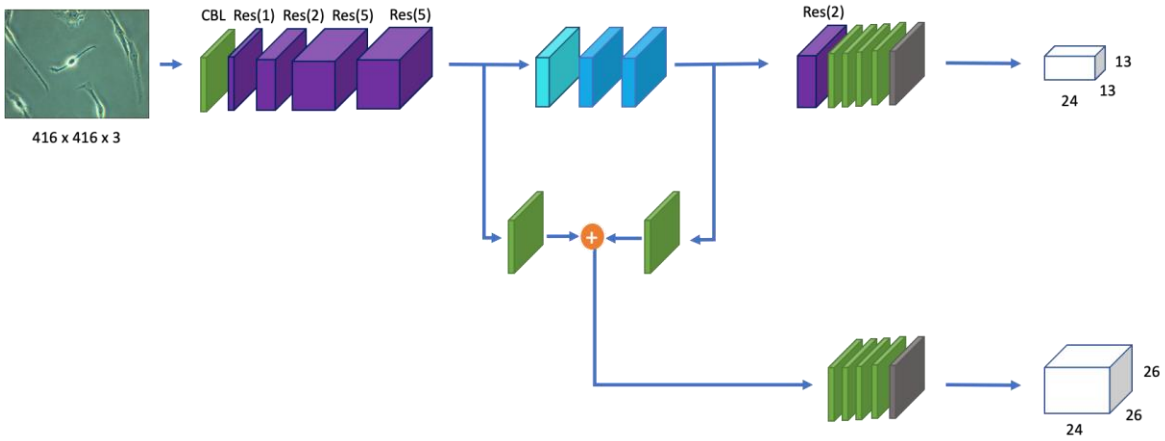

Figure 40. The architecture of CELL-YOLO.

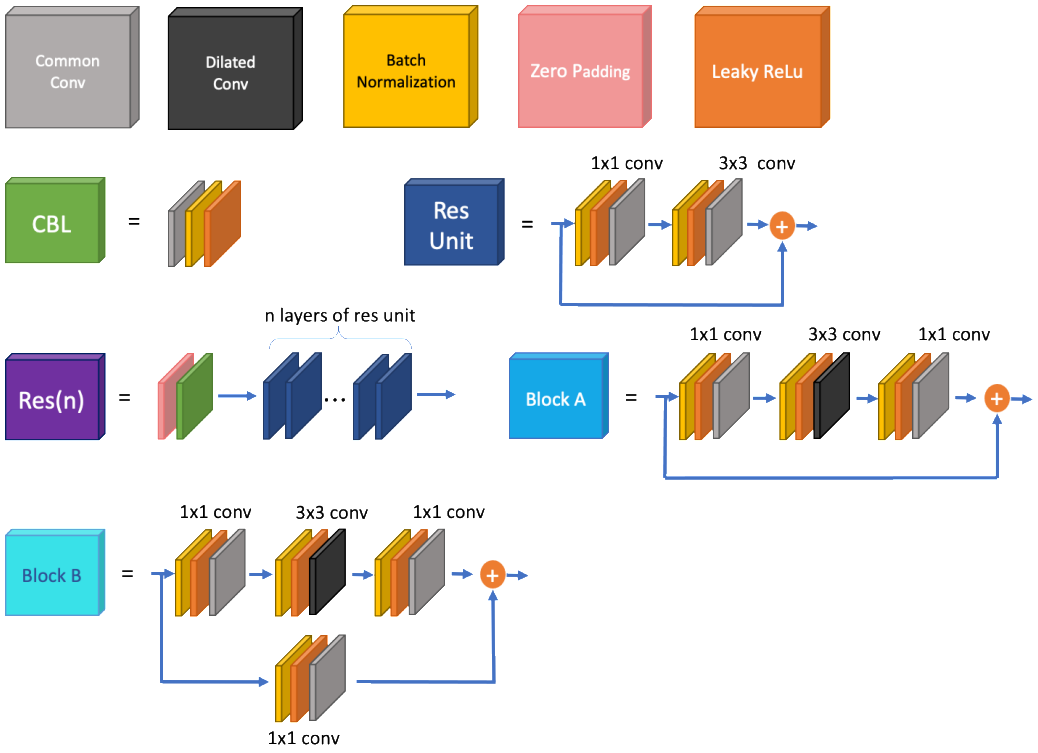

Figure 41. Building blocks of CELL-YOLO

Six anchors are determined by k-means clustering over the training set of dataset 3 as the YOLOV3 did. They are divided into two groups with equal amounts based on the selected area over the sliding window [89][90]. The algorithm of k-means clustering in CELL-YOLO is stated in Table 3. The group containing three small anchors is fixed at a large scale output layer, and another group containing three large anchors is fixed at small scale output layers.

Table 3. Algorithm of k-means in CELL-YOLO

Input	training set of Dataset 3
Output:	*k* prior boxes

Algorithm:

1. To give k clustering centers (W_i, H_i) $\in\{1, 2 \ldots, k\}$, where W_i and H_i are the width and height of anchor boxes. (As the location of anchor boxes is not fixed, there is no coordinate of (x,), only the width and height.)
2. Calculate the distance between each label box in the training set and each cluster center: d=1− $I(label\ \ box, cluster\ \ centre)$ by coinciding the centre of each label box with the cluster center.
3. After all label boxes are allocated, the cluster centers are recalculated by
   $W_i^{'} = \frac{1}{N_i}\sum w_i$ and $H_i^{'} = \frac{1}{N_i}\sum h_i$
   N_i is the number of label boxes in the i^{th} cluster.
4. Repeat steps 2 and 3 until there is no change of cluster center.

As the backbone of YOLOV3 is more suitable for image classification tasks, a backbone that can be used for object detection is greatly desired in CELL-YOLO. Therefore, network structures (i.e., Block A and Block B, as shown in Figure 41) used in DetNet [26] is integrated into the backbone of CELL-YOLO for increasing the spatial receptive field of the feature extraction network. It replaces the last residual block of the backbone network of YOLOV3. For the remaining part of the backbone, the number of residual blocks does not change, but the number of layers in each block and the number of channels at each convolutional layer are reduced compared with YOLOV3.

To tackle the imbalance of the number of different cell classes, the weighted class coefficient *w(c)* is added to the categorical loss of YOLO [23]. Ultimately,

$$\begin{aligned}
&\lambda_{coord}\sum_{i=0}^{S^2}\sum_{j=0}^{B}1_{ij}^{obj}[(x_i-\hat{x}_i)^2+(y_i-\hat{y}_i)^2] \\
&\quad+\lambda_{coord}\sum_{i=0}^{S^2}\sum_{j=0}^{B}1_{ij}^{obj}\left[\left(\sqrt{w_i}-\sqrt{\hat{w}_i}\right)^2\right. \\
&\quad\left.+\left(\sqrt{h_i}-\sqrt{\hat{h}_i}\right)^2\right]+\sum_{i=0}^{S^2}\sum_{j=0}^{B}1_{ij}^{obj}\left(C_i-\hat{C}_i\right)^2 \\
&\quad+\lambda_{noobj}\sum_{i=0}^{S^2}\sum_{j=0}^{B}1_{ij}^{noobj}\left(C_i-\hat{C}_i\right)^2 \\
&\quad+\sum_{i=0}^{S^2}1_{ij}^{obj}\sum_{c\in classes}w(c)\left(p_i(c)-\hat{p}_i(c)\right)^2
\end{aligned} \tag{5.1}$$

w(c) is calculated on the basis of the concept of median-frequency-balancing [114] and is expressed as:

$$w(c)=\frac{\text{median (freq)}}{\text{freq(c)}} \tag{5.2}$$

where *c* represents the class, *freq(c)* represents the total number of boxes of class *c* divided by the number of all boxes in images that contain class *c*, and *median(freq)* represents the median value of the frequencies.

In the loss function of CELL-YOLO as shown in Equation (5.1), the first and second terms represent localization loss of the coordinates and dimensions of the bounding box relative to an image, the third and fourth terms represent confidence loss of image with an object and no object, and the last term represents classification loss. The localization loss reflects if the model can detect an object within the bounding box, 1_{ij}^{obj} equals to one if there is an object in the jth box at ith grid cell, 1_{ij}^{noobj} equals to one if there is no object in the jth box at ith grid cell. In the last term of the classification loss, the weighted coefficient is added to the sum of errors for all the classes probabilities of 49 boxes in an image.

5.2 Data collection and labelling for training dataset

In this study, images were collected using a digital camera with a microscope during the patch clamp experiment. The cells in the images are divided into three classes, namely 'suitable', 'acceptable', and 'unsuitable'. Representative examples are shown in Figure 42. It should be noted that accumulated cells, overlapping cells, cells with totally irregular cell bodies, suspended cells, and dead cells are not labelled because they are certainly not suitable for the electrophysiological recording. Moreover, the cell is not labelled if over half of the cell body was out of the image. Therefore, only cells with recognizable cell bodies and axons are labelled.

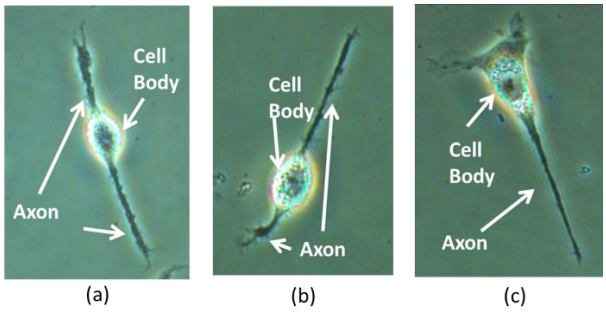

Figure 42. Examples of three classes of cells. (a) Suitable cell (b) acceptable cell (c) unsuitable cell.

A cell labelled as ‘suitable’ means that it can be patched successfully. Cells that have the ideal shape and appearance for patch clamp are labelled to this class. In this class, cells must have strong axons about or longer than the length of the cell body but not over 2 times the length of the cell body. The axons are grown from two sides of the cells and are continually attached to the surface of the coverslip. This type of axon is crucial to show that the cell is fully developed as an adherent cell and can firmly attach to the coverslip. Apart from the axon, the ideal cell should have a clear and rigid cell body that is often round and ellipse. The centre of the cell body is considered the easiest position to be patched. If the cell body is clear, the patching position can be identified, and the success rate of patching and break-in will be increased. In addition, the ideal cell should have a good health condition which can be known from the observation of a clear cell membrane. A clear cell membrane indicates the integrity of a healthy cell and shows that the whole structure of the cell would not be easily destroyed by the contact of the micropipette and the negative pressure applied during the Gigaseal process. Besides, the patch clamp recording can be affected by the distribution of the cell. In an ideal case, the target cell should be grown solely and hence the recoding signal was not influenced by the cells nearby.

A cell labelled as ‘unsuitable’ means that it cannot be patched successfully. Cells that should not be selected for Patch clamp are classified into this class. Cells with an unclear cell body and axons are categorized as "unsuitable" because they represent unhealthy and weak cells. Cells with an unclear cell membrane are also categorized to this class because the cell at this stage is nearly dead. Consequently, it is easy to damage the cell membrane even when we carefully control the tip of a micropipette to approach the cell when conducting a patch clamp experiment. This situation often happens on the patched cells and cells which have been immersed in the extracellular solution and outside of the incubator for more than an hour.

The final class is ‘acceptable’, which is the condition between “suitable” and “unsuitable”. Some cells that can be selected to perform patch clamp with uncertainty can be classified into this class. In this class, cells may not be entirely adhesive to the coverslip. One of the features is that the cell body is perfectly round while the axons

are still ideally grown. Another situation is that the length of one axon is too short, as shown in Figure 42 (b). When the cell is not attached firmly, the cell might be leaving the surface due to the negative pressure or the small movement of the micropipette. This led to the breaking of the sealing between the micropipette and the cell membrane. Ideally, the target cell is grown solely, but it is difficult to control the distribution of the cells. In many cases, the axon of the target cell is connected to the other cells. Therefore, it is acceptable to carry out the patch clamp recording with the connected cells. However, it is crucial to ensure no cell overlapping with the target cell so that the patching is only conducted on a single healthy cell. In some unusual cases, the cells grow three axons. The shape of the cell body may become triangular. If the cell body is still clear and one of the axon lengths is long, the cell can still be classified as "acceptable".

5.3 Data augmentation of biological microscopic images

Data collection depends heavily on the manual work of researchers, and it is time-consuming. A patch clamp experiment usually takes 2 hours, but less than 20 images can be collected, limiting the data available for analysis. To enhance the richness of the dataset and improve the generalization ability of the deep learning model, several data augmentations are carried out before feeding training data to the CELL-YOLO during each training epoch.

5.3.1 Random image rotation

Random image rotation was used for image augmentation in this task. The original images were rotated by 90°, 180°, 270° and mirrored subjected to equal probability. A random value r subjected to zero to one uniform distribution was generated. The rotation angle was defined into four actions according to the random value r of Equation (5.3). Figure 43. Examples of image rotation. (a) original image (b) mirrored image (c) rotated by 180° (d) rotated by °270° (e) rotated by 90°. Figure 43 below illustrates the results of the random image rotation operation.

$$r \in \begin{cases} [0.0, 0.25) \ rotated\ by\ 90^o \\ [0.25, 0.5) \ rotated\ by\ 180^o \\ [\ 0.5, 0.75) \ rotated\ by\ 270^o \\ [0.75, 1.0) \ mirrored \end{cases} \quad (5.3)$$

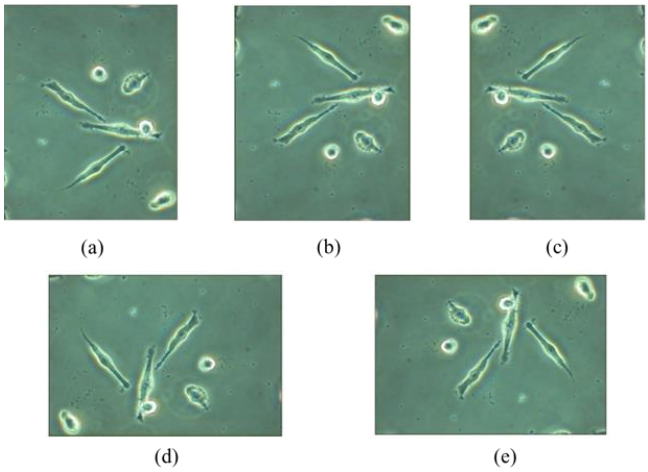

Figure 43. Examples of image rotation. (a) original image (b) mirrored image (c) rotated by 180° (d) rotated by °270° (e) rotated by 90°.

5.3.2 Random image resize

Another method of image augmentation in this study is to randomly resize the training images to adapt the input of the network on different scales. Suppose the original image size is $h \times w$, three random values denoted by r_1, r_2, r_3, subjected to from zero to one uniform distribution were generated separately. Then, two proportional parameters, p_1 and p_2, were generated by (5.4) and (5.5), a, b, c, and d were augments that need to be set according to specific tasks. In cell detection task, *a=1.3*, *b=0.7*, *c=0.25*, *d=2* was set manually. In (5.6) and (5.7), the new height (*hn*) would be equal to the integer part of $p_2 \times h$, and the new width (*wn*) would be equal to the integer part of $p_1 \times nh$.) if p_1 was less than 1. If p_1 is more than or equal to 1, the new width (*wn*) would be equal to the integer part of $p_2 \times w$, and the new height (*hn*) would be equal to the integer part of nw / p_1. This image augmentation could facilitate the network to adapt to objects with different scales. Figure 44 below shows the illustration of the results of image random resize.

$$p_1 = \frac{w}{h} \cdot \frac{r_1(b-a)+a}{r_2(b-a)+a} \quad (5.4)$$

$$p_2 = r_3(d - c) + c \quad (5.5)$$

$$New\ Height, hn = \begin{cases} p_2 \times h & if\ p_1 < 1 \\ \dfrac{nw}{p_1} & if\ p_1 \geq 1 \end{cases} \quad (5.6)$$

$$New\ Width, wn = \begin{cases} p_1 \times nh & if\ p_1 < 1 \\ p_2 \times w & if\ p_1 \geq 1 \end{cases} \quad (6.7)$$

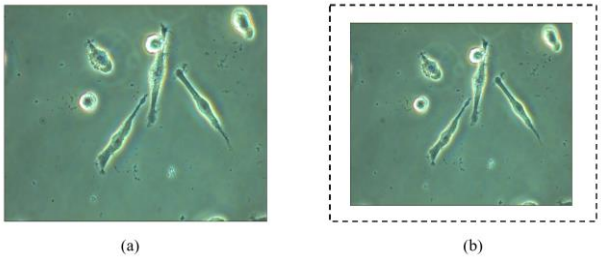

Figure 44. Examples of image random resize. (a) original image (b) resized image.

5.3.3 Colour jittering

Usually, the colour of the image is digitalized by the RGB values, which are the red, green, and blue values of every pixel in the image. In RGB colour space, the RGB values are influenced interactively even when one of the RGB values is changed. Therefore, it is difficult to control the consistency of the images after colour jittering using RGB values. Considering the manoeuvrability of individual colour values, HSV colour values consisting of hue, saturation and value is an alternative. In HSV colour space, the hue, saturation, and the values of the original image can be randomly changed separately and independently with no impact on other values. To jitter the colour of images, the colour values of every pixel in an image was first converted from RGB to HSV. Suppose the original values of hue, saturation and value denoted by hue, sat, and val were set to 0.1, 1.5 and 1.5. Then, the new values of hue, sat, and val will be generated by Equations (5.8), (5.9) and (5.10).

$$hue^* = rand\ (-hue, hue) \quad (5.8)$$

$$sat^* = \begin{cases} rand(1, sat) & if\ r < 0.5 \\ \dfrac{1}{rand(1, sat)} & if\ r \geq 0.5 \end{cases} \quad (5.9)$$

$$val^* = \begin{cases} rand(1, val) & if\ r < 0.5 \\ \dfrac{1}{rand(1, val)} & if\ r \geq 0.5 \end{cases} \quad (5.10)$$

where r is a random number subjected to from zero to one uniform distribution. $rand(m, n)$ is a random number generator that can generate a number subjected to uniform distribution from m to n. After colour jittering, the colour values of every pixel in an image will be converted from HSV to RGB, and hence new images were generated after randomizing the HSV values of images. The results of different tuning of HSV colour jittering are shown in Figure 45.

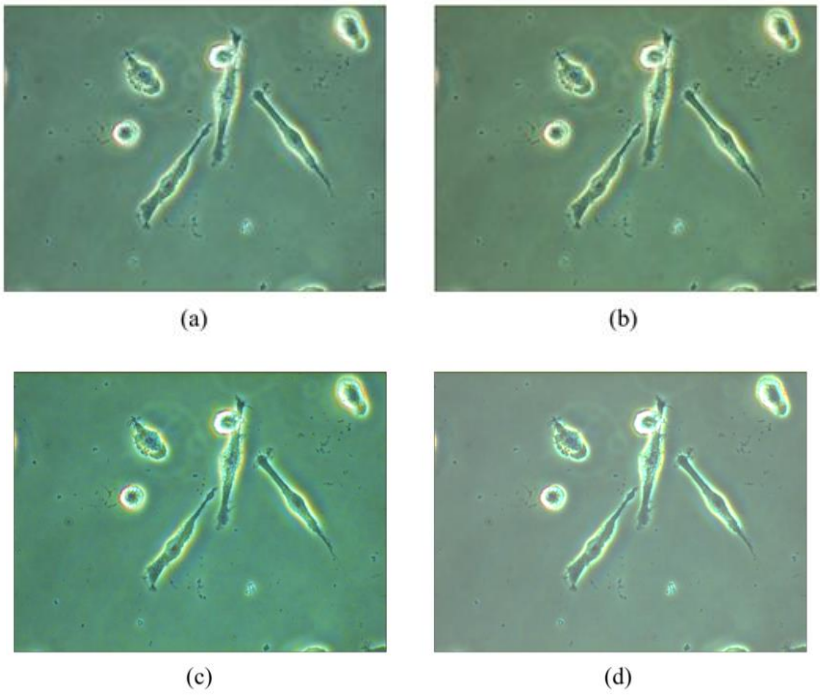

Figure 45. Examples of colour jittering: (a) original image; (b) hue-tuned image; (c) saturation-tuned image and (d) value-tuned image.

5.4 Loss curves of CELL-YOLO

The CELL-YOLO was trained and tested on an NVIDIA GTX machine with four GPUs of V100 Tesla. To test the learning ability of CELL-YOLO, the model was trained with 104, 306, 612 images, then validated with 12, 34 and 68 images, and hence generated the three-trained models denoted by CELL-YOLO^{104}, CELL-YOLO^{306}and CELL-YOLO^{612}. As shown in Figure 46, loss curves of CELL-YOLO^{104}, CELL-YOLO^{306}and CELL-YOLO^{612} were plotted to indicate the training processes during training.

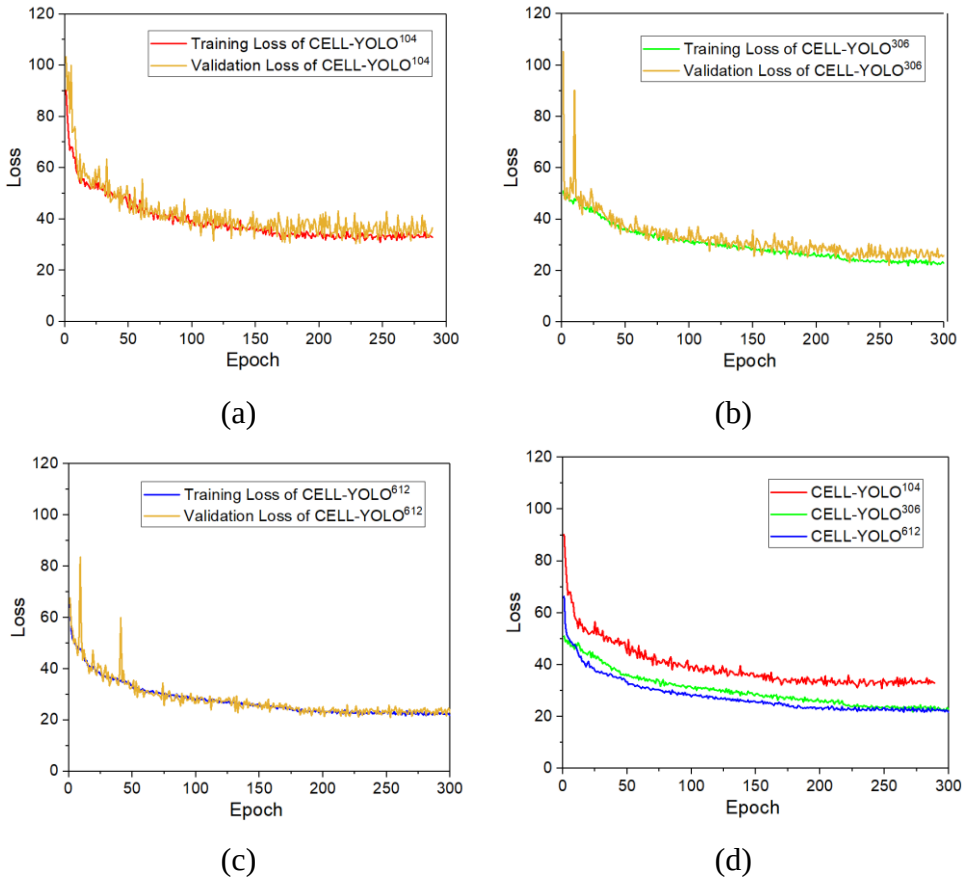

Figure 46. Loss curves of CELL-YOLO model. (a) Loss curves of CELL-YOLO^{104}. (b) Loss curves of CELL-YOLO^{306}. (c) Loss curves of CELL-YOLO^{612}. (d) Training loss curves of three models of CELL-YOLO^{104}, CELL-YOLO^{306} and CELL-YOLO^{612}.

Based on the above, the final losses of the above three models are summarized in Table 4. The training loss of CELL-YOLO^{104}, CELL-YOLO^{306}and CELL-YOLO^{612} became steady at 33.28, 23.25 and 22.17 at the final stage of training which converged up to around 300, 350 and 400 epochs during training. The steady loss values were acquired by averaging the last 50 loss values of each model during training.

Table 4. The training loss of CELL-YOLO^{104}, CELL-YOLO^{306}and AND CELL-YOLO^{612}

	CELL-YOLO^{104}	CELL-YOLO^{306}	CELL-YOLO^{612}
Steady Training Loss	33.28	23.25	22.17
Steady Validation Loss	36.09	26.51	22.98

5.5 Detection results and mAP of CELL-YOLO

The trained three models were tested with the same set of another 81 images to verify the detection performance. Figure 47 visualizes the testing results of CELL-YOLO for detecting cells in images acquired under the microscope. The ability of cell detection was enhanced when the size of our database for training was increased, as shown in Figure 47. The model trained with 104 images can detect the suitable and acceptable cells accurately but has no response to the unsuitable cell. After increasing the data size to 306 images, the model responded to unsuitable cells but wrongly recognised the unsuitable cells to be the acceptable cells. Further increasing the data size to 612 images, the model can accurately detect and distinguish all cell classes. Table 5 shows the mean average precision (mAP) and average precision (AP) of each class of the three models based on IoU =50%. These selected performance metrics are the standard metric of the COCO dataset and have been widely used in previous studies on object detection [115]. According to Figure 47, the performance of the CELL-YOLO model was enhanced by increasing the data size of the training set.

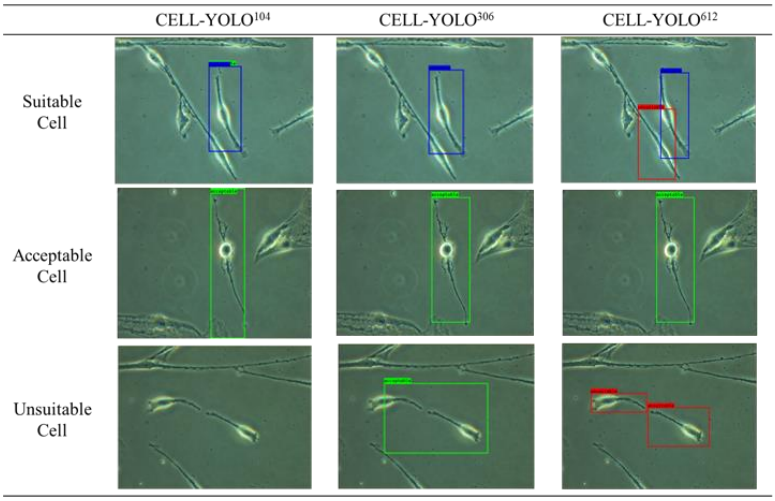

Figure 47. Examples of detections results of the biological cells using the three-trained models. The blue bounding box indicated "Suitable cells" detection. The green bounding box indicated "Acceptable cells" detection. The Red bound box indicated "Unsuitable cells" detection.

Table 5. mAP and AP of three classes of cells

	CELL-YOLO^{104}	CELL-YOLO^{306}	CELL-YOLO^{612}
mAP	14.76	21.43	35.65

AP of suitable cells	14	18	25
AP of acceptable cells	17	32	42
AP of unsuitable cells	14	14	40

To evaluate the effectiveness of the reweighted coefficient due to the class to the categorical part of the loss function as shown in Equation (5.2), the performance of CELL-YOLO^{612} is compared between with and without the reweighted coefficient. In this comparison, AP based on IoU=50% is still be chosen as the metric. In Table 6, the AP of suitable cells and the AP of acceptable cells of the model with the reweighted coefficients were increased by 7% and 1%, respectively, even though the AP of unsuitable cells was decreased by 4%. The results indicated that adding the reweighted coefficient in the loss function of CELL-YOLO^{612} could certainly weaken the negative effects of class imbalance.

Table 6. Performance comparison between the class-reweighted version and non-reweighted version of the CELL-YOLO^{612} model

	Class-reweighted version	Non-reweighted version
mAP	35.65	34.22
AP of suitable cells	25	18
AP of acceptable cells	42	41
AP of unsuitable cells	40	44

5.6 Comparison with YOLOV3 and YOLOV4

To demonstrate the superiority of the CELL-YOLO^{612}, its performance was compared with the baseline model, YOLOV3 and the latest mode of the YOLO series, YOLOV4. The comparison indexes include mAP$_{50}$ that mean average precision (mAP) is calculated with IoU = 50%; mAP$_{75}$ that mAP is calculated with IoU = 75%; and the processing speed in terms of frame per second (FPS). To make the comparison reasonable, the largest scale output of YOLOV3 was removed, and it was trained on

the same training set. Besides, the reweighted coefficients of categorical loss were added to the loss function of YOLOV3 and YOLOV4. The comparison indexes of CELL-YOLO^{612}, YOLOV3 and YOLOV4 have been summarized as shown in Table 7. Table 7 show, Even if the network's scale was smaller than YOLOV3 and YOLOV4, the mAP_{50}, mAP_{75}, and FPS of CELL-YOLO^{612} are higher than YOLOV3 and YOLOV4, which indicated that the proposed CELL-YOLO^{612} has higher accuracy and faster detection speed, and it is very suitable for biological cell detection under the limited amount of training set. Moreover, the FPS value indicated the detection speed of CELL-YOLO^{612} is 30, which is sufficiently high for the real-time application of the automated patch clamp, by taking consideration of the traditional video speed from 24 FPS to 30 FPS and the limit of human vision from 30 FPS to 60 FPS [116].

Table 7. Performance comparison between CELL-YOLO and YOLOV3

	mAP_{50}	mAP_{75}	FPS
CELL-YOLO^{612}	35.65	21.26	30
YOLOV3	33.17	17.22	21
YOLOV4	34.19	20.29	20

Figure 48 shows the detection results of CELL-YOLO^{612} and YOLOV3 and YOLOV4 for the same set of images in a visual way. The first row shows that CELL-YOLO^{612} could accurately detect the acceptable cell, but YOLOV3 detected the same object as different classes. At the same time, YOLOV3 and YOLOV4 both detected a cell that is not entirely shown in the image, as an unsuitable cell in image 1. The second row shows that CELL-YOLO^{612} can accurately detect suitable and unsuitable cells, but YOLOV3 selected a cell that is not shown entirely in the image and classified a suitable cell as an acceptable cell, and YOLOV4 missed a suitable cell during detection. The third row shows that CELL-YOLO^{612} could accurately detect suitable and unsuitable cells, but YOLOV3 wrongly classified a suitable cell as acceptable. In addition, YOLOV4 missed the unsuitable cell even though it can detect the suitable cell correctly in image 3.

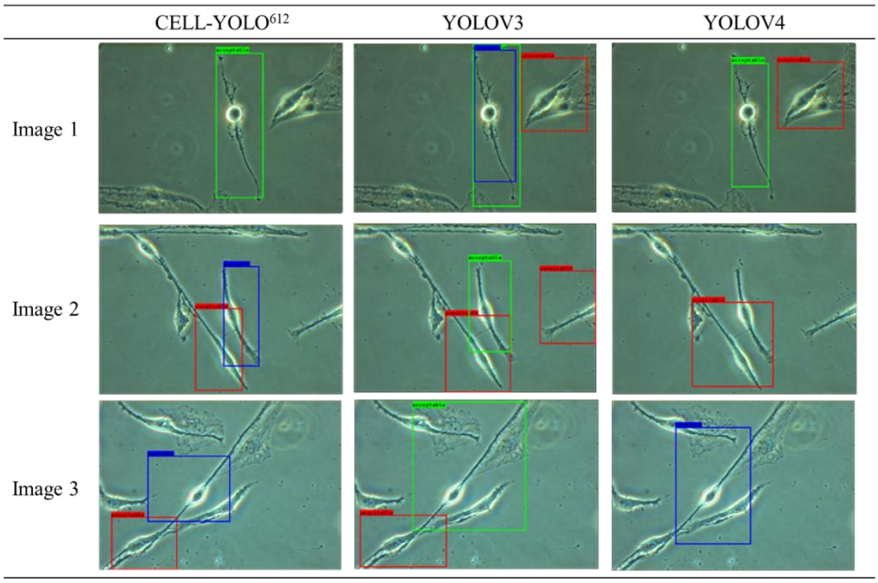

Figure 48. Detection results of CELL-YOLO612, YOLOV3 and YOLOV4. The blue bounding box indicates "Suitable cells" detection. The green bounding box indicates "Acceptable cells" detection. The Red bound box indicates "Unsuitable cells" detection.

5.7 Chapter summary

We have proposed the CELL-YOLO model to automatically select a suitable cell for the patch clamp experiment. The target cells are labelled in three classes in the training data collection: suitable, acceptable, and unsuitable. The model has been trained using this dataset with three different data sizes, and hence three trained models have been generated. The validation losses of CELL-YOLO^{104}, CELL-YOLO^{306} and CELL-YOLO^{612} are 36.09, 26.51 and 22.98, which converged to around 300 epochs or more. The performance of CELL-YOLO^{612} is the best among the three models, with the smallest loss for the specific application of cell detection for reducing the operational challenge of the patch clamp technique. Compared with our reference models (YOLOV3 and YOLOV4), CELL-YOLO^{612} has the highest accuracy and shortest processing time: the mAP_{50}, mAP_{75} and FPS of CELL-YOLO^{612} are 35.65, 21.26, and 30. The results show that the proposed AI method can be beneficial to the development of an automated patch clamp system for single cell analysis soon.

Chapter 6 Electrophysiological study of neural stem cells (NSC) differentiation

Neurodegenerative diseases have become a public health threat, especially in the region with the population ageing problem. Parkinson's disease (PD) is a brain disorder that leads to shaking and difficulty with walking, balance, and coordination. PD can arise from the degeneration of dopamine (DA) neurons in the region of substantia nigra (SN) in the basal ganglia of the brain. Stem cell therapies and cell transplantation are considered possible solutions for replacing damaged DA cells in the SN. To work toward the above application, we have a collaboration project led by the Department of Biology from Hong Kong Baptist University (HKBU) for the development of the neural stem cells by differentiation of the induced pluripotent stem (iPS) cells into NSC using the biocompatible extracellular matrices (ECMs) substrates, that are silica nonozigzags (NZs) and left-handed nanohelices (L-NHs), fabricated by the research group from Department of Physics from HKBU. Figure 49 shows the nano-structure of NZs substrate and L-NHs substrate

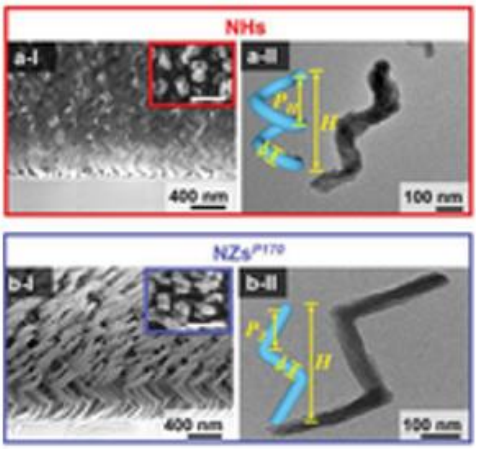

Figure 49. The nano-structure of the extracellular matrix (ECM). The red box shows the L-NHs. The blue shows the NZs [121].

To verify the feasibility of differentiating stem cells into neural stem cells (NSC) in vitro on various biocompatible extracellular matrices (ECMs), including silica nonozigzags (NZs), left-handed nanohelices (L-NHs) and typical glass slip as a control (CTR),

In this project, I was responsible for measuring the electrophysiological behaviours of iPS cells and hence verifying if the iPS cells have any neuronal activities by applying the developed patch clamp technique. Besides measuring the voltage-gated current response of the cell grown on NZs, I measured the response of the cell grown on L-NHs and a typical glass coverslip as the control (CTR) for comparison. In addition, the study for verifying if the zigzag pitch (P_z) is one of the key structural parameters of NZs substrate related to the induced organisation of NSC. There were three derivatives for the substrate of NZs, namely NZs^{P100}, NZs^{P160} and NZs^{P250}, respectively. Furthermore, we studied if another factor, day after plating (DAP), would affect the differentiation of iPS cell into NSC by measuring the signal firing and the ion channel activities using the current clamp and voltage clamp, respectively.

6.1 Materials and methodology of patch clamp recording for NSCs

Patch clamp is an electrophysiological technique to record the ion channel activities of neurogenic-induced stem cells. The whole-cell voltage clamp is used to record the total ion flow of an entire cell in response to voltage stimuli. During the recording, the adherent cell with a substrate is bathed with the extracellular solution inside a petri dish placed on an inverted microscope (Model: Eclipse Ti from Nikon, Tokyo, Japan). Inward and outward currents are recorded in the whole-cell voltage clamp configuration with an Axopatch 200B patch clamp amplifier, a Digidata 1440A data digitalizer and pClamp 10.7 software (all from Molecular Devices, Sunnyvale, CA, USA). Data are sampled at 50 kHz with low-pass filtered at 5 kHz. The extracellular solution is prepared using 160 mM NaCl, 4.5 mM KCl, 1 mM $MgCl_2$, 2 mM $CaCl_2$, 5 mM of glucose, and 10 mM of HEPES with pH adjustment to pH 7.4 using NaOH. The intracellular solution is prepared using 75 mM KCl, 10 mM NaCl, 70 mM KF, 2 mM $MgCl_2$, 10 mM HEPES, and 10 mM EGTA with pH adjustment to pH 7.2–7.4 using KOH.

6.2 Current response detection of differentiated NSC on different ECM using voltage clamp recording

The voltage clamp recording shows that both inward and outward ionic current of the cells grown on the substrate of NZs can be significantly elicited in response to the step voltage stimuli from -80 mV to 100 mV (Figure 50(a)). We found the Na^+ ion channel activities indicated by fast inward current peaking at -10 mV and the K^+ ion channel activities indicated by a slow and sustainable outward current peaking at 100 mV, as shown in Figure 50(b). This result indicates a range of activation like voltage-activated sodium currents of neuron cells.

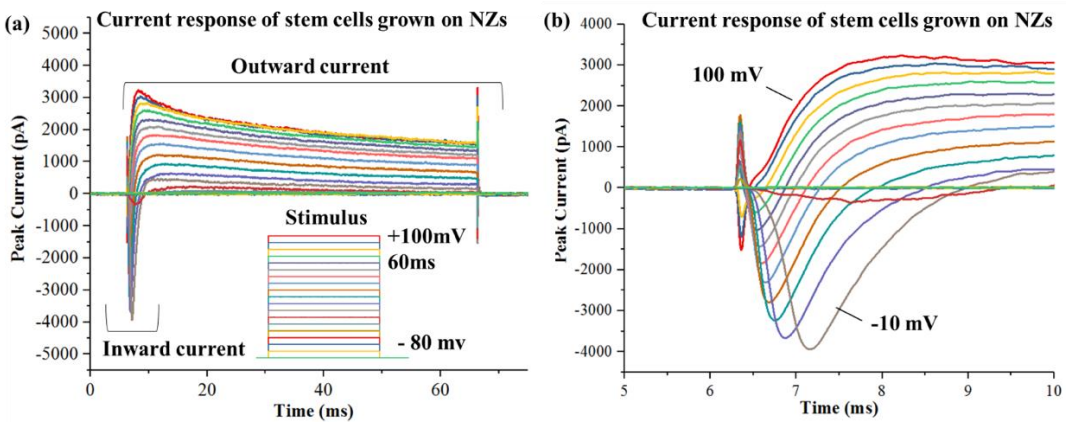

Figure 50. The current response of stem cells grown on NZs. (a) in full scale; (b) between 5 ms to 10 ms.

The voltage clamp recording has also been conducted using the iPS cell grown on L-NHs and CTR for comparison. Figure *51* shows the cell morphology is quite similar when they grew on CTR, L-NHs and NZs, respectively. For each recording, we converted the current amplitude per unit cell capacitance (proportion to cell surface area) to be peak current densities and then plotted against the step voltages stimulus to produce an IV graph. We conducted the voltage clamp recording at six cells for each substrate and summarised the results by using the average and derivatives in one IV graph, as shown in Figure 52. For comparison, we combined the three IV graphs into one IV graph, as shown in Figure 53.

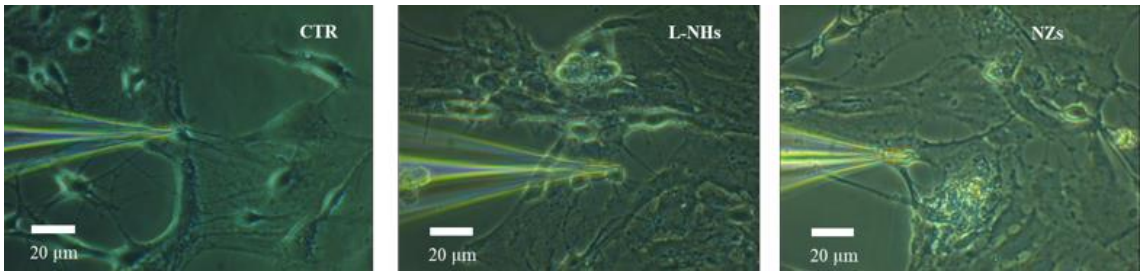

Figure 51. *Microscopic image of the iPSC on CTR, L-NHs and NZs during the patch clamp recording.*

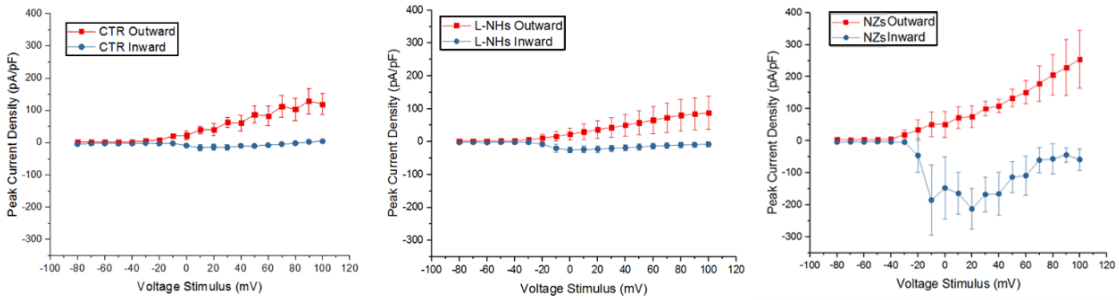

Figure 52. Peak current density against voltage stimulus of the cells grown on different substrates, the left shows the IV graph of the cell on CTR, the middle shows the IV graph of the cell on L-NHs, and the right shows the IV graph of the cell on NZs.

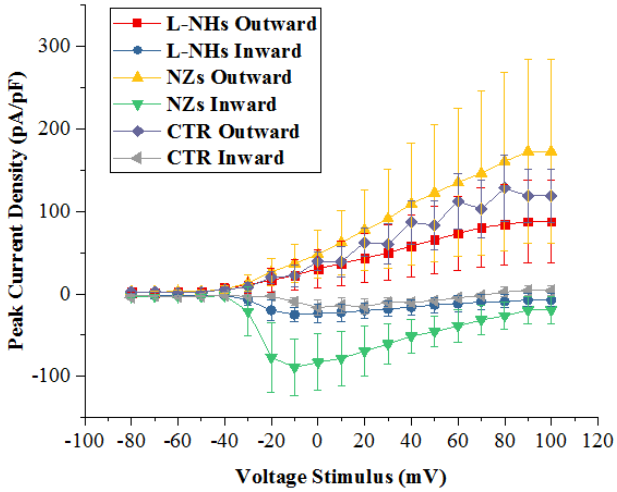

Figure 53. A summary of peak current density against voltage stimulus of the cells grown on different substrates

The current response of the stem cells grown on NZs showed the highest inward current and outward current value, similar to the fast Na^+ current and delayed rectifier K^+ currents in neurons. In contrast, the inward current of the stem cell grown on L-NHs and the control were not as obvious as the stem cell response on NZs.

Furthermore, the iPSC cells were grown on the derivative substrates of NZs, as shown in Figure 54. There are three derivatives for the substrate of NZs, namely NZs^{P100}, NZs^{P160} and $NZs^{P250,}$ which zigzag pitches **(**Pz) are 100 nm, 160 nm, and 250 nm, respectively. Figure 55 shows that both inward current and outward current elicitation happened on the cells grown on NZs^{P160} and NZs^{P250}. We conducted the voltage clamp recording at six cells for each substrate and summarised the results by using the average and derivatives in one IV graph, as shown in Figure 55. For comparison, we combined the three IV graphs into one IV graph, as shown in Figure 56. Figure 56 shows that the highest peak current density was found from the cell on NZs^{P250} substrate, but the curve of inward current density is not smooth, which implicates the cell may not be in a healthy condition. Hence, we concluded that the optimal pitch Pz could range from 160 nm to 250 nm. Twelve cells were recorded on each substrate when DAP is between 8 DAP and 18 DAP (days after plating). Therefore, we measured the ion channel activities and signal-firing of another 12 cells on each substrate for three different DAPs.

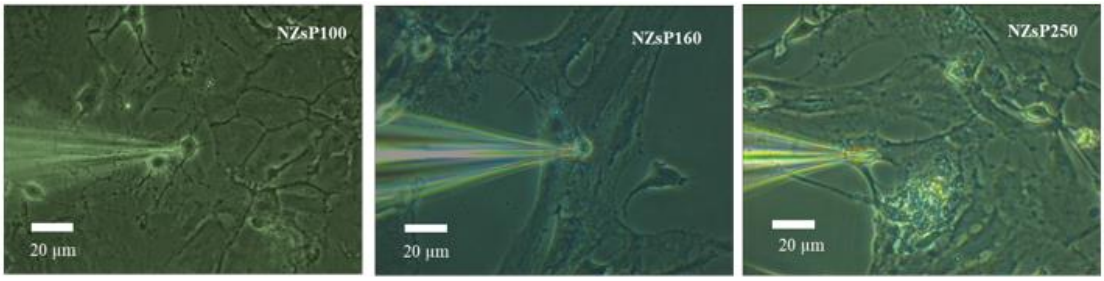

Figure 54. Microscopic image of the iPSC on NZsP100, NZsP160 and NZsP250 during the patch clamp recording

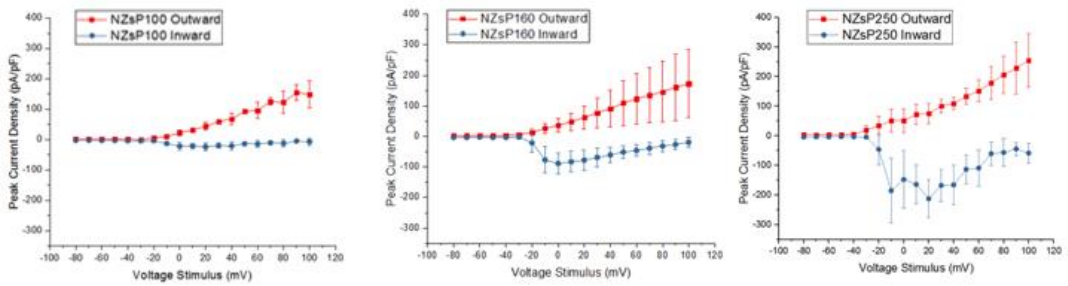

Figure 55. Peak current densities against voltage stimulus of the cells grown on three derivatives for the substrate of NZs: NZsP100 (left), NZsP160 (middle), and NZsP250 (Right)

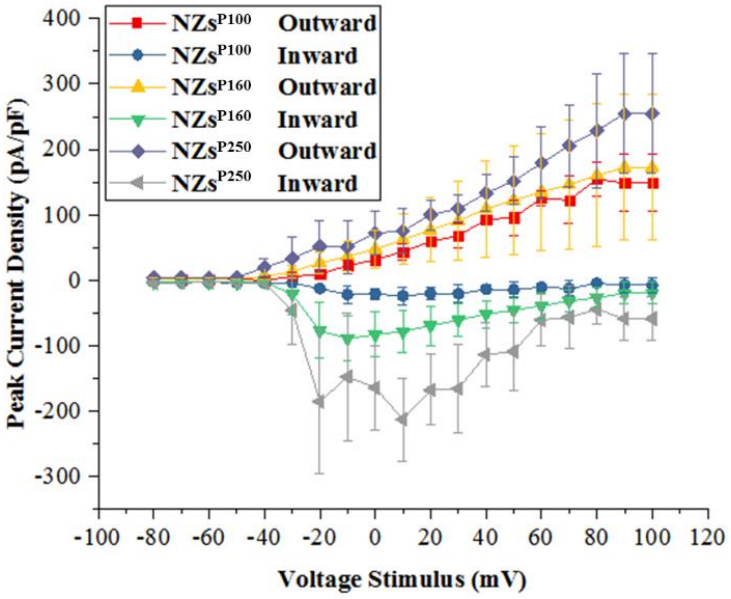

Figure 56. A summary of peak current densities against voltage stimulus of the cells grown on three derivatives for the substrate of NZs

6.3 Firing results of NSCs with differentiation time of days after plating (DAP) on NZs^{P165}

In the microscopic pictures (Figure 57), the growth of NSCs showed the gradual growth of dendrites from 8 DAP to 18 DAP during the differentiation [117]. These data indicated that NSCs can be induced to display more mature neuronal characteristics when the differentiation time is longer until 18 DAP. Moreover, the mature neuronal characteristics can be observed through the firing signal of NSCs. The firing of a neuron is driven by the opening of increasing numbers of voltage-gated sodium ion channels and the entry of sodium ions into the cell [118]. After an action potential occurs, the cell membrane will rapidly repolarize to its resting membrane potential with the opening of increasing numbers of voltage-gated potassium ion channels and the entry of potassium ions [118]. I applied 400-ms wide square-shaped current pulses from 20 pA to 80 pA with 20 pA increments. The pulses induced three action potentials responses under three development stages: 8 days after plating (DAP) on NZs^{P165}, 14 DAP and 18 DAP (Figure 58). 5 DA cells were measured in each development stage in each development stage, and 3 development stages were investigated in each trial. The experiments were repeated 3 times. At 8 DAP, one firing was observed at the beginning of the current pulse application at all current pulse applications. At 14 DAP and 18

DAP, more firings were observed. At 14 DAP, there are 3 to 4 firings at the beginning of 90-ms at 60 pA and 80 pA, while 1 firing happened at the beginning of 90-ms at 20 pA and 40 pA. At 18 DAP, there are 18 to 19 firings at the beginning of 90-ms at all given current application. In addition, the amplitude of the action potential firing increases gradually when the amplitude of the current application increases. The results of the DA neurons at 18 DAP agreed with other research groups, which found the matured dopaminergic neurons with typical pace-making spike train from 20 pA to 60 pA with 20 pA increment [119]. It also agrees with induced dopamine neurons' action potential firing characteristics [120].

In addition, the NSCs of 18 DAP has the highest outward current flow and inward current flow under the voltage stimulus from -60 mV to +40 mV with 10 mV increment as shown in Figure 59 and Figure 60. The outward current flow is the potassium ion channel activities, while the inward current flow is the sodium ion channel activities. Both potassium ion channel activities following sodium ion channel activities are typical neuronal characteristics. The peak inward current flows are -0.60 nA and -1.12 nA, and -1.40 nA, while the peak outward current flows are 0.44 nA, 1.01 nA and 1.94 nA at 8 DAP, 14 DAP and 18 DAP, respectively. The data revealed that the dopamine neuronal characteristic is more mature when the differentiation time is longer until 18 DAP.

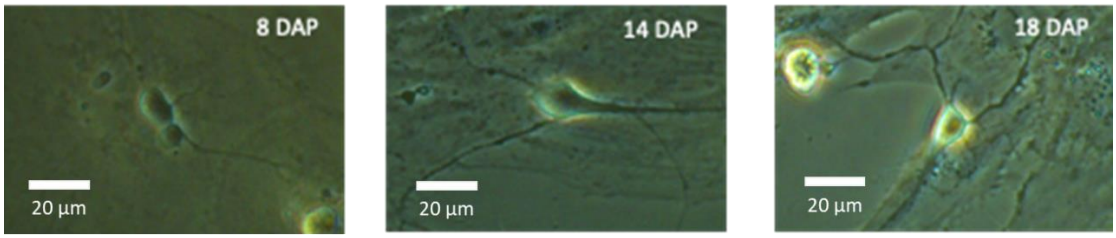

Figure 57. Microscopic image of a NSC on NZs^{P165} under three different development stages: 8 days after plating (DAP) on NZs^{P165}, 14 DAP and 18 DAP.

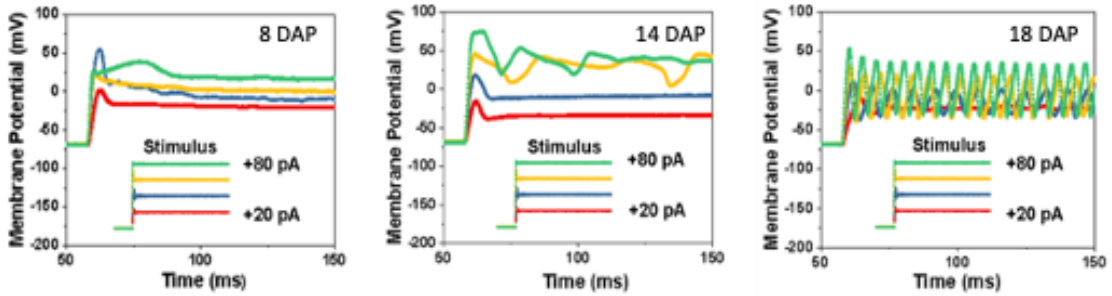

Figure 58. Representative traces of membrane potential of a NSC responding to step depolarization were recorded by the current clamp under three different development stages: 8 days after plating (DAP) in coverslips, 14 DAP and 18 DAP.

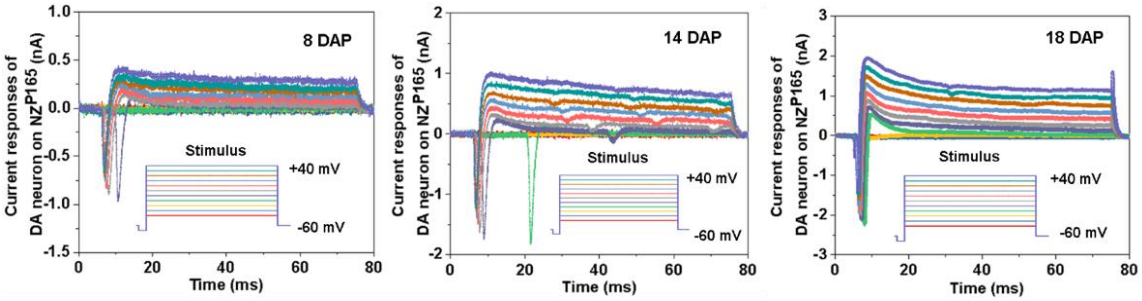

Figure 59. Representative traces of voltage-dependent sodium currents in an induced NSC Membrane potential was initially held at -90 mV and incrementally increased from -60 to +40 mV in 10 mV depolarizing steps

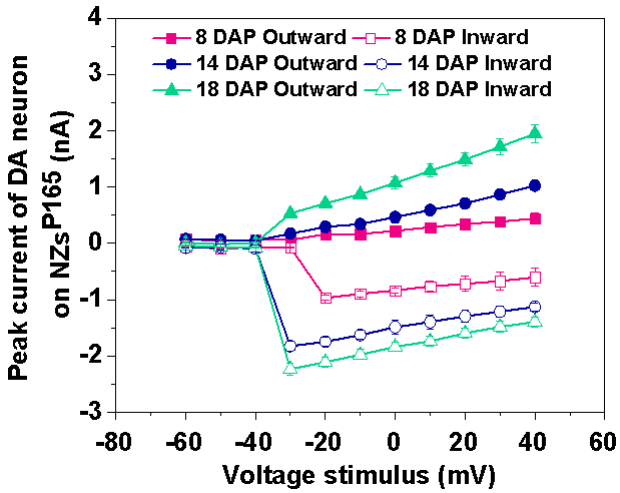

Figure 60. Current-voltage curve of current recording under voltage stimuli. Upper: current-voltage curve of outward current (Potassium current). Lower: current-voltage curve of inward current (Sodium current).

6.4 Chapter summary

In this study, both voltage clamp recording and current clamp recording of patch clamp techniques have been applied to record the electrophysiological behaviours of stem cells grown on ECMs to check if any neuronal activities can be recorded and hence verify if stem cells can be differentiated into neural stem cells (NSC). Silica nonozigzags (NZs) is a more effective substrate than left-handed nanohelices (L-NHs) and typical glass slip. Among three derivatives of the substrate of NZs, namely NZs^{P100}, NZs^{P160} and $NZs^{P250,}$ which P_z = 100 nm, 160 nm, and 250 nm, the current response of NSC on NZs^{P250} give the largest current response under the same set of voltage stimuli. Furthermore, using NZs^{P250} as a substrate, the morphology of the living cells in which dendrites have been developed at 14 DAP and 18 DAP, and the signal firing is the most significant at 18 DAP.

Chapter 7 Conclusions and Future Works

7.1 Conclusions

The research project aims to develop an effective patch clamp technique for both ion channel activities recording and cell cytoplasmic microinjection monitoring, for both cell lines and stem cells, a label-free cell detection using deep learning small adherent cells. The cell microinjection method not only can give reliable and spontaneous feedback when the target solution is injected, but also can verify the cell viability after the microinjection. In addition, cell identification using deep learning is designed to identify the cell condition before the patch clamp technique and hence enhance the success rate of the patch clamp recording.

To conclude, we developed a microinjection process with current feedback using the patch clamp technique for small and non-spherical living cells, developed an equivalent electrical model and equivalent circuit for monitoring the real-time response during the microinjection and verifying the viability of the cells after the microinjection, developed a deep learning approach to automatically select healthy biological cells during the patch clamp recording process and hence enhance the success rate of the electrophysiological recording, and applied both voltage clamp recording and current clamp recording of patch clamp techniques to record the electrophysiological behaviours of induced pluripotent stem cells grown on biocompatible extracellular matrices to confirm if neuronal stem cells have been successfully developed.

7.2 Future works

Since the development of deep learning technology is tremendous, I believe the biomedical application of deep learning can have many opportunities. For the patch clamp operation, many cell lines having subtle features led to the challenges of cell hunting operation. After this work, this research can be extended to other types of cell lines besides SHSY-5Y and HEK-293 that were used in these studies. Using the developed technique, our research group can load various drugs into intracellular

solutions for injection to achieve specific biomedical functions. Besides the patch clamp operation, the cell identification using deep learning can be applied to the injection operation. Lastly, we can apply deep learning methods to study the electrophysiological behaviour besides the cell morphology of cells.

References:

[1] B. Hille, *Ion channels of excitable membranes*, vol. 507. Sinauer Sunderland, MA, 2001.

[2] F. Kukita, 'Progress in a study of ion channels for 50 years', *Biophysics*, vol. 45, pp. 10–15, 2005.

[3] D. J. Aidley and P. R. Stanfield, 'Ion Channels: Molecules in Action', *Cell*, vol. 89, no. 6, pp. 829–830, 1997.

[4] J. Koester and S. A. Siegelbaum, 'Membrane potential', *Princ. Neural Sci.*, vol. 4, pp. 125–139, 1991.

[5] R. M. Spanswick, 'Electrogenic ion pumps', *Annu. Rev. Plant Physiol.*, vol. 32, no. 1, pp. 267–289, 1981.

[6] E. R. Kandel, J. H. Schwartz, T. M. Jessell, S. A. Siegelbaum, and A. J. Hudspeth, *Principles of neural science*, vol. 4. McGraw-hill New York, 2000.

[7] H. Bostock, M. K. Sharief, G. Reid, and N. M. F. Murray, 'Axonal ion channel dysfunction in amyotrophic lateral sclerosis', *Brain*, vol. 118, no. 1, pp. 217–225, 1995.

[8] S. K. Bagal *et al.*, 'Ion channels as therapeutic targets: a drug discovery perspective', *J. Med. Chem.*, vol. 56, no. 3, pp. 593–624, 2012.

[9] Y. Okada, *Patch clamp techniques: from beginning to advanced protocols*. Springer Tokyo/New York, 2012.

[10] M. B. Goodman, T. H. Lindsay, S. R. Lockery, and J. E. Richmond, 'Electrophysiological methods for Caenorhabditis elegans neurobiology', *Methods Cell Biol.*, vol. 107, pp. 409–436, 2012.

[11] D. Geraghty and L. D. Rash, *Ion Channels Down Under*. Academic Press, 2017.

[12] M. Martina and S. Taverna, 'Patch clamp Methods and Protocols', *Methods Mol. Biol.*, 2014.

[13] D. Ogden and P. Stanfield, 'Patch clamp techniques for single channel and whole-cell recording', *Microelectrode Tech.*, pp. 53–78, 1994.

[14] B. Sakmann and E. Neher, 'Single channel currents recorded from membrane of denervated frog muscle fibers', *Nature*, vol. 260, no. 5554, pp. 799–802, 1976.

[15] O. P. Hamill, A. Marty, E. Neher, B. Sakmann, and F. J. Sigworth, 'Improved Patch clamp techniques for high-resolution current recording from cells and cell-free membrane patches', *Pflüg. Arch.*, vol. 391, no. 2, pp. 85–100, 1981.

[16] M. Kakei, A. Noma, and T. Shibasaki, ‘Properties of adenosine-triphosphate-regulated potassium channels in guinea-pig ventricular cells.’, *J. Physiol.*, vol. 363, p. 441, 1985.

[17] E. S. Levitan and R. H. Kramer, ‘Neuropeptide modulation of single calcium and potassium channels detected with a new patch clamp configuration’, 1990.

[18] R. Horn and A. Marty, ‘Muscarinic activation of ionic currents measured by a new whole-cell recording method.’, *J. Gen. Physiol.*, vol. 92, no. 2, pp. 145–159, 1988.

[19] E. M. Zayas and G. T. Grossberg, ‘Treating the agitated Alzheimer patient.’, *J. Clin. Psychiatry*, vol. 57, pp. 46–51, 1995.

[20] A. Marty and E. Neher, ‘Tight-seal whole-cell recording’, in *Single-channel recording*, Springer, 1995, pp. 31–52.

[21] G. J. Stuart, H. U. Dodt, and B. Sakmann, ‘Patch clamp recordings from the soma and dendrites of neurons in brain slices using infrared video microscopy’, *Pflüg. Arch.*, vol. 423, no. 5–6, pp. 511–518, 1993.

[22] A. Obergrussberger, S. Friis, A. Brüggemann, and N. Fertig, ‘Automated patch clamp in drug discovery: major breakthroughs and innovation in the last decade’, *Expert Opin. Drug Discov.*, vol. 16, no. 1, pp. 1–5, Jan. 2021, doi: 10.1080/17460441.2020.1791079.

[23] R. Yang, K. W. C. Lai, N. Xi, and J. Yang, ‘Development of automated patch clamp system for electrophysiology’, in *2013 IEEE International Conference on Robotics and Biomimetics (ROBIO)*, Shenzhen, China, Dec. 2013, pp. 2185–2190. doi: 10.1109/ROBIO.2013.6739793.

[24] R. Yang, K. W. C. Lai, N. Xi, and J. Yang, ‘Development of automated patch clamp system for electrophysiology’, *2013 IEEE Int. Conf. Robot. Biomim. ROBIO 2013*, no. December, pp. 2185–2190, 2013, doi: 10.1109/ROBIO.2013.6739793.

[25] S. Stoelzle-Feix, ‘State-of-the-art automated patch clamp: Heat activation, action potentials, and high throughput in ion channel screening’, *Methods Mol. Biol.*, vol. 1183, no. November, pp. 65–80, 2014, doi: 10.1007/978-1-4939-1096-0_4.

[26] X. Yajuan, L. Xin, and L. Zhiyuan, ‘A Comparison of the Performance and Application Differences Between Manual and Automated Patch clamp Techniques’, *Curr. Chem. Genomics*, vol. 6, pp. 87–92, 2013, doi: 10.2174/1875397301206010087.

[27] Y. Sun and B. J. Nelson, ‘Biological Cell Injection Using an Autonomous MicroRobotic System’, *The International Journal of Robotics Research*, vol. 21, no. 10–11. pp. 861–868, 2002.

[28] E. Kwon, Y. Kim, and D. Kim, ‘Investigation of penetration force of living cell using an atomic force microscope.’, *J. Mech. Sci. Technol.*, vol. 23, pp. 1932–1938, 2009, doi: 10.1007/s12206-009-0508-z.

[29] P. H. Wu, C. M. Hale, W. C. Chen, J. S. H. Lee, Y. Tseng, and D. Wirtz, ‘High-throughput ballistic injection nanorheology to measure cell mechanics.’, *Nat. Protoc.*, vol. 7, no. 1, pp. 155–70, 2012.

[30] J. Gao, X. F. Yin, and Z. L. Fang, ‘Integration of single cell injection, cell lysis, separation and detection of intracellular constituents on a microfluidic chip’, *Lab. Chip*, vol. 4, no. 1, pp. 47–52, 2004, doi: 10.1039/b310552k.

[31] A. Prokop and J. M. Davidson, ‘Nanovehicular intracellular delivery systems’, *Journal of Pharmaceutical Sciences*, vol. 97, no. 9. pp. 3518–3590, 2008.

[32] C. S. O. Paulo, R. Pires das Neves, and L. S. Ferreira, ‘Nanoparticles for intracellular-targeted drug delivery’, *Nanotechnology*, vol. 22, no. 49. p. 494002, 2011.

[33] C. E. Thomas, A. Ehrhardt, and M. A. Kay, ‘Progress and problems with the use of viral vectors for gene therapy.’, *Nat. Rev. Genet.*, vol. 4, no. May, pp. 346–358, 2003, doi: 10.1038/nrg1066.

[34] Y. Wang *et al.*, ‘Poking cells for efficient vector-free intracellular delivery.’, *Nat. Commun.*, vol. 5, p. 4466, 2014.

[35] T. Nakayama, H. Fujiwara, K. Tastumi, K. Fujita, T. Higuchi, and T. Mori, ‘A new assisted hatching technique using a piezo-micromanipulator’, *Fertil. Steril.*, vol. 69, no. 4, pp. 784–788, 1998.

[36] W. Wang, X. Liu, D. Gelinas, B. Ciruna, and Y. Sun, ‘A fully automated robotic system for microinjection of zebrafish embryos’, *PloS One*, vol. 2, no. 9, p. e862, 2007.

[37] Y. Xie, D. Sun, C. Liu, H. Y. Tse, and S. H. Cheng, ‘A force control approach to a robot-assisted cell microinjection system’, *Int. J. Robot. Res.*, vol. 29, no. 9, pp. 1222–1232, 2010.

[38] Q. Xu, ‘Review of Microinjection Systems’, in *Micromachines for Biological Micromanipulation*, Springer, 2018, pp. 15–47.

[39] H. Huang, D. Sun, H. Su, and J. K. Mills, ‘Force sensing and control in robot-assisted suspended cell injection system’, in *Advances in Robotics and Virtual Reality*, Springer, 2012, pp. 61–88.

[40] Y. Zhang, ‘Microinjection technique and protocol to single cells’, *Protoc. Exch.*, vol. 10, 2007.

[41] Y. Zhang and L. C. Yu, ‘Single-cell microinjection technology in cell biology’, *BioEssays*, vol. 30, no. 6, pp. 606–610, 2008, doi: 10.1002/bies.20759.

[42] A. Ghanbari, W. Wang, C. E. Hann, J. G. Chase, and X. Chen, ‘Cell image recognition and visual servo control for automated cell injection’, *Autonomous Robots and Agents, 2009. ICARA 2009. 4th International Conference on*. pp. 92–96, 2009. doi: 10.1109/ICARA.2000.4803986.

[43] Y. T. Chow, S. Chen, R. Wang, C. Liu, C. Kong, and R. A. Li, ‘Single Cell Transfection through Precise Microinjection with Quantitatively Controlled Injection Volumes’, *Sci. Rep.*, vol. 6, no. January, pp. 1–9, 2016, doi: 10.1038/srep24127.

[44] X. Liu, K. Kim, Y. Zhang, and Y. Sun, ‘Nanonewton force sensing and control in microrobotic cell manipulation’, *Int. J. Robot. Res.*, vol. 28, no. 8, pp. 1065–1076, 2009, doi: 10.1177/0278364909340212.

[45] A. Pillarisetti, M. Pekarev, A. D. Brooks, and J. P. Desai, ‘Evaluating the Effect of Force Feedback in Cell Injection’, *IEEE Trans. Autom. Sci. Eng.*, vol. 4, no. 3, pp. 322–331, Jul. 2007, doi: 10.1109/TASE.2006.888051.

[46] H. B. Huang, D. Sun, S. Member, J. K. Mills, and S. H. Cheng, ‘Robotic cell injection system with position and force control: Toward automatic batch biomanipulation.’, *IEEE Trans. Robot.*, vol. 25, no. 3, pp. 727–737, 2009.

[47] H. Huang, J. K. Mills, C. Lu, and D. Sun, ‘A universal piezo-driven ultrasonic cell microinjection system’, *Biomed. Microdevices*, vol. 13, no. 4, pp. 743–752, Aug. 2011, doi: 10.1007/s10544-011-9544-4.

[48] F. Karimirad, S. Chauhan, and B. Shirinzadeh, ‘Vision-based force measurement using neural networks for biological cell microinjection’, *J. Biomech.*, vol. 47, no. 5, pp. 1157–1163, 2014, doi: 10.1016/j.jbiomech.2013.12.007.

[49] H. Huang, D. Sun, J. K. Mills, W. J. Li, and S. H. Cheng, ‘Visual-based impedance control of out-of-plane cell injection systems’, *IEEE Trans. Autom. Sci. Eng.*, vol. 6, no. 3, pp. 565–571, 2009.

[50] J. Liu *et al.*, ‘Robotic Adherent Cell Injection for Characterizing Cell–Cell Communication’, *IEEE Trans. Biomed. Eng.*, vol. 62, no. 1, 2015.

[51] S. Permana, E. Grant, G. M. Walker, and J. A. Yoder, ‘A review of automated microinjection systems for single cells in the embryogenesis stage’, *IEEEASME Trans. Mechatron.*, vol. 21, no. 5, pp. 2391–2404, 2016, doi: 10.1109/TMECH.2016.2574871.

[52] Y. T. Chow *et al.*, ‘A high throughput automated microinjection system for human cells with small size’, *IEEEASME Trans. Mechatron.*, vol. 21, no. 2, pp. 838–850, 2016, doi: 10.1109/TMECH.2015.2476362.

[53] S. Yu and B. J. Nelson, ‘Autonomous injection of biological cells using visual servoing’, *Exp. Robot.*, vol. 7, no. LNCIS 271, pp. 169–178, 2001.

[54] Y. Sun and B. J. Nelson, ‘Biological cell injection using an autonomous microrobotic system’, *Int. J. Robot. Res.*, vol. 21, no. 10–11, pp. 861–868, 2002, doi: 10.1177/027836490202101083 3.

[55] Y. Xie, D. Sun, C. Liu, H. Y. Tse, and S. H. Cheng, ‘A force control approach to a robot-assisted cell microinjection system’, *Int. J. Robot. Res.*, vol. 29, no. 9, pp. 1222–1232, 2010, doi: 10.1177/0278364909354325.

[56] R. A. Seger, P. A. Actis, P. Catherine, M. Maaolouf, B. Vilozny, and N. Pourmand, ‘Voltage controlled nano-injection system for single-cell surgery’, *Nanoscale*, vol. 4, no. 19, pp. 5843–5846, 2012, doi: 10.1177/1043454210368532.Analysis.

[57] T. Hamid, M. T. Malik, and S. S. Kakar, ‘Ectopic expression of PTTG1/securin promotes tumorigenesis in human embryonic kidney cells’, *Mol. Cancer*, vol. 4, no. 1, p. 3, 2005.

[58] R. Francis *et al.*, ‘Connexin43 modulates cell polarity and directional cell migration by regulating microtubule dynamics’, *PloS One*, vol. 6, no. 10, p. e26379, 2011.

[59] S. Xiong *et al.*, ‘Neuroprotective effects of a novel peptide, FK18, under oxygen-glucose deprivation in SH-SY5Y cells and retinal ischemia in rats via the Akt pathway’, *Neurochem. Int.*, vol. 108, pp. 78–90, 2017.

[60] M. J. Bours, P. C. Dagnelie, A. L. Giuliani, A. Wesselius, and F. Di Virgilio, ‘P2 receptors and extracellular ATP: a novel homeostatic pathway in inflammation’, *Front Biosci Sch. Ed*, vol. 3, pp. 1443–1456, 2011.

[61] S. Permana, E. Grant, G. M. Walker, and J. A. Yoder, ‘A review of automated microinjection systems for single cells in the embryogenesis stage’, *IEEEASME Trans. Mechatron.*, vol. 21, no. 5, pp. 2391–2404, 2016.

[62] P. Kallio and J. Kuncova-Kallio, ‘Capillary pressure microinjection of living adherent cells: challenges in automation’, *J. Micromechatronics*, vol. 3, no. 3–4, pp. 189–220, 2006.

[63] A. Meister *et al.*, ‘FluidFM: combining atomic force microscopy and nanofluidics in a universal liquid delivery system for single cell applications and beyond’, *Nano Lett.*, vol. 9, no. 6, pp. 2501–2507, 2009.

[64] F. H. L. Chan, R. Yang, and K. W. C. Lai, ‘Development of the electric equivalent model for the cytoplasmic microinjection of small adherent cells’, *Micromachines*, vol. 8, no. 7, p. 216, 2017.

[65] X. Wang and M. Li, ‘Automated electrophysiology: high throughput of art.’, *Assay Drug Dev. Technol.*, vol. 1, no. 5, pp. 695–708, 2003, doi: 10.1089/154065803770381057.

[66] L. Wroblewska *et al.*, ‘Automated whole-cell patch clamp electrophysiology of neurons in vivo’, *Nat. Methods*, vol. 33, no. 8, pp. 839–841, 2016, doi: 10.1038/nbt.3301.Mammalian.

[67] Y. Zhao, S. Inayat, D. A. Dikin, J. H. Singer, R. S. Ruoff, and J. B. Troy, ‘Patch clamp technique: Review of the current state of the art and potential contributions from nanoengineering’, *Proc. Inst. Mech. Eng. Part N J. Nanoeng. Nanosyst.*, vol. 222, no. 1, pp. 1–11, 2008, doi: 10.1243/17403499JNN149.

[68] N. Fertig and C. Farre, ‘Renaissance of ion channel research and drug discovery by patch clamp automation’, *Future Med. Chem.*, vol. 2, no. 5, pp. 691–695, 2010, doi: 10.4155/fmc.10.183.

[69] O. Scheel, S. Frech, B. Amuzescu, J. Eisfeld, K. H. Lin, and T. Knott, ‘Action potential characterization of human induced pluripotent stem cell-derived cardiomyocytes using automated Patch clamp technology’, *Assay Drug Dev. Technol.*, vol. 12, no. 8, pp. 457–469, 2014, doi: 10.1089/adt.2014.601.

[70] R. Yang, K. W. C. Lai, Y. Fang, N. Xi, and J. Yang, ‘Development of a nanorobotic station for electrophysiology under nanomechanical stimulation’, in *2013 13th IEEE International Conference on Nanotechnology (IEEE-NANO 2013)*, Beijing, China, Aug. 2013, pp. 213–216. doi: 10.1109/NANO.2013.6720942.

[71] C. Wood, C. Williams, and G. J. Waldron, ‘Patch clamping by numbers’, *Drug Discov. Today*, vol. 9, no. 10, pp. 434–441, 2004, doi: 10.1016/S1359-6446(04)03064-8.

[72] Z.-Q. Zhao, P. Zheng, S.-T. Xu, and X. Wu, ‘Object Detection With Deep Learning: A Review’, *IEEE Trans. Neural Netw. Learn. Syst.*, vol. 30, no. 11, pp. 3212–3232, Nov. 2019, doi: 10.1109/TNNLS.2018.2876865.

[73] X. Wu, D. Sahoo, and S. C. H. Hoi, ‘Recent advances in deep learning for object detection’, *Neurocomputing*, vol. 396, pp. 39–64, Jul. 2020, doi: 10.1016/j.neucom.2020.01.085.

[74] H. Bay, T. Tuytelaars, and L. Van Gool, ‘SURF: Speeded Up Robust Features’, in *Computer Vision – ECCV 2006*, vol. 3951, A. Leonardis, H. Bischof, and A. Pinz, Eds. Berlin, Heidelberg: Springer Berlin Heidelberg, 2006, pp. 404–417. doi: 10.1007/11744023_32.

[75] D. G. Lowe, ‘Distinctive Image Features from Scale-Invariant Keypoints’, *Int. J. Comput. Vis.*, vol. 60, no. 2, pp. 91–110, Nov. 2004, doi: 10.1023/B:VISI.0000029664.99615.94.

[76] T. Ojala, M. Pietikainen, and T. Maenpaa, ‘Multiresolution gray-scale and rotation invariant texture classification with local binary patterns’, *IEEE Trans. Pattern Anal. Mach. Intell.*, vol. 24, no. 7, pp. 971–987, Jul. 2002, doi: 10.1109/TPAMI.2002.1017623.

[77] A. Krizhevsky, I. Sutskever, and G. E. Hinton, ‘ImageNet classification with deep convolutional neural networks’, *Commun. ACM*, vol. 60, no. 6, pp. 84–90, May 2017, doi: 10.1145/3065386.

[78] Y. Lecun, Y. Bengio, and G. Hinton, ‘Deep learning’, *Nature*, vol. 521, no. 7553, pp. 436–444, 2015, doi: 10.1038/nature14539.

[79] X. Glorot, A. Bordes, and Y. Bengio, ‘Deep Sparse Rectifier Neural Networks’, p. 9.

[80] K. Simonyan and A. Zisserman, ‘Very Deep Convolutional Networks for Large-Scale Image Recognition’, *ArXiv14091556 Cs*, Apr. 2015, Accessed: Sep. 03, 2021. [Online]. Available: http://arxiv.org/abs/1409.1556

[81] C. Szegedy, V. Vanhoucke, S. Ioffe, J. Shlens, and Z. Wojna, ‘Rethinking the Inception Architecture for Computer Vision’, in *2016 IEEE Conference on Computer*

Vision and Pattern Recognition (CVPR), Las Vegas, NV, USA, Jun. 2016, pp. 2818–2826. doi: 10.1109/CVPR.2016.308.

[82] C. Szegedy, S. Ioffe, V. Vanhoucke, and A. A. Alemi, 'Inception-v4, Inception-ResNet and the Impact of Residual Connections on Learning', p. 7.

[83] K. He, X. Zhang, S. Ren, and J. Sun, 'Deep Residual Learning for Image Recognition', in *2016 IEEE Conference on Computer Vision and Pattern Recognition (CVPR)*, Las Vegas, NV, USA, Jun. 2016, pp. 770–778. doi: 10.1109/CVPR.2016.90.

[84] R. Girshick, J. Donahue, T. Darrell, and J. Malik, 'Rich Feature Hierarchies for Accurate Object Detection and Semantic Segmentation', in *2014 IEEE Conference on Computer Vision and Pattern Recognition*, Columbus, OH, USA, Jun. 2014, pp. 580–587. doi: 10.1109/CVPR.2014.81.

[85] R. Girshick, 'Fast r-cnn', in *Proceedings of the IEEE international conference on computer vision*, 2015, pp. 1440–1448.

[86] S. Ren, K. He, R. Girshick, and S. Jian, 'Faster R-CNN: Towards Real-Time Object Detection with Region Proposal Networks Shaoqing', *Adv. Neural Inf. Process. Syst.*, pp. 241–294, 2015, doi: 10.2307/j.ctt1d98bxx.10.

[87] J. Dai, Y. Li, K. He, and J. Sun, 'R-FCN: Object Detection via Region-based Fully Convolutional Networks', *ArXiv160506409 Cs*, Jun. 2016, Accessed: Sep. 07, 2021. [Online]. Available: http://arxiv.org/abs/1605.06409

[88] J. S. D. R. G. A. F. Redmon, '(YOLO) You Only Look Once: Unified, Real-Time Object Detection', *Proc. IEEE Conf. Comput. Vis. Pattern Recognit.*, 2016, doi: 10.1109/CVPR.2016.91.

[89] J. Redmon and A. Farhadi, 'YOLOv3: An Incremental Improvement', 2018.

[90] J. Redmon and A. Farhadi, 'YOLO9000: Better, Faster, Stronger', in *Proceedings of the IEEE conference on computer vision and pattern recognition*, pp. 7263–7271.

[91] A. Bochkovskiy, C.-Y. Wang, and H.-Y. M. Liao, 'YOLOv4: Optimal Speed and Accuracy of Object Detection', 2020.

[92] W. Liu *et al.*, 'SSD: Single Shot MultiBox Detector', in *Computer Vision – ECCV 2016*, Cham, 2016, pp. 21–37.

[93] T.-Y. Lin, P. Goyal, R. Girshick, K. He, and P. Dollar, 'Focal Loss for Dense Object Detection', p. 9.

[94] H. Law and J. Deng, 'CornerNet: Detecting Objects as Paired Keypoints', p. 17.

[95] J. Zheng and M. C. Trudeau, *Handbook of ion channels.* CRC Press, 2015.

[96] D. L. Yprey and L. J. Defelice, 'The Patch clamp Technique Explained and Exercised with the Use of Simple Electrical Equivalent Circuits', in *'Electrical Properties of Cells,* 2000, p. 7.

[97] B. Hille, *Ion channels of excitable membranes*, vol. 507. Sinauer Sunderland, MA, 2001.

[98] M. Martina, S. Taverna, and T. Taverna, 'Patch clamp Methods and Protocols', *Methods Mol. Biol.*, 2014.

[99] B. Sakmann and E. Neher, *Single-channel recording*. Springer Science & Business Media, 2013.

[100] W. F. Boron and E. L. Boulpaep, *Medical Physiology a Cellular and Molecular Approach,* vol. 53, no. 9. 2013. doi: 10.1017/CBO9781107415324.004.

[101] B. He and D. M. Soderlund, 'Human embryonic kidney (HEK293) cells express endogenous voltage-gated sodium currents and Na v 1.7 sodium channels.', *Neurosci. Lett.*, vol. 469, no. 2, pp. 268–72, 2010, doi: 10.1016/j.neulet.2009.12.012.

[102] B. Jiang, X. Sun, K. Cao, and R. Wang, 'Endogenous KV channels in human embryonic kidney (HEK-293) cells', *Mol. Cell. Biochem.*, vol. 238, no. 1/2, pp. 69–79, 2002, doi: 10.1023/A:1019907104763.

[103] C. Sommer and D. W. Gerlich, 'Machine learning in cell biology-teaching computers to recognize phenotypes', *J. Cell Sci.*, vol. 126, no. 24, pp. 5529–5539, 2013, doi: 10.1242/jcs.123604.

[104] J. Maindonald, *Pattern Recognition and Machine Learning*, vol. 17, no. Book Review 5. New York: Springer, 2007. doi: 10.18637/jss.v017.b05.

[105] K. W. Eliceiri *et al.*, 'Biological imaging software tools', vol. 9, no. 7, 2012, doi: 10.1038/nmeth.2084.

[106] G. Myers, 'Why bioimage informatics matters', *Nat. Methods*, vol. 9, no. 1, pp. 1–2, 2012.

[107] G. Danuser, 'Computer vision in cell biology', *Cell*, vol. 147, no. 5, pp. 973–978, 2011, doi: 10.1016/j.cell.2011.11.001.

[108] P. Domingos, 'A few useful things to know about machine learning', *Commun. ACM*, vol. 55, no. 10, pp. 78–87, 2012.

[109] G. E. Hinton, S. Osindero, and Y.-W. Teh, ‘Communicated by Yann Le Cun A Fast Learning Algorithm for Deep Belief Nets 500 units 500 units’, *Neural Comput.*, vol. 18, pp. 1527–1554, 2006, doi: 10.1162/neco.2006.18.7.1527.

[110] A. A. Cruz-roa, J. Edison, A. Ovalle, A. Madabhushi, and F. A. Gonz, ‘A Deep Learning Architecture for Image Representation, Visual Interpretability and Automated Basal-Cell Carcinoma Cancer Detection’, pp. 403–410, 2013.

[111] J. R. R. Uijlings, K. E. A. Van De Sande, T. Gevers, and A. W. M. Smeulders, ‘Selective search for object recognition’, *Int. J. Comput. Vis.*, vol. 104, no. 2, pp. 154–171, 2013, doi: 10.1007/s11263-013-0620-5.

[112] R. Girshick, J. Donahue, T. Darrell, J. Malik, U. C. Berkeley, and J. Malik, ‘Rich features hierarchies for accurate object detection and semantic segmentation’, in *Proceedings of the IEEE Computer Society Conference on Computer Vision and Pattern Recognition*, 2014, vol. 1, p. 5000. doi: 10.1109/CVPR.2014.81.

[113] Z. Li, C. Peng, G. Yu, X. Zhang, Y. Deng, and J. Sun, ‘DetNet: A Backbone network for Object Detection’, pp. 1–17, 2018.

[114] S. B. Busam, ‘Predicting depth, surface normals and semantic labels with a common multi-scale convolutional architecture (arXiv 2014) Seminar Recent Trends in 3D Computer Vision’, *Iccv*, no. arXiv, 2015, doi: 10.1109/ICCV.2015.304.

[115] X. Chen *et al.*, ‘Microsoft COCO Captions: Data Collection and Evaluation Server’, *ArXiv Prepr. ArXiv150400325*, pp. 1–7, 2015.

[116] P. Narang, A. Agarwal, and A. S. Sanu, ‘Detecting subtle intraocular movements: Enhanced frames per second recording (slow motion) using smartphones’, *J. Cataract Refract. Surg.*, vol. 41, no. 6, pp. 1321–1323, 2015.

[117] D. Engel, ‘Subcellular Patch clamp Recordings from the Somatodendritic Domain of Nigral Dopamine Neurons’, *J. Vis. Exp.*, no. 117, pp. 1–16, 2016, doi: 10.3791/54601.

[118] D. Purves *et al.*, *Neuroscience*. 2008.

[119] D. Franz, H. L. Olsen, O. Klink, and J. Gimsa, ‘Automated and manual patch clamp data of human induced pluripotent stem cell-derived dopaminergic neurons’, *Sci. Data*, vol. 4, pp. 1–11, 2017, doi: 10.1038/sdata.2017.56.

[120] R. C. Addis, F. C. Hsu, R. L. Wright, M. A. Dichter, D. A. Coulter, and J. D. Gearhart, ‘Efficient conversion of astrocytes to functional midbrain dopaminergic

neurons using a single polycistronic vector', *PLoS ONE*, vol. 6, no. 12, pp. 6–13, 2011, doi: 10.1371/journal.pone.0028719.

[121] S. Zhang *et al.*, "Extracellular nanomatrix-induced self-organization of neural stem cells into miniature substantia nigra-like structures with therapeutic effects on Parkinsonian rats," *Advanced Science*, vol. 6, no. 24, p. 1901822, 2019.

Publications and Patents

1. **Florence Hiu Ling Chan**, Yan Fei Liu, Musthafa Farhan, Keng Huat Koh, Bing Lam Luk* and King Wai Chiu Lai*. "Design study of gripping module for multi-size objects with tactile sensory feedback control." *2016 IEEE International Conference on Cyber Technology in Automation, Control, and Intelligent Systems (CYBER)*. IEEE, 2016.

2. **Florence Hiu Ling Chan**, Runhuai Yang, and King Wai Chiu Lai*. "Development of the electric equivalent model for the cytoplasmic microinjection of small adherent cells." *Micromachines* 8.7 (2017): 216.

3. Keng Huat Koh, Musthafa Farhan, Yan Fei Liu, **Florence Hiu Ling Chan**, and King Wai Chiu Lai*. "Learning to Grasp Unknown Objects using Force Feedback." *2017 IEEE 7th Annual International Conference on CYBER Technology in Automation, Control, and Intelligent Systems (CYBER)*. IEEE, 2017

4. **Florence Hiu Ling Chan** and King Wai Chiu Lai*. "Monitoring microinjection process of small and non-spherical living cells using electrical responses." *2018 IEEE 18th International Conference on Nanotechnology (IEEE-NANO)*. IEEE, 2018.

5. Shiqing Zhang, Peng Sun, Kaili Lin, **Florence Hiu Ling Chan**, Qi Gao, Wai Fung Lau, Vellaisamy A. L. Roy, Hongqi Zhang, King Wai Chiu Lai*, Zhifeng Huang*, and Ken Kin Lam Yung*. "Extracellular Nanomatrix-Induced Self-Organization of Neural Stem Cells into Miniature Substantia Nigra-Like Structures with Therapeutic Effects on Parkinsonian Rats." *Advanced Science* 6.24 (2019): 1901822.

6. **Florence Hiu Ling Chan**, Zhe Liu, and King Wai Chiu Lai, "Deep Learning Approach for Cell Detection and Screening in Patch clamp for Electrophysiology" IEEE Access (under review)

7. **Florence Hiu Ling Chan, CHAN, H. L.** & LO, W. C., 11 Feb 2022, (Accepted/In press/Filed) Priority No. 32022048046.3, Intelligence smart set enabling the automatic obstacle detection for the visually impaired

Awards and Achievements

1. **Florence Hiu Ling Chan**, Kong Ka Wai and Dr Jon Wing-Cheong LO, Silver Award of Inventions Geneva Evaluation Days 2022
2. **Hiu Ling CHAN (Team Leader),** Ka Wai KONG, Innovation Award (University / Tertiary Institute) , City I&T Grand Challenge, 2021
3. **Hiu Ling CHAN (PIC)**, Technology Start-up Support Scheme for Universities (TSSSU) funding – HKD1.515M , 2020 – 2023
4. **Hiu Ling Chan** (**PIC)**, Incu-App Program – HKD890k, Hong Kong Science and Technology Parks Corporation (HKSTP), 2020 – 2022
5. **Hiu Ling Chan** (**PIC)**, iDM2 Hardware Accelerator Program – HKD50k, Hong Kong Science and Technology Parks Corporation (HKSTP), 2021
6. **Florence Hiu Ling Chan** and Kong Ka Wai, Merit Awards of Hardware Journey Eco-System Contest 2021
7. **Florence Hiu Ling Chan** (**PIC)** and Kong Ka Wai, Co-Creation Funding Award – HKD800k, organized by Innovation and Technology Commission (ITC) and Hong Kong Science and Technology Parks Corporation (HKSTP), 2022